SC-4-07(RR)

CLOSE-IN PHENOMENA OF BURIED EXPLOSIONS

Final Report

May 1, 1963

Sandia Corporation Project No. 14.041.00

Sandia Corporation

Contractor for U.S. Atomic Energy Commission
ALBUQUERQUE, NEW MEXICO   LIVERMORE, CALIFORNIA

DASA-1382

SC-4907(RR)

CLOSE-IN PHENOMENA OF BURIED EXPLOSIONS

Final Report

May 1, 1963

Sandia Corporation Project No. 14.041.00

This report has been approved for open
publication by the Department of Defense,
Office of the Assistant Secretary of Defense
(Public Affairs).

Prepared for
Defense Atomic Support Agency
Washington 25, D. C.

2

TABLE OF CONTENTS

LIST OF ILLUSTRATIONS

LIST OF TABLES

INTRODUCTION

The impetus for study of close-in phenomena of buried explosions stems from a desire to understand how the explosive disturbance generates seismic waves at distances far from underground explosions. It is certain that the elastic waves produced are characterized by features of the initial explosion and by properties of the propagating medium as well. Delineation of the characteristics of the close-in disturbance provides insight into the manner of seismic wave generation by explosions, a central aim of the Vela-Uniform Program.

The close-in region about a buried explosion may be described as that in which wave propagation is nonelastic. This close-in region may be subdivided into at least two distinct subregions which are characterized by the manner of the medium's response to the explosive disturbance. In the region immediately adjacent to the explosion where disturbance of the medium is intense, wave propagation is by means of shock waves; this region is termed hydrodynamic or fluid. At distances farther removed from the explosion center, the shock wave disturbance decays to such an extent that the medium no longer responds as a fluid but not to the extent where the medium's behavior is yet elastic. This nonfluid-nonelastic region is characterized by many possible complex phenomena whose details are largely unknown. Processes such as yielding, plastic flow, crushing and cracking, phase changes, anomalous compressibility, and viscosity are likely to be encountered in this region. In spite of the vast number of existing experimental and theoretical publications on these processes, it is important to realize that little is actually known about these phenomena particularly as they may apply to underground explosions. However, numerous and valuable data from measurements in the nonfluid-nonelastic region about buried explosions await detailed theoretical description, and from these, it is hoped, we can glean information.

Significant progress has been made during the past two or three years in theoretical calculations of the wave disturbance from buried explosions in the close-in region. Most striking is the success of these calculations for the disturbance in the hydrodynamic region. It seems certain that the general features of shock wave propagation in the hydrodynamic region are correctly described by the theory. However, quantitative agreement between theoretical predictions and data recently obtained from measurements in the fluid region is not in every case obtained, indicating that refinements in theory are required.

7

Understandably, much less progress has been made in detailed calculations of the wave disturbance in the nonfluid-nonelastic region. This lack of success is principally a result of our ignorance of the medium's properties in this region. For this region a model of the medium is required which describes its properties and dynamic behavior under the conditions created by buried explosions. Criteria for dynamic yielding must be established, the influence of phase changes evaluated, the significance of viscosity and strain rate effects determined, and other possibly significant phenomena investigated before an adequate model can be obtained.

Once a realistic model is obtained, then the explosive disturbance may be theoretically described throughout both the fluid and nonfluid-nonelastic regions to the point where the disturbance is elastic. At that region in space about the explosion where the disturbance is described and where the medium responds elastically, the explosion source characteristics for seismology may be considered obtained. At present, the greatest barrier to a fuller understanding of seismic wave generation from buried explosions is the lack of knowledge of the medium's properties in the nonfluid-nonelastic region. Much of the information required for construction of an adequate model can be obtained from laboratory experiments. The remainder must come from direct measurement during full-scale explosion experiments.

The research described in this report is an attempt to obtain some information about close-in phenomena which will be helpful to the realization of objectives in the Vela-Uniform Program. Specific aims of this research have been the development of instruments capable of making measurements in the nonelastic region about buried explosions, investigation of medium properties of geologic solids relevant to studies of the close-in region, and development of a theory for description of spherical wave propagation from buried explosions.

Instruments developed are a peak shock pressure gage for measurement of 100- to 1000-kilobar shock pressures in solids and long-period, large-amplitude displacement gages for measurements in the nonfluid-nonelastic region. All instruments developed have been tested in field experiments with nuclear explosions under conditions for which they were designed. These tests have been successful and the instruments developed are currently being used to collect data from experiments with buried nuclear explosions.

Medium properties investigated have been Hugoniots and the Hugoniot elastic limits of geologic materials. Hugoniots of volcanic tuff and two types of porous soil have been measured. Also the influence of porosity and water content on the Hugoniots of porous media has been examined. Hugoniot

elastic limits have been investigated by means of a new technique employing quartz piezoelectric crystals to measure directly the stress-time profiles of finite amplitude waves in rock specimens. By this technique some qualitative information has been obtained from measurements of stress wave profiles in granite, basalt, and halite.

A phenomenological description of spherical wave propagation from buried explosions has been developed and compared with experimental data. The express purpose of this effort has been to obtain a simple analytical description without resort to the formidable difficulties of a more rigorous mathematical approach and without detailed consideration of the numerous possible complex phenomena which occur in the close-in region. Objectives were to obtain, in terms of a few parameters which characterize gross properties of media, expressions for the decay of wave pressure with distance which could then be compared with numerous available data. Calculations have been compared with data from both nuclear and chemical explosions in granite, halite, volcanic tuff and desert alluvium over the complete range of pressures found in all regions from the hydrodynamic to the elastic. The results of calculation are presently as accurate as those of other methods.

Section 1

HYDRODYNAMIC SHOCK PRESSURE GAGE

A. J. Chabai, R. C. Bass, and H. L. Hawk

Background

The purpose of developing an instrument that can measure pressures of amplitude from 0.1 to 1 megabar (100 thousand to 1 million atmospheres) is to obtain data on the shock wave decay with distance in the hydrodynamic region about buried explosions and to provide information for the evaluation of theoretical calculations. Conventional pressure gages can not operate at the extreme pressure levels associated with shock waves in solids, nor are their principles of operation generally applicable for extension to the high pressures in question. Indeed, the material of which the gage is constructed may be a significant perturbation on the shock wave whose pressure is to be measured. At shock pressures of 0.1 to 1 megabar all materials suffer a large compression and so any transducer will have its physical form drastically altered; in short, it will be destroyed by shock waves. The extreme pressures and high accelerations associated with shock waves present a difficult environment for any transducer. Clearly any transducer in this environment must complete its measurement before it and its component circuitry and cabling are destroyed.

Of the five hydrodynamic quantities - pressure, density, temperature, particle velocity and shock wave velocity - which characterize any shock wave, the one most susceptible to direct measurement is shock wave velocity. Particle velocity comes next in ease of measurement.* Pressure and temperature behind shock waves in solids have never been directly measured. While direct measurements of density behind shock waves in solids have been made by flash-X-ray techniques in laboratory experiments the method is not considered feasible for use in a field gage.

The boundary conditions at a shock front specifying conservation of mass and momentum contain the four unknown hydrodynamic quantities - pressure, density, particle velocity, and shock velocity. If any two of these can be measured, then the remaining two quantities are determined by the conservation equations. In laboratory experiments[1] on shock waves in solids, shock velocity and particle velocity are measured; shock pressure and density are then inferred from the conservation equations.

---

*From measurements of free surface velocity particle velocity is inferred (see Reference 1).

This laboratory technique has been adopted by Lombard[2] in development of a peak shock pressure gage for field use. Another laboratory technique[1] used to determine hydrodynamic quantities behind shock waves is the impedance-mismatch method. In this method use is made of some material whose Hugoniot is known, and measurement of only one quantity, shock velocity, is required in order to infer pressure, density, and particle velocity. Since shock velocity is more easily measured than particle velocity the principles of the impedance-mismatch technique have been chosen for the development of the peak shock pressure transducer described in this report.

Other methods for measurement of peak shock pressures, employing new and different principles, are currently being investigated. For example, Lombard[3] has made use of electric current released by Lucite under the influence of shock pressure. It is found that over a certain range of shock pressures the peak current released by Lucite is directly proportional to peak shock pressure.

Research is also being conducted to develop shock pressure gages capable of measuring pressure as a function of time behind the incident shock fronts. Significant progress along these lines has been made. Keough and Bernstein[4] have employed a technique where the changes in resistance of a wire over which a shock wave is passing are related to the pressure changes behind the wave. Manganin wire appears to be the most promising sensor. The percentage increase in wire resistance is a linear function of shock front pressure over the range investigated (10 to 150 kilobars). Measurement of pressure-time history behind a shock wave can be made for times of the order of tens of microseconds before the gage is destroyed.

Another gage being developed [5,6] for measurement of shock wave pressure-time profiles consists of a disk-shaped cell filled with distilled water into which two silver electrodes are inserted. Applying a potential to the electrodes and passing a shock wave through the cell results in an output signal which varies directly with incident shock pressure and directly with the initially applied potential. No signal is observed with zero applied potential. Pressure-time waveforms are observed for periods of 10 to 20 μsec and have shapes similar to those obtained with the manganin resistance wire gage.

While not all of the pressure gages currently under development have been extensively tested in field experiments, their eventual use will provide much information about wave propagation in the non-elastic region about buried explosions.

As a result of research activity in shock pressure transducers, roughly 25 measurements of peak shock pressure have been successfully performed during the past two years in the hydrodynamic region

about buried explosions. The measurements were made using the impedance-mismatch gages and the Lombard[2] gage. Shock pressures recorded[7,8,9] have been from 20 to more than 600 kilobars in granite, volcanic tuff, and desert alluvium. These pressure measurements have yielded valuable information and, together with independent measurements of shock wave position as a function of time, provide the basis for confidence in the theoretical description of shock wave propagation in the hydrodynamic region about buried explosions.

Impedance-Mismatch Shock Pressure Gage

Conservation of momentum and mass at the front of a shock wave are specified by the equations[1]

$$P = \rho_o V u \tag{1.1}$$

and

$$\rho_o V = \rho(V-u), \tag{1.2}$$

where P, ρ, and u are respectively pressure, density and particle velocity behind the shock wave, V is shock velocity, and ρ_o is the density of the medium into which the wave progresses. In Equations 1.1 and 1.2 it is assumed that the medium is at rest, $u_o = 0$, and that ambient medium pressure, P_o, is essentially zero. The increase in internal energy, $E-E_o$, is given by

$$E-E_o = \tfrac{1}{2}P\left(\frac{1}{\rho_o} - \frac{1}{\rho}\right) \quad . \tag{1.3}$$

The Hugoniot of a material is a relationship between P and ρ and represents the locus of the thermodynamic states which can be attained in the material by means of shock waves. Every material has a unique Hugoniot. From laboratory experiments[10] it has been found that for most solids shock velocity is a linear function of particle velocity over a wide range of shock pressures,

$$V = C + Su \quad . \tag{1.4}$$

Eliminating velocities in Equations 1.1, 1.2 and 1.4, the Hugoniot is obtained in terms of the material constants ρ_o, C and S:

$$P = \frac{\rho_o C^2 \rho(\rho-\rho_o)}{\left[\rho_o S - \rho(S-1)\right]^2} \quad . \tag{1.5}$$

13

By eliminating shock velocity from Equations 1.1 and 1.4 another form for the Hugoniot can be expressed in terms of pressure, particle velocity, and the material constants:

$$P = \rho_o (C + Su)u \quad . \tag{1.6}$$

The principle of operation of the impedance-mismatch gage is an extension of well known[1] laboratory techniques and is illustrated by the following example. Consider a plane shock wave progressing through a medium whose Hugoniot is unknown, and assume that this incident wave encounters two or more different materials of known Hugoniot in its path (see Figure 1.1).
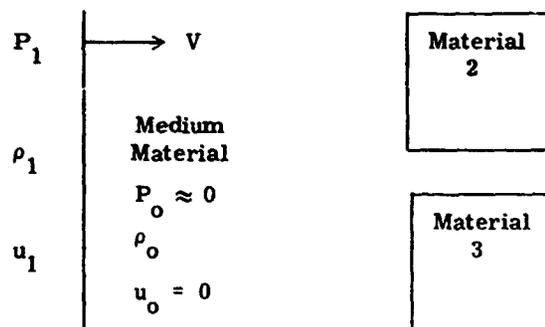
Figure 1.1 Shock Wave Incident on Dissimilar Materials

At the interfaces of the materials with known Hugoniots, shock waves are transmitted into these materials and waves are reflected back into the medium. By measuring the shock wave transit times through materials 2 and 3, shock pressure in each material is determined since their Hugoniots are known. This information together with a measurement of the incident shock velocity allows the incident shock pressure to be inferred.

The known Hugoniots (Equation 1.6) of materials 2 and 3 of Figure 1.1 are illustrated in Figure 1.2 together with the medium Hugoniot, 1, considered unknown. From the shock-wave transit-time measurements in materials 1, 2, and 3 we obtain shock velocities, and with the known values of material densities, shock impedance, $\rho_o V$, is determined for each material.

By Equation 1.1 it is seen that shock impedance is represented by a line of slope $\rho_o V$ passing through the origin of coordinates in Figure 1.2. Since the momentum equation must be satisfied and since the pressure of the shock wave must be given by one of the points on the Hugoniot curve, the intersection of the line of slope $\rho_o V$ with the medium Hugoniot curve determines the pressure and particle velocity of the shock wave whose impedance is $\rho_o V$. This point of intersection is given by the solution

of Equations 1.1 and 1.6 once $\rho_o V$ has been measured. It is because the Hugoniots of materials 2 and 3 are known that pressures P_2 and P_3 and corresponding particle velocities u_2 and u_3 may be obtained from shock transit time measurements in these materials.
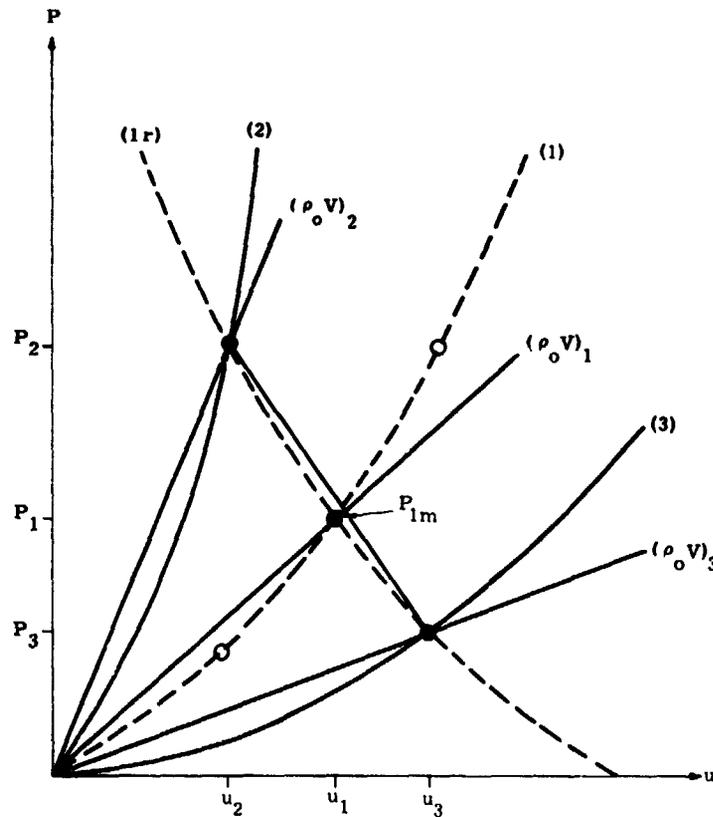
Figure 1.2 Illustration of Peak Shock Pressure Determination From
Pressure-Particle Velocity Diagram

Now the transmitted pressures and particle velocities established in materials 2 and 3 are determined by the strength of the incident shock wave in the medium material, 1. Since the shock impedances of materials 2 and 3 differ from the medium impedance, the transmitted shock pressures will be different from those of the incident shock and waves will be reflected back into the medium material at the interfaces. Applying the conservation equations to the system of waves resulting after the incident shock passes an interface, it is found that pressure and particle velocities of a reflected wave must lie on a curve called the "reflection Hugoniot."[1,11,12] This curve, illustrated by 1r for the medium material in Figure 1.2, represents the reflected wave traveling in a direction opposite from the incident wave and determines the locus of states, (P, u), which may be attained by reflected waves starting from the shocked state, (P_1, u_1). From the boundary conditions that pressure and particle

velocity must be continuous across an interface, it is seen that the intersection of curves 1r and 2 of figure 1.2 determines the values of pressure and particle velocity for both the transmitted and reflected waves at the interface between materials 1 and 2. In this case it is seen that the reflected wave is a shock wave $(P_2 > P_1)$ since the shock impedance of material 2 is greater than that of the medium material. Similarly, considering materials 1 and 3, it is seen from Figure 1.2 that from this interface a rarefaction wave $(P_3 < P_1)$ is reflected since $(\rho_0 V)_3 < (\rho_0 V)_1$.

It is found[1] experimentally that within a few percent the reflection Hugoniot, 1r, is the mirror image of the Hugoniot curve, 1, about the line $u = u_1$. Consequently the reflection Hugoniot may be expressed as

$$P = \rho_0 \left[S(2u_1 - u)^2 + C(2u_1 - u) \right] \quad . \tag{1.7}$$

The points (P_2, u_2) and (P_3, u_3), established by shock transit time measurements in materials 2 and 3, are also points on the unknown Hugoniot of the medium (noted by open circles in Figure 1.2). The impedance-mismatch gage can make use of this fact in obtaining information on the Hugoniot of the medium material.

If materials 2 and 3 are chosen to have a higher and lower shock impedance than the medium as shown in Figure 1.2, then the incident shock pressure may be estimated by interpolation as that pressure, P_{1m}, determined by the intersection of the line of slope $(\rho_0 V)_1$ and a line joining the points (P_2, u_2) and (P_3, u_3) on the Hugoniot of materials 2 and 3. If the two materials of known Hugoniot both have higher or lower shock impedances than the medium, then an extrapolation procedure may be employed to establish P_{1m} . The interpolated pressure, P_{1m}, will, as seen in Figure 1.2, always be greater than the incident shock pressure, P_1; however, it is found empirically from examination of the interpolation procedure for various combinations of materials 1, 2, and 3 and for various incident pressures, P_1, that the difference between P_{1m} and P_1 resulting from interpolation will, in almost every case, be much less than the maximum combined percentage error (25 percent) expected from other sources in the measurement process. A 10 percent error appears to be a more realistic error incurred in P_1 by a straight line interpolation procedure.

Once P_{1m} and also u_{1m} are obtained Equation 1.7 and the points (P_2, u_2) and (P_3, u_3) may be utilized to estimate the unknown Hugoniot of the medium. Since medium density ρ_{01} is known and u_{1m} has been obtained, the two unknown constants, S_1 and C_1, which determine the medium Hugoniot

(Equation 1.5), may be evaluated. This procedure gives at least an estimate of the Hugoniot in the vicinity of the pressure, P_1. From similar measurements of shock pressure at different levels of the incident pressure, P_1 (at different distances from an explosion), additional Hugoniot points and values of C_1 and S_1 near the pressure P_1 are obtained, which, when all taken together, provide an estimate of the in situ medium Hugoniot curve (curve 1 of Figure 1.2) over the range of measured pressures.

It must be emphasized that the impedance-mismatch method of measuring shock pressures is strictly applicable only to strong shock waves. At lower wave pressures where, for example, phase changes may be induced in the medium material, the Hugoniot (curve 1 in Figure 1.2) will have a cusp or point of inflection, and the reflection Hugoniot (curve 1r) will likely not be the mirror image of the Hugoniot, particularly that portion of the reflection Hugoniot which joins the initial shock point (P_1, u_1) with a lower impedance point such as (P_3, u_3) in Figure 1.2. Fortunately, it appears from presently available data that even marked phase changes induced by shock waves in geologic materials do not produce marked cusps or deviations from a smooth (P-u) Hugoniot curve (Equation 1.6) whose C and S values are evaluated by strong shock measurements. In addition, that portion of the reflection Hugoniot joining points such as (P_1, u_1) and (P_3, u_3) in Figure 1.2 is actually an adiabat which is absolutely unknown for geologic materials and which, more than likely, has no inflection points as does a Hugoniot with phase changes. The observation that a Hugoniot curve in the P-u plane is not grossly altered from a continuous curve as given by Equation 1.6 by phenomena such as phase changes, and the qualitative belief that the adiabatic portion of the reflection Hugoniot will be a continuous curve and nearly equal to the mirror image of the Hugoniot, tend to be compensations for errors incurred in P_{1m} when an impedance-mismatch gage is used at pressure levels where phase changes may occur. Until more precise methods are available for measuring shock pressures, it is felt that the impedance-mismatch technique will provide reasonable values of incident shock pressure even at pressures where phenomena such as phase changes cause cusps or departures from a smooth Hugoniot curve.

To test the impedance-mismatch method of determining incident shock pressures, laboratory experiments were conducted in which 2024 aluminum (whose Hugoniot is known[1]) was used to represent the medium. Brass and Plexiglas were used as the mismatch materials 2 and 3 of known [10, 13] Hugoniot. Plane shock waves were generated in the aluminum using TNT and Composition-B explosives. The 210-kilobar shock from TNT and the 350-kilobar shock from Composition-B expected in aluminum were measured by the impedance-mismatch method with errors of about 5 percent.

As envisaged for field use in drill holes radial to an explosion center the impedance-mismatch gage will have a large circular disk (Figure 1.3) cut from rock cores taken at or near positions in the medium where pressure measurements are desired.
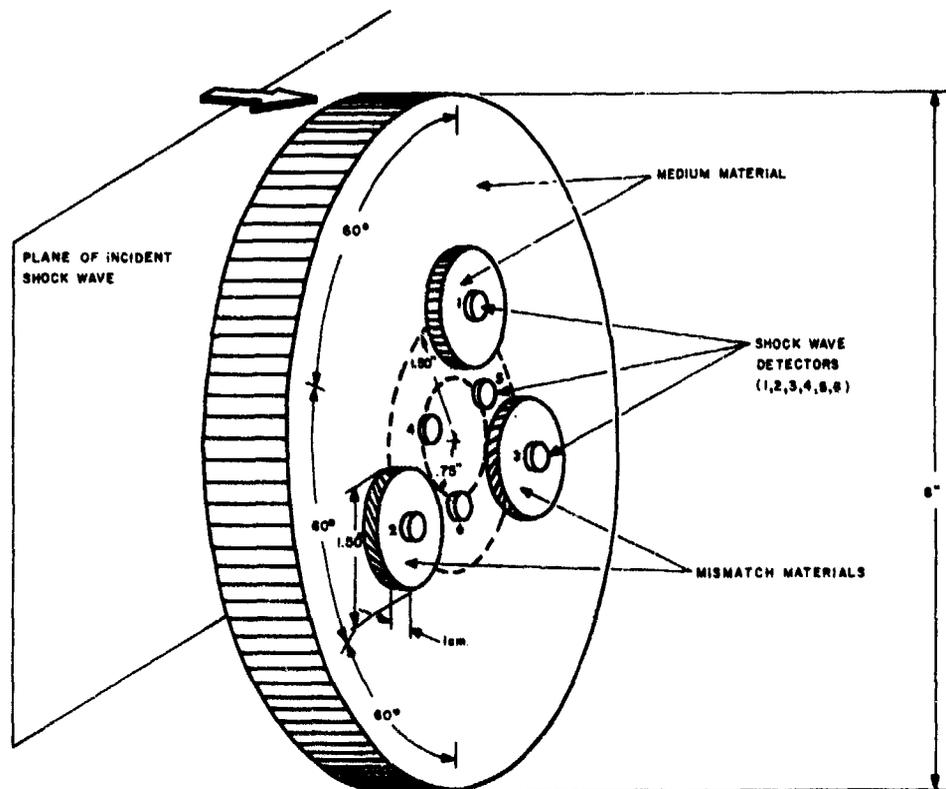
Figure 1.3 Schematic of Impedance-Mismatch Gage Assembly

A typical arrangement of the basic elements for an impedance-mismatch gage is shown in Figure 1.3. On the flat surface of the large circular disk of medium material (8 inches in diameter and 1 to 2 inches in thickness) are mounted three smaller disks (dimensions 1-1/2 inch diameter and 1 cm thick). The two disks of mismatch material and the small disk of medium material have their centers on a circle of 1-1/2 inch radius and are spaced 120 degrees apart. Diameter-to-thickness ratio of the small disks must be about 2 or more in order to avoid the influence of edge effects[10] on detectors as the shock wave progresses through the disks. Shock wave detectors are placed at the center of the back face of each of the small disks (numbered 1, 2 and 3 in Figure 1.3). In addition, three shock detectors (numbered 4, 5 and 6) are placed on the back surface of the large disk. These latter three, mounted on

18

a circle of 3/4-inch radius, are spaced 120 degrees apart and located symmetrically to the small disks as shown in the figure.

Detectors 2 and 3 each in combination with any one or all of the detectors 4, 5 and 6 serve to determine shock transit times in the mismatch materials. Detector 1 with 4, 5 or 6 establishes transit time in the medium material. Thus, for example, in the case of a normally incident plane shock wave, the impedance slopes, $(\rho_o V)_1$, $(\rho_o V)_2$, and $(\rho_o V)_3$, required in Figure 1.2 for determination of medium shock pressure, may be obtained from transit time measurement of detector combinations 1 and 4, 2 and 5, and 3 and 6, respectively.

When the incident wave is not normal, correction for tilt (angle between the longitudinal axis of the large medium disk and a normal to the plane of the incident shock wave) must be made. It is for the purpose of measuring shock tilt that three detectors, 4, 5, and 6, are used on the large medium disk. Detectors 4, 5, 6, and 1 form a set of four noncoplanar points which in principle are sufficient to determine both degree of shock tilt and shock velocity in the medium material.

Consider, for example, a plane wave incident on the shock gage and tilted with respect to the longitudinal axis of the gage of Figure 1.3. Suppose that detector number 4 first senses the shock wave. Construct a cartesian system of coordinates with the center of detector 4 as origin and with one of the coordinate axes parallel to the longitudinal gage axis. Then from the four equations

$$V\Delta t_{14} = \Delta x_{14}\cos\alpha_1 + \Delta y_{14}\cos\alpha_2 + \Delta z_{14}\cos\alpha_3$$

$$V\Delta t_{54} = \Delta x_{54}\cos\alpha_1 + \Delta y_{54}\cos\alpha_2 + \Delta z_{54}\cos\alpha_3$$

$$V\Delta t_{64} = \Delta x_{64}\cos\alpha_1 + \Delta y_{64}\cos\alpha_2 + \Delta z_{64}\cos\alpha_3 \qquad (1.8)$$

$$1 = \cos^2\alpha_1 + \cos^2\alpha_2 + \cos^2\alpha_3 \quad ,$$

incident shock velocity, V, and its direction cosines $\cos\alpha_1$, $\cos\alpha_2$, and $\cos\alpha_3$ may be determined in terms of the known positions of detectors 1, 5 and 6 with respect to detector 4 and in terms of the measured time differences Δt_{14}, Δt_{54}, and Δt_{64}. A solution of the equations is possible only if the four detectors are not coplanar. It is assumed that a field gage can be located with some degree of accuracy so that shock wave tilt will not be too great and so that possible shock wave refraction effects will be negligible.

For experiments in which drill holes radial to an explosion center are not feasible but in which vertical drill holes to the depth of an explosion center are available, the impedance-mismatch gage can be a rectangular slab with elements mounted on the back face in a manner similar to that shown in Figure 1.3. Whenever a gage is placed in a vertical drill hole, orientation of the gage will be required. Field experience with orientation has shown that, by means of gyroscopes attached to gages, an axis normal to the gage or slab face may be aligned in a 1000-foot-deep hole to within 1 degree with a horizontal line passing through the explosion center.

In final form for field installation the gage will be mounted in a canister which protects the working elements of the assembly and to which the signal cables and gage lowering equipment may be attached. The front surface of the medium disk must, of course, be completely exposed so as not to impose a perturbation on the pressure measurement. Bonding the medium disk to the in situ material is discussed below.

Shock Wave Detectors

Several types of shock detector elements have been considered for use with the impedance-mismatch gage. The properties of both piezoelectric ceramic detectors and shorting pin detectors have been examined. In addition, a shorting "circular switch" type of detector has been investigated.[14] Up to shock pressures of about 1 megabar, piezoelectric ceramics of lead-zirconate-titanate are found to be by far the best; however, any detector element of fast rise time ($\sim 10^{-8}$ sec) and output of 10 or more volts would serve as well.

In Figure 1.4 are shown the components of a PZT detector which has proven to be extremely reliable. A small wafer* of PZT, 0.120 inch in diameter by 0.020 inch in thickness is sandwiched into a small brass housing onto which a standard Microdot coaxial cable connector is attached. For use with an impedance gage the assembly is simply cemented into position, usually with an epoxy mixture.

It has been found that the PZT detector of Figure 1.4 releases considerable amounts of charge over a relatively wide range of pressures. For example, at a shock pressure of 300 kilobars about 100 volts are generated by the PZT wafer across a 50-ohm resistive load. As shock pressure is increased, however, the output signal progressively decreases. Precise experiments by Reynolds and Seay[15] have shown a marked decrease in charge per unit area released by PZT as shock pressure increases from 20 to 150 kilobars. Our investigations of the PZT detector shown in Figure 1.4 indicate that

---

*Obtained from Clevite Corp., Electronic Components Div., 3405 Perkins Ave., Cleveland 1, Ohio.

output voltages from PZT are still sufficiently high and usable in a pressure gage up to 1-megabar pressures. At 1-megabar pressure, the output is about 10 volts across a 50-ohm load. At shock pressures in excess of 1 megabar PZT ceramics are not adequate as detectors for field gages. For shock wave detection at pressures in excess of 1 megabar, we have used the 0.032-inch coaxial self-shorting pins manufactured by Edgerton, Germeshausen and Grier, Inc.; however, the shorting pins do not have the same reliability that PZT ceramics have at lower pressures. Investigations of different types of piezoelectric ceramics other than PZT are being made in the hope of finding one which will operate at pressures above 1 megabar.

CUTAWAY VIEW OF STANDARD MICRODOT COAXIAL CABLE CONNECTOR   BRASS INNER ELECTRODE   PZT CERAMIC (CLEVITE PZT-4)   BRASS OUTER ELECTRODE

SCALE - 10/1 APPROX.
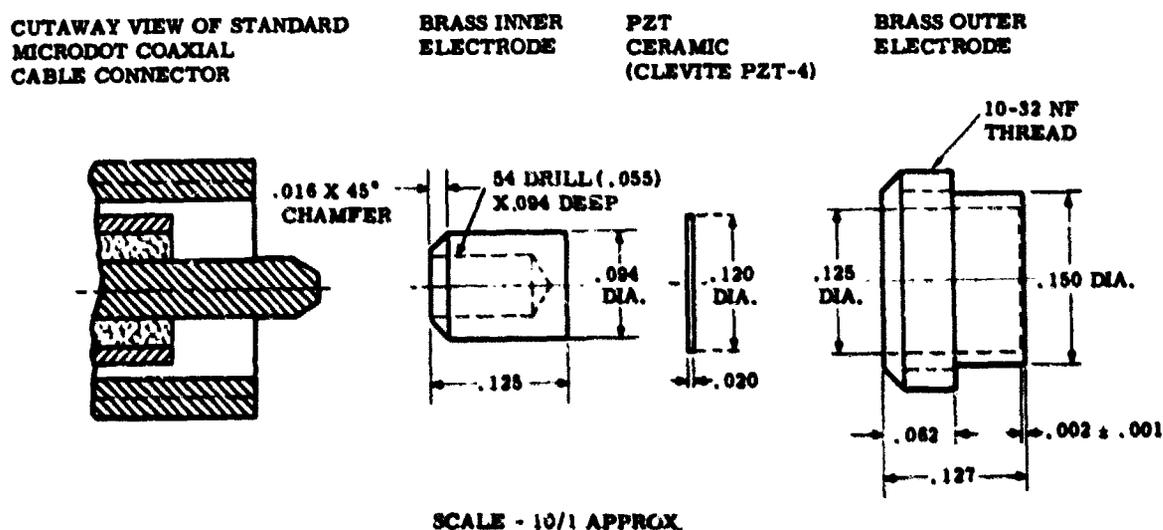
Figure 1.4   Assembly Drawing of PZT Shock Wave Detector

Delay Time Coding Mixer Circuit

When a shock wave is nearly normally incident on the gage of Figure 1.3, output signals from detectors 4, 5, and 6 will be nearly coincident. Also, depending on the incident shock pressure and the material of the medium and mismatch disks, signals from detectors 1, 2, and 3 may occur nearly simultaneously. In addition, since the degree of tilt of the shock wave at the pressure gage cannot be known before a measurement is made, one does not know, for example, which of detectors 4, 5, or 6 will give an output signal first. To identify each detector signal and to distinguish unambiguously those signals which occur nearly simultaneously, a delay time coding mixer circuit has been developed.

An electronic circuit [16] (Figure 1.5), developed for use with an impedance-mismatch pressure gage, is employed to identify detector output signals and to allow the times at which a shock wave activates the detectors to be measured with some precision.
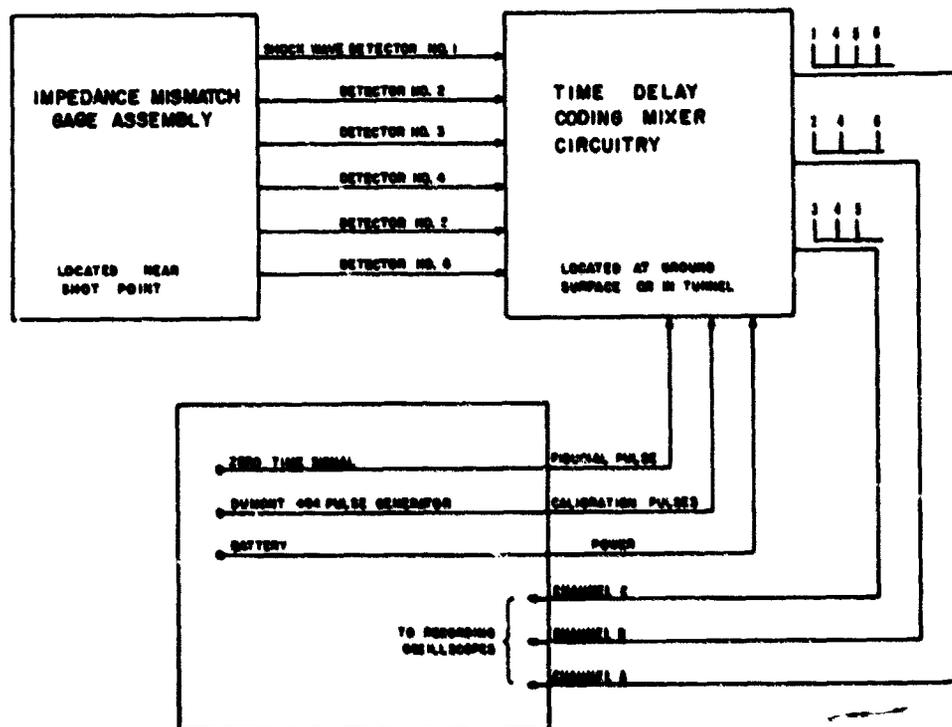
Figure 1.5. Circuit Flow Diagram for Time-Delay Coding Mixer Circuitry

The time delay coding mixer (TDCM) circuit performs the function of delaying in time several of the output signals from detectors and mixing these signals in appropriate combinations for recording. Delaying signals by prescribed amounts serves the purpose of identifying signals with particular detectors and of increasing the separation in time of those signals which occur nearly simultaneously (two output signals are considered simultaneous when they are separated in time by an amount which is less than the pulse width of either signal). Provisions are made in the TDCM for receiving pulses from a pulse generator for preshot calibration of time delays and for receiving a zero time signal.

From Figure 1.5 it is seen that output signals from detectors 4, 5, 6, and 1 - which measure shock velocity and tilt of the shock wave in the medium - are delayed and mixed in the TDCM circuit and fed out on a single line, channel A, to the recording station. Signals from detectors 2, 4, and 6 - which measure shock velocity in one mismatch material - are delayed, mixed, and fed out on channel B. Similarly, signals from detectors 3, 4, and 5 on channel C determine shock velocity in the other mismatch

22

material. There is some redundancy of signals on channels B and C used to obtain velocity in the mismatch material. This redundancy has been specifically designed into the circuit as a safeguard against the possible failure of one or two of the PZT detectors, 4, 5, and 6.

Figure 1.6 is a block diagram of the TDCM. Its principal circuit for reception of signals from the detectors involves for each detector an "and" gate, a 26 μsec blanking monostable multivibrator (MMV), a delay MMV and inverter (for detectors 4, 5, and 6 only), a pulse-shaping MMV, an "or" gate, and an emitter follower. The subsidiary and optional enabling circuit consists of a 120 μsec delay MMV, an inverter, and an enabling MMV for operation of the "and" gates.
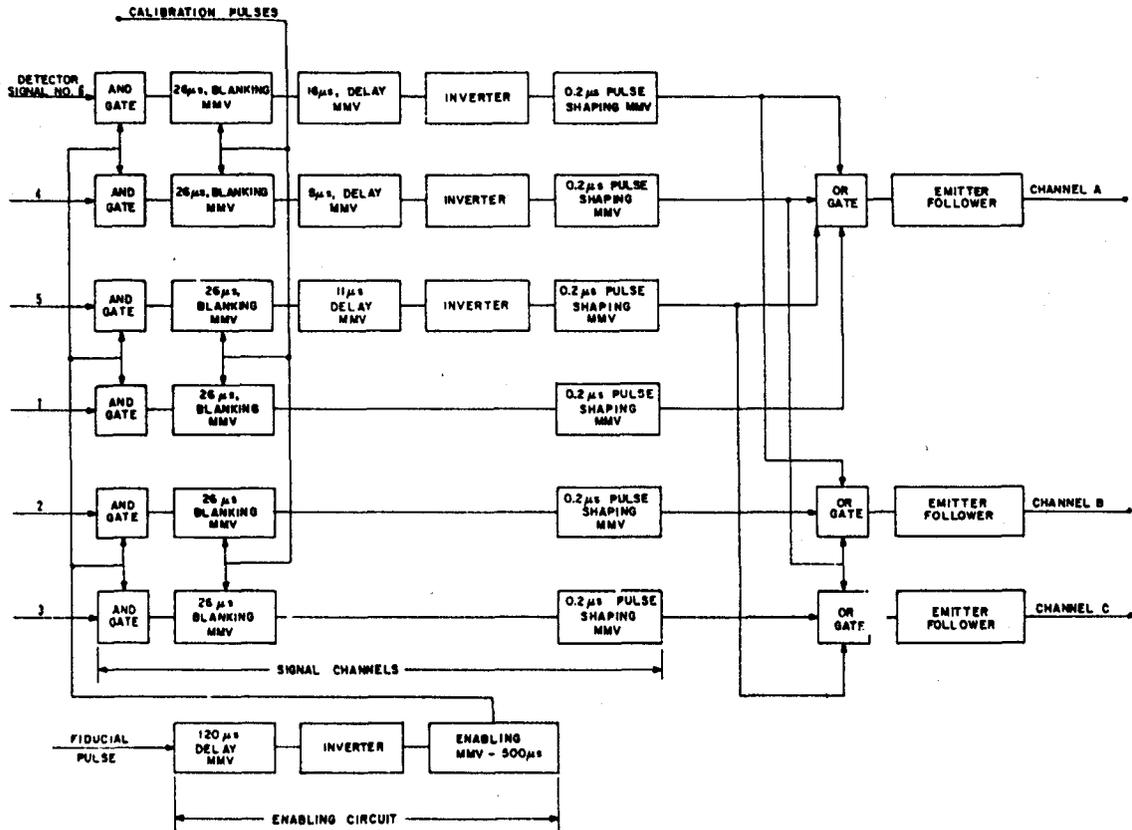
Figure 1.6   Block Diagram of Time-Delay Coding Mixer Circuit

The optional enabling circuit has been designed for use with pressure gages that will be placed very close to explosions. Its purpose is to blank out any early extraneous signals from an explosion and prevent them from triggering the TDCM and recording scopes. When used, the enabling circuit, as shown, provides a 500-μsec long signal which activates the "and" gates and makes them receptive to detector signals from 120 μsec to 620 μsec after zero time. The time at which the "and" gates are activated and the duration of activation can be varied to suit the requirement of a particular pressure

gage. At shock pressure gage positions where it is felt that extraneous signals will not be troublesome, the enabling circuit is not used, the "and" gates are bypassed, and detector signals are presented directly to the 26 μsec delay MMV's.

In the main TDCM circuit, the 26 μsec blanking MMV's are used to eliminate noise and undesired signals, such as cable breaks which may occur after the measurement signals are obtained from detectors.

The delay MMV's take the nearly simultaneous signals from detectors 4, 5, and 6 and delay each signal by a different amount so that it may be identified with the detector which generated it. The particular values of delay times shown in Figure 1.4 were more or less arbitrarily chosen and can be varied according to estimated shock wave transit times in the gage and to meet conditions required for recording.

From inverters or directly from blanking MMV's, signals are passed to the pulse-shaping MMV's after first being differentiated. Output from a pulse-shaping MMV is a single positive pulse of 0.2 μsec duration and of about 8-volt amplitude (see Figure 1.7).
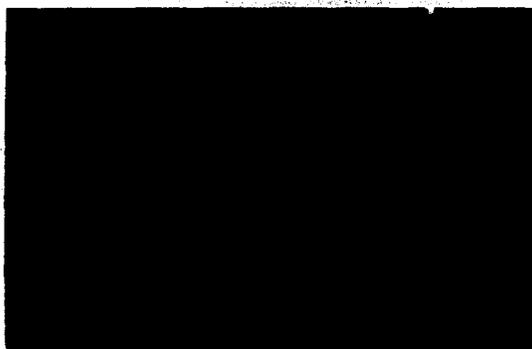
Figure 1.7 Output of Pulse Shaping MMV, 2 Volts/cm, 0.1 μsec/cm

Figure 1.8 shows the typical operation performed by the TDCM on the signal from detector number 6.

Output signals from detectors 1, 4, 5, and 6 - after being delayed, inverted, differentiated, and shaped - are mixed by the "or" gate and then passed to an emitter follower whose output is channel A. In Figure 1.9 are shown output displays which are expected from channel A during calibration and for a normal incidence shock wave with a velocity of 2.5 mm/μsec in a medium disk with a thickness of 1 cm.
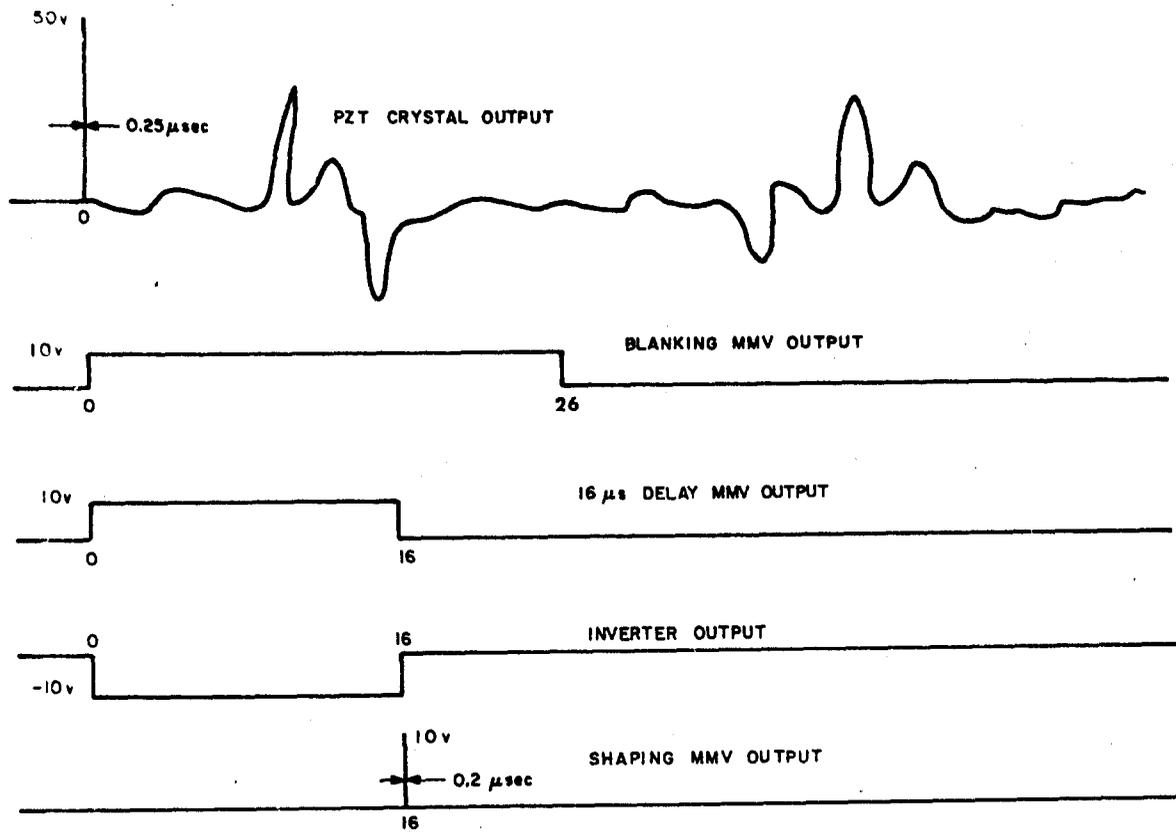
Figure 1.8 Typical Operation of TDCM, Signal Output From Detector No. 6
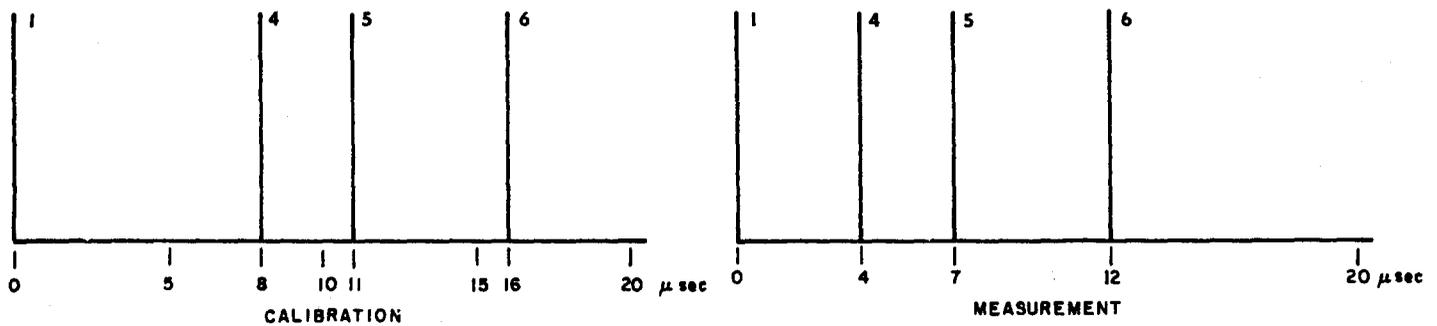
Figure 1.9 Channel A Displays During Calibration and for a Shock Wave of Normal Incidence

A prototype TDCM circuit has been built and its characteristics and electronic operation evaluated.[16] Figures 1.10(a) through 1.10(e) present detailed circuit diagrams of the TDCM. Figures 1.11(a) and 1.11(b) show two views of the prototype circuit. Channel A, B, and C outputs resulting from calibration signals applied simultaneously to simulate detector signals 1 through 6 are shown in Figure 1.12. Stability tests indicate that delay times produced by the TDCM are constant to better than 0.02 μsec over periods of more than 30 minutes.
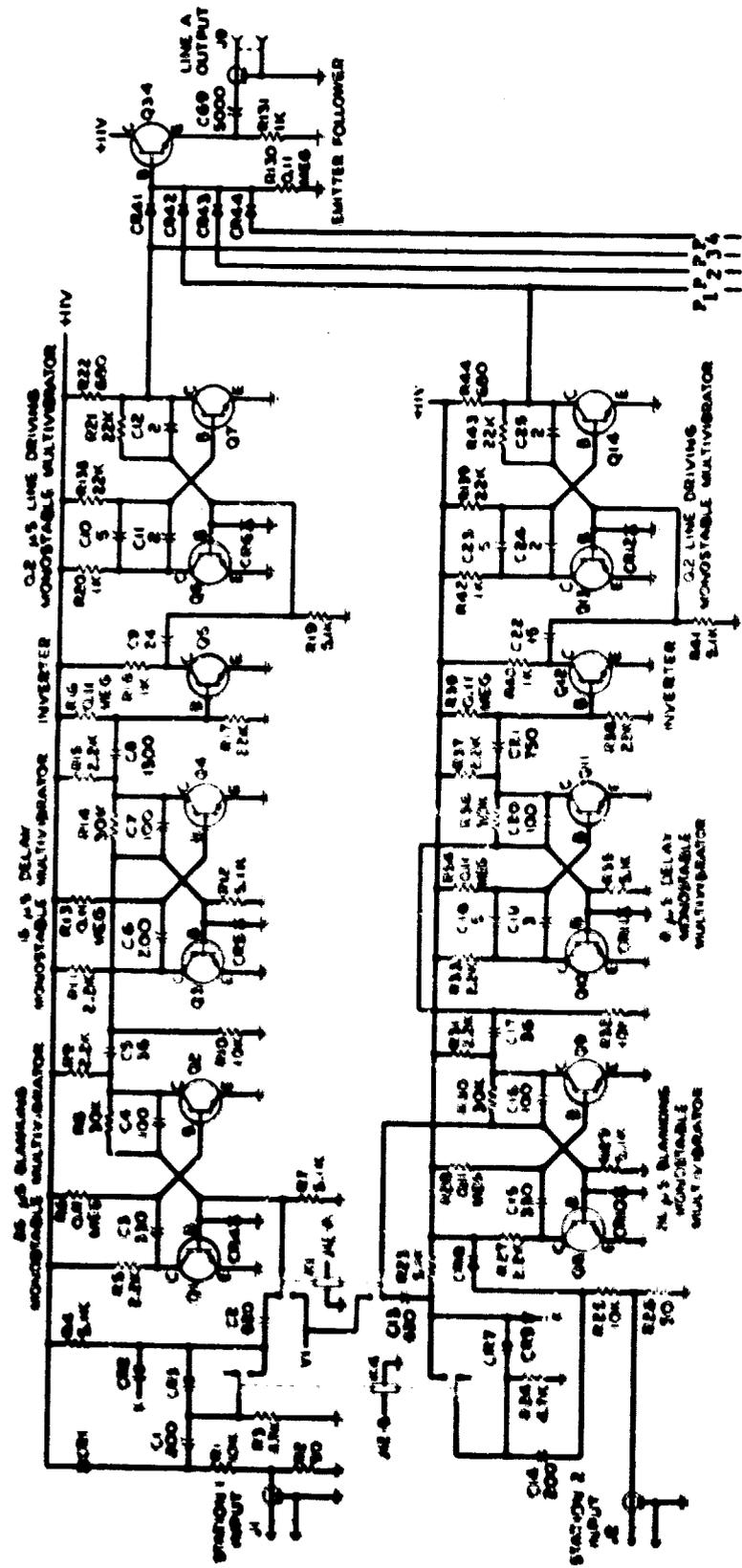
Figure 1.10(a) Channel A Circuit Diagram
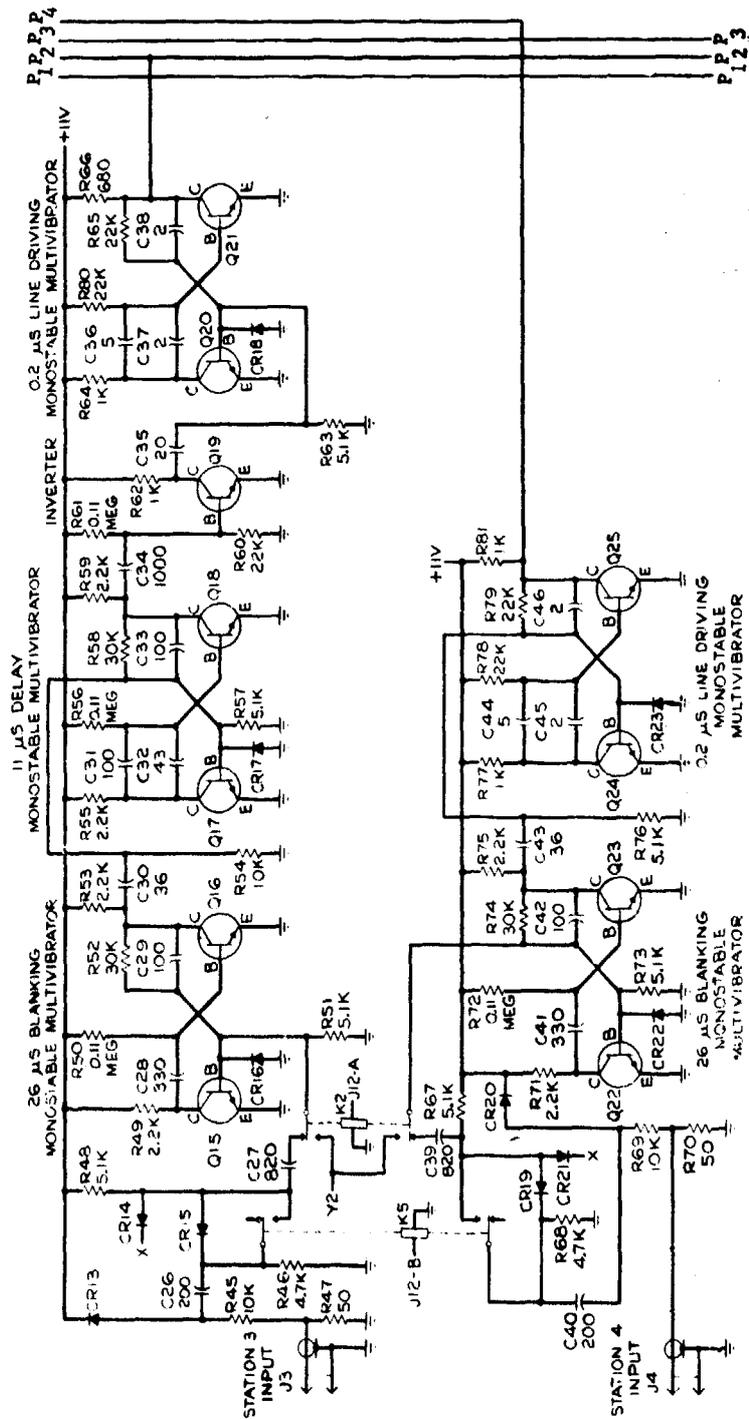
Figure 1.10(b) Channel A Circuit Diagram (Continued)
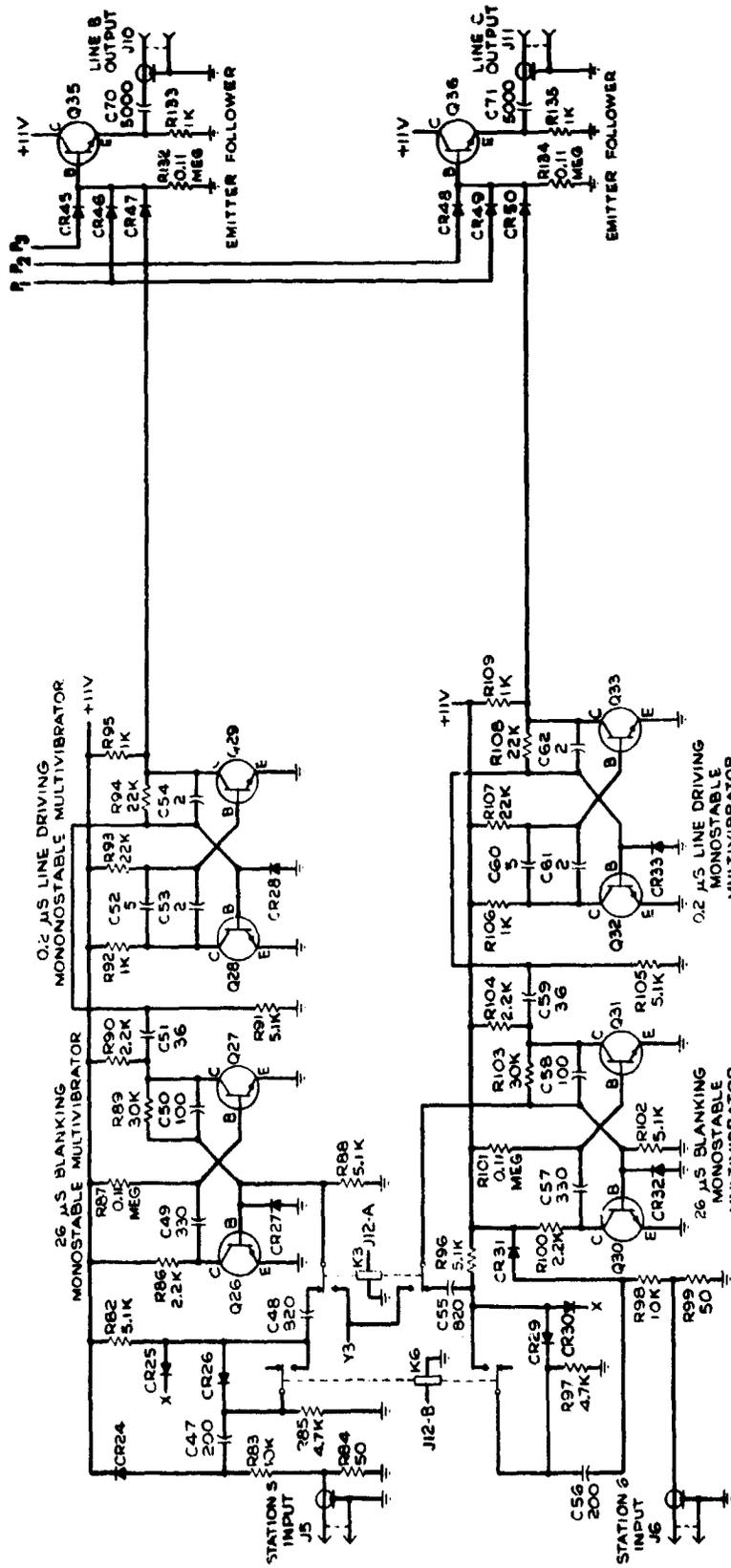
NOTES

1 RESISTANCE VALUES ARE IN OHMS UNLESS OTHERWISE SPECIFIED.

2 CAPACITANCE VALUES ARE IN MICROMICROFARADS UNLESS OTHERWISE SPECIFIED.

3 THE FOLLOWING TRANSISTORS ARE 2N1613 TYPE: Q1 THRU Q5, Q8 THRU Q12, Q15 THRU Q19, Q22, Q23, Q26, Q27, Q30, Q31, Q37 THRU Q41. ALL OTHERS ARE 2N744 TYPE.

Figure 1.10(c)   Circuit Diagram for Channels B and C
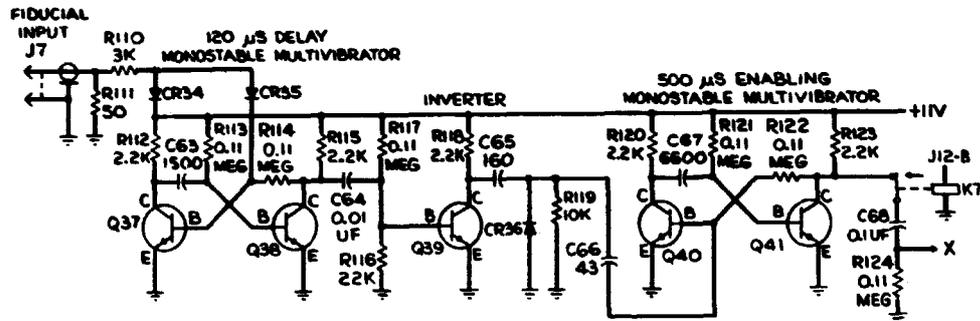
NOTES

1   RESISTANCE VALUES ARE IN OHMS UNLESS OTHERWISE SPECIFIED.

2   CAPACITANCE VALUES ARE IN MICROMICROFARADS UNLESS OTHERWISE SPECIFIED.

3   THE FOLLOWING TRANSISTORS ARE 2N1613 TYPE: Q1 THRU Q5, Q8 THRU Q12, Q15 THRU Q19, Q22, Q23, Q26, Q27, Q30, Q31, Q37 THRU Q41. ALL OTHERS ARE 2N744 TYPE.

Figure 1.10(d)　Enabling Circuit Diagram
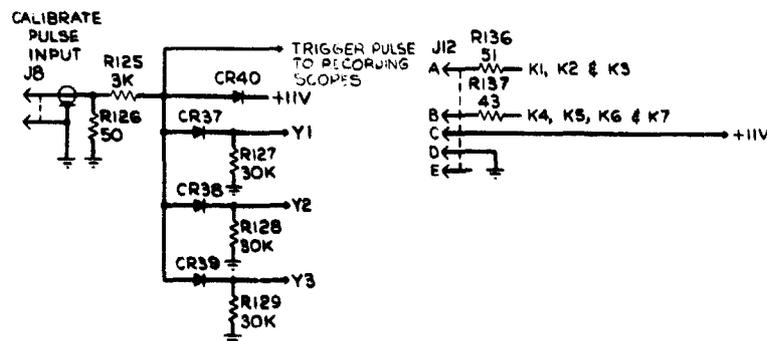
NOTES

1　RESISTANCE VALUES ARE IN OHMS UNLESS OTHERWISE SPECIFIED.

2　CAPACITANCE VALUES ARE IN MICROMICROFARADS UNLESS OTHERWISE SPECIFIED.

3　THE FOLLOWING TRANSISTORS ARE 2N1613 TYPE: Q1 THRU Q5, Q8 THRU Q12, Q15 THRU Q19, Q22, Q23 Q26, Q27, Q30, Q31, Q37 THRU Q4L ALL OTHERS ARE 2N744 TYPE.

Figure 1.10(e)　Calibration Circuit Diagram

NOTES

1　RESISTANCE VALUES ARE IN OHMS UNLESS OTHERWISE SPECIFIED.

2　CAPACITANCE VALUES ARE IN MICROMICROFARADS UNLESS OTHERWISE SPECIFIED.

3　THE FOLLOWING TRANSISTORS ARE 2N1813 TYPE: Q1 THRU Q5, Q8 THRU Q12, Q15 THRU Q19, Q22, Q23 Q26, Q27, Q30, Q31, Q37 THRU Q4L ALL OTHERS ARE 2N744 TYPE.

Figure 1.11(b)   Rear View of Prototype TDCM

Figure 1.11(a)   Front View of Prototype TDCM

(A)
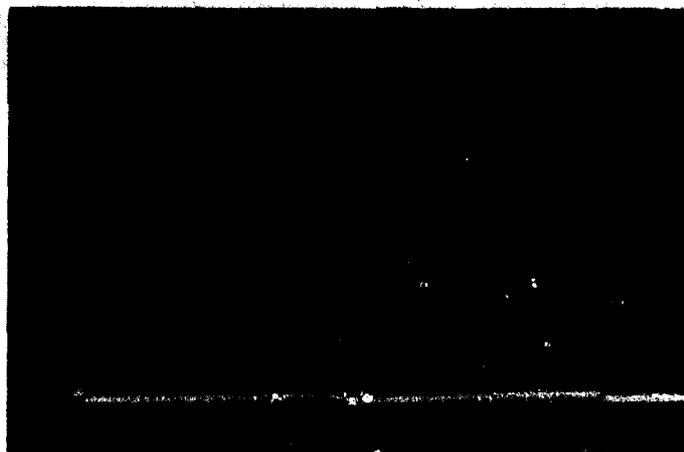
(B)
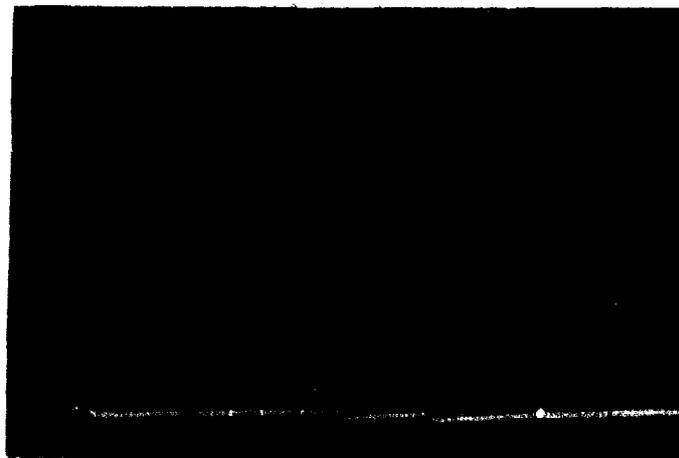
(C)

Figure 1.12 Calibration Traces of Channels A, B and C,
1 volt/cm, 2 μsec/cm

A plane wave explosive experiment was conducted to test the TDCM operation at shock pressure levels similar to those expected in the field. Composition-B explosive was used to generate a 450-kilobar shock wave in brass. On the back surface of the brass plate were placed three shock detectors (corresponding to 4, 5, and 6 of Figure 1.3). In addition a 1 cm thick disk of brass with a shock detector on its back surface (corresponding to 1 of Figure 1.3) was mounted on the back of the brass plate. The test then was an evaluation of the channel A portion of the TDCM. This test was successful and the TDCM circuit functioned properly.

Performance of the TDCM circuit appears adequate for field use. Modifications of the basic circuit can be made to accommodate specific applications without undue difficulties.

With the TDCM circuit the impedance-mismatch gage can operate as described, yielding shock velocity in the medium, degree of tilt of the shock wave, shock pressure in the medium, and information on the medium Hugoniot in the vicinity of the medium shock pressure.

Bonding Gage to Medium

A practical consideration which has not received sufficient attention to date is that of bonding the pressure gage to the medium at its emplacement position. A grout mixture is desired which will be convenient to use and will make a good bond or contact between the medium and the gage in its drill hole. More important, a grout mixture is required whose Hugoniot matches that of the medium. If the grout has a shock impedance much different from that of the medium then a significant perturbation may be made on the pressure measurements. The preparation of grout mixtures with Hugoniots matching those of a given rock medium, at least over a small range of pressures where a measurement is contemplated, is felt to be a relatively easy task. An analysis[17] of the synthesis of Hugoniots of multi-component materials has indicated how the grout preparation problem may be approached.

Shock Pressure Measurements About Nuclear Explosions

The impedance-mismatch gage as described above has never been used to measure shock pressures in a field experiment. The principal reasons for this have been (1) that no adequate electronic circuitry, such as the TDCM, was available for proper recording of pressure gage signals, and (2) that no opportunity has arisen where an impedance-mismatch gage could be placed near an underground explosion for a meaningful evaluation of its performance. Now that the impedance-mismatch gage has been developed, it is ready for field trials. Measurements of peak shock pressure will be attempted at the 1-, 0.6-, and

0.4-megabar pressure levels using impedance-mismatch gages in a scheduled nuclear explosion (Shoal) in granite.

As a result of research conducted on the impedance-mismatch gage, simplified shock pressure gages have been fabricated, tested, and used in field experiments. Shock pressures created by buried nuclear explosions have been successfully measured with these gages. However, in each case where a simplified gage was used, no absolute measure - in the sense of that derived from an impedance-mismatch gage - of shock pressure was possible. Rather, to derive shock pressures from measurements it was necessary to make the assumption that the medium Hugoniot was known. The desirability of a gage which gives direct measurements of shock pressure is clear, for with this type of gage the reliance on possibly erroneous assumptions regarding medium Hugoniots is avoided and, to a certain extent, the requirement of extensive laboratory determinations of medium Hugoniots is eliminated.

To date, 23 attempts have been made with simplified gages to obtain peak shock pressures in the hydrodynamic region about nuclear explosions. Except for one in granite rock, all measurements were made in desert alluvium, a porous, weakly consolidated soil. Of the 23 measurements, the one in granite and 14 in desert alluvium are considered reliable and the remainder are felt to be of doubtful or little value.

In desert alluvium, shock pressures were measured using Plexiglas gages placed in vertical drill holes to the same depth as that of the explosion. The choice of Plexiglas for gage material was dictated by the fact that it is not possible to machine and prepare a sample of poorly consolidated alluvial soil for use in a pressure gage and by the fact that the Hugoniot of Plexiglas matches reasonably well that of desert alluvium over a workable range of pressures.

The difficulty of not being able to machine and work soil cores will probably persist, and any shock pressure gage used in soil measurements will probably require a substitute material which can be worked and whose Hugoniot is as similar as possible to that of the soil. In view of this, it will be necessary to make laboratory determinations of soil Hugoniots so that suitable substitute materials can be selected. Materials which can serve as substitutes for soil may be obtained by reviewing all available data on Hugoniots in the hope of finding one which is nearly the same as that of the soil medium, or by synthesizing[17] materials so that their Hugoniots match the soil Hugoniot at least over a range of pressures where measurements are contemplated.

The reasonably close match between Hugoniots of Plexiglas and desert alluvium is shown in Figure 1.13. From measurements of shock velocity in Plexiglas, shock pressure in Plexiglas is obtained (solution of Equations 1.1 and 1.6). This pressure then is taken to be the shock pressure in desert alluvium at the position of the Plexiglas gage.

DESERT ALLUVIUM

△ ρ_o = 1.54 gm/cm^3, REF. 21

◇ ρ_o = 1.80 gm/cm^3, REF. 21

● ρ_o = 1.38 to 1.77 gm/cm^3

EXTRAPOLATION OF REF. 13 DATA USING
$V = 2.87 + 1.42\ u$

MEASURED PLEXIGLAS HUGONIOT
ρ_o = 1.18 gm/cm^3
REF. 13

SHOCK PRESSURE (KILOBARS)

PARTICLE VELOCITY mm/μsec
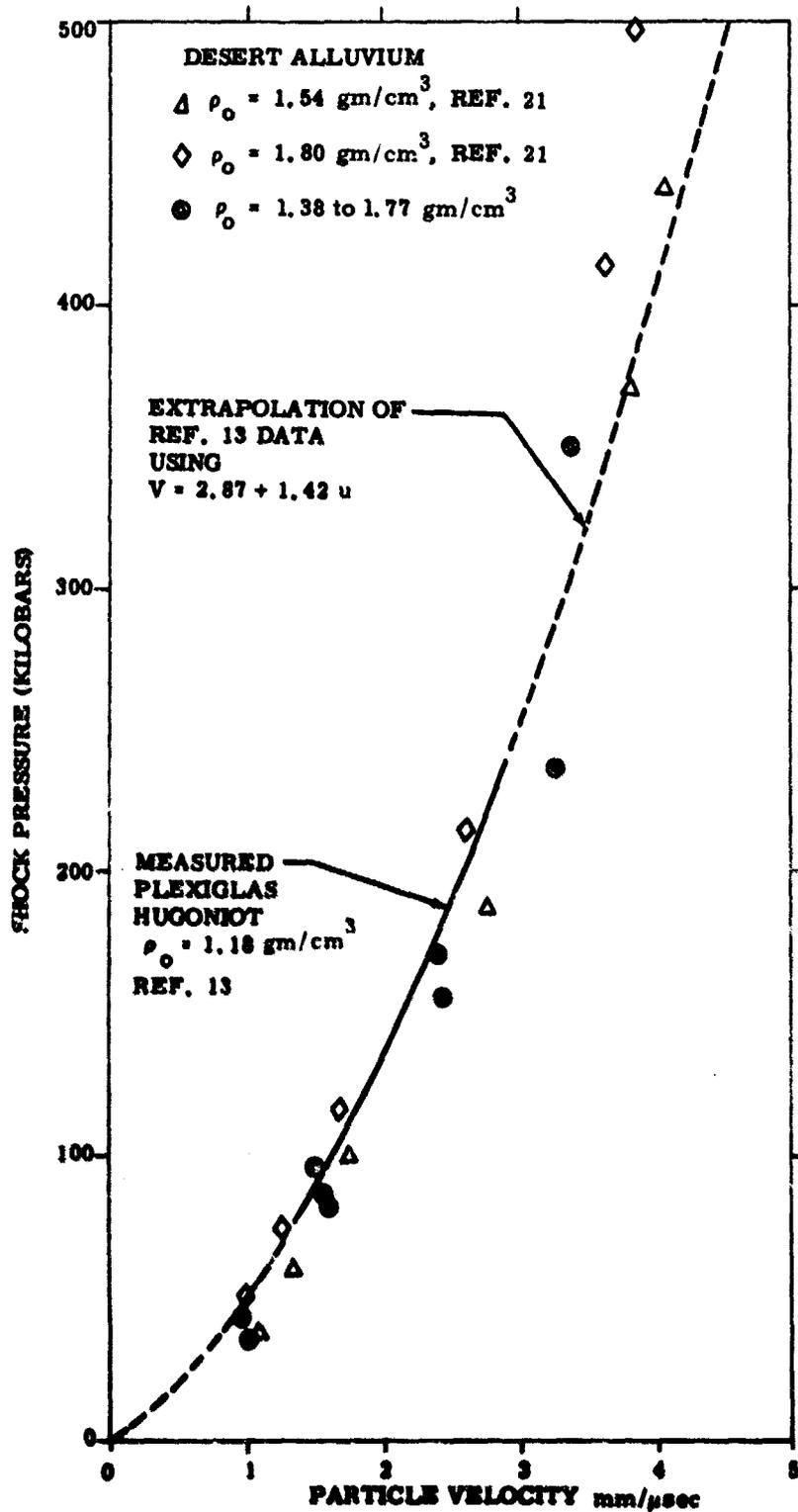
Figure 1.13 Comparison of Hugoniots of Desert Alluvium and Plexiglas

Two types of gages have operated successfully in desert alluvium, one a rectangular slab gage and the other a ring-type gage. The Plexiglas slab gage is shown in Figure 1.14. One or more pairs of PZT shock detectors identical to those of Figure 1.4 were employed in each Plexiglas gage of Figure 1.14. A pair of detectors were accurately spaced about 2 inches apart along the direction of shock propagation and spaced about 1 inch apart along a direction transverse to that of shock wave propagation.
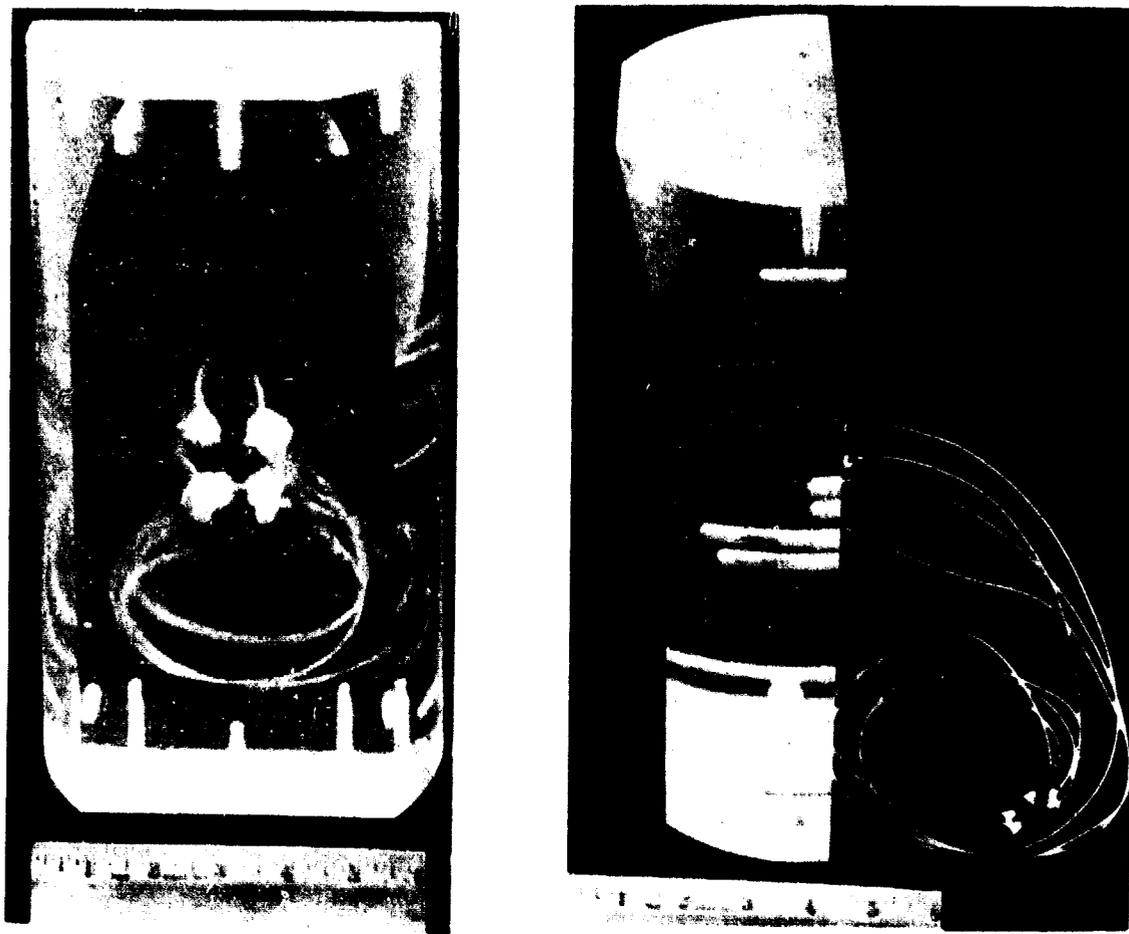
Figure 1.14 Front and Side Views of Plexiglas Slab Gage Used in Desert Alluvium

Attached to and above the slab gage are a gyroscope and a motor to rotate and position the gage near the bottom of its vertical hole. With gyroscope drift taken into account the gage may be aligned azimuthally to within 1 degree. After the slab gage is positioned the drill hole is filled with native soil from the same area in which the gage hole was drilled.

To avoid the great inconvenience of orienting the slab gage, a ring gage has been developed[18] which requires no azimuthal alignment. The manner of ring gage operation is illustrated in the diagram of Figure 1.15. Two cylindrical rings of PZT are the shock detecting elements. Electrical leads are attached to the inner and outer radii of each PZT ring and taken out to the surface through the axially located tube. Details of construction and operation may be found in Reference 18. In Figure 1.16 is shown a raster oscillogram of ring gage signals obtained in a field experiment with a buried explosion in desert alluvium. The amplitude of the pulses derived from the PZT rings is about 300 volts. These pulses were obtained at a position where the shock wave pressure was 150 kilobars. Timing pips on the record occur at 1 μsec intervals.
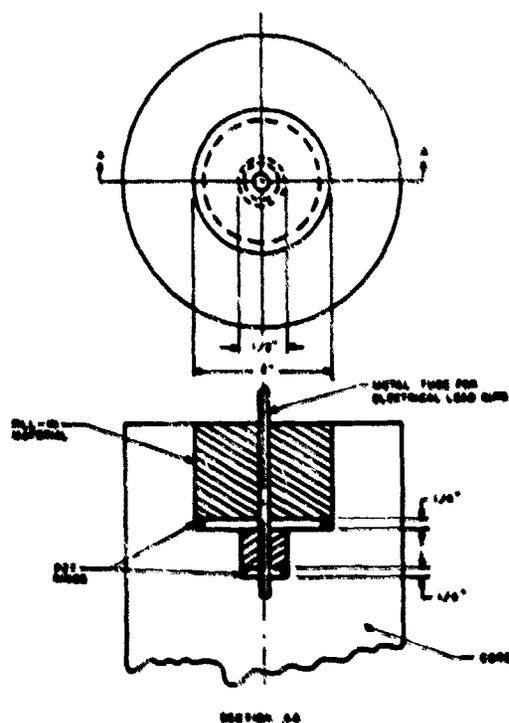
Figure 1.15 Diagram of Pressure Gage With PZT Rings

Figure 1.16 Raster Oscillogram of Signals From PZT Ring Gage

Shock pressure data obtained to date from the two types of gages used in desert alluvium are plotted in Figure 1.17 as a function of scaled distance from explosion center. Each open circle point represents a shock pressure measurement from one explosion. The triangles and squares occurring in pairs signify two pressure measurements from a single explosion. The solid curve of Figure 1.17 is obtained by calculation using methods described in Reference 8. Data of Figure 1.17 have also been plotted in Figure 4.11 of this report for comparison with Bishop's calculations.

The reliability of shock pressure measurements in desert alluvium may be ascertained by comparison of data with the dotted curve of Figure 1.17. This dotted curve is an indirect and less accurate indication of shock pressure versus distance obtained from independent measurements of shock wave position as a function of time.

Shock time-of-arrival data obtained from buried explosions in desert alluvium are shown scaled in Figure 1.18. The solid curve of Figure 1.18 is calculated by methods given in Reference 8 and the dotted curve is a best fit to all the data. An analytical expression was obtained for the dotted curve from which, by differentiation, shock velocity as a function of distance from explosion center was estimated. Since shock velocity is now known at any given position, the shock pressure at any position can be determined from the Hugoniot curve (Figure 1.13 , 1.20, or 1.21) of the medium. Shock pressure as a function of distance from the explosion estimated in this manner from shock time of arrival data is the dotted curve shown in Figure 1.17. Since direct shock pressure measurements are consistent with the independent shock wave time-of-arrival measurements, it is believed that the shock pressure data are reliable and descriptive of spherical shock wave propagation in desert alluvium.

Data of Figures 1.17 and 1.18 were obtained from various explosions among which the maximum ratio of two explosion energies was in excess of 50. Since data of Figures 1.17 and 1.18 scatter nicely about a single curve in each figure, the measurements verify that spherical shock phenomena scale as the cube-root of energy release, W, expressed in kilotons.

Scatter in the data of Figures 1.17 and 1.18 is attributed to lack of precise values of explosion energy release, to experimental errors in measurement, to the possibility that all explosions were not perfectly spherical, and also to the fact that the medium Hugoniot was very likely not the same for all explosions.
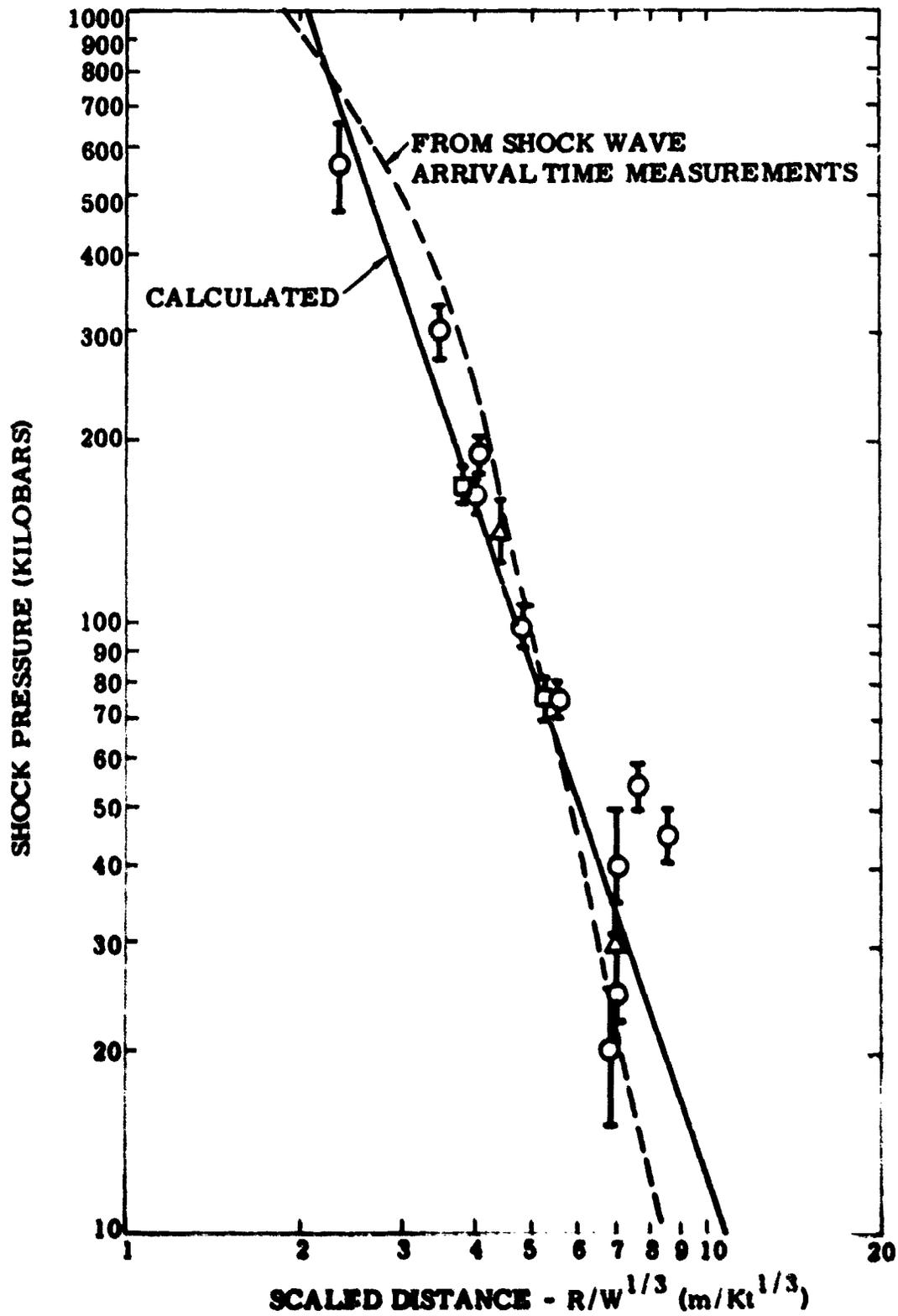
Figure 1.17 Peak Shock Pressure Versus Scaled Distance
From Explosions in Desert Alluvium
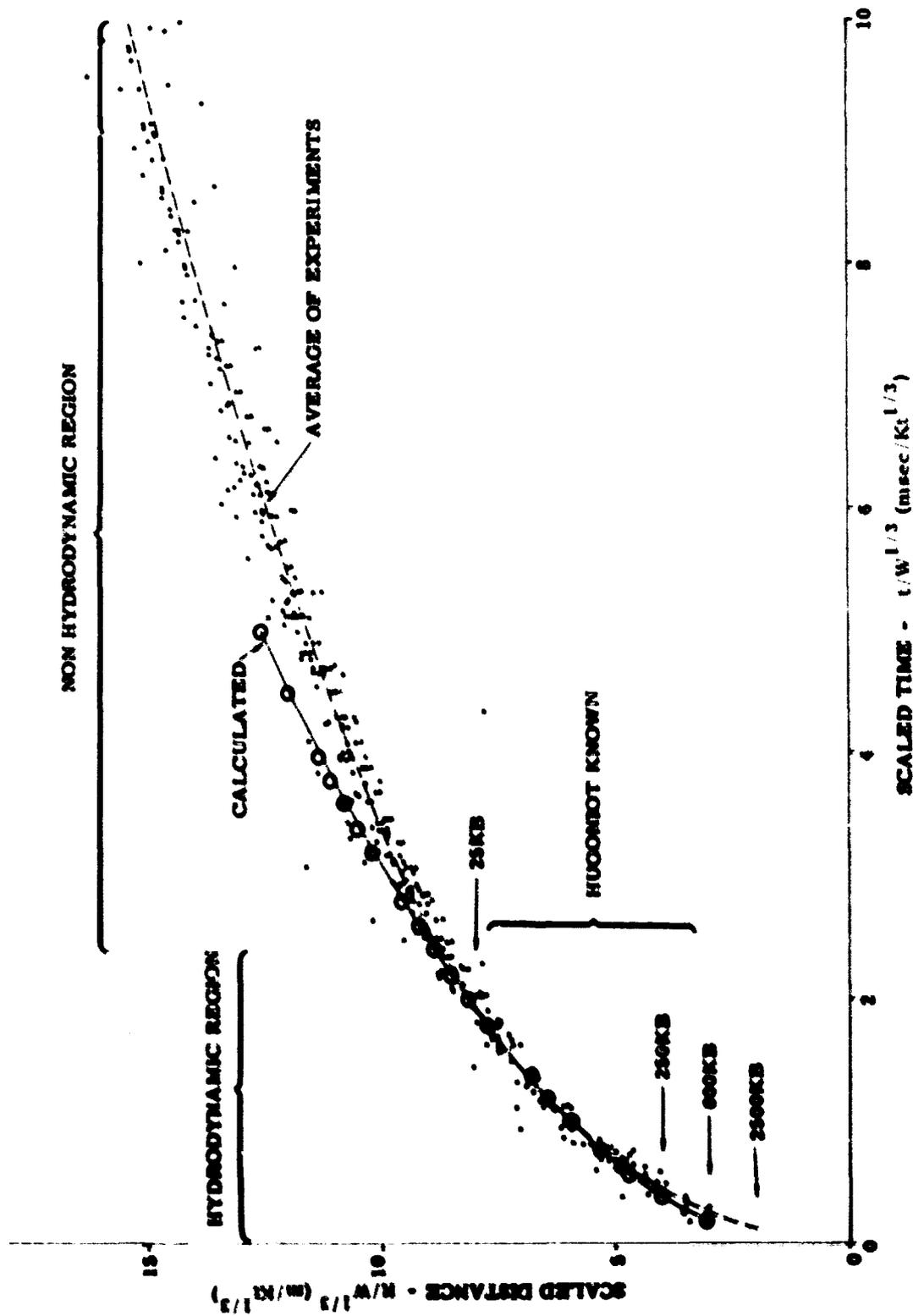
Figure 1.18 Scaled Position Versus Scaled Arrival Time for Spherical Shock Waves in Desert Alluvium

There is good evidence (see discussion below on Hugoniots of porous soils) to indicate that relatively small changes in the porosity or water content of desert alluvium or any other porous medium make significant changes in the Hugoniot. Shock pressure gages used to obtain the data of Figure 1.17 were made of Plexiglas whose Hugoniot is similar to that of completely dry desert alluvium. It is possible that the Hugoniot of Plexiglas was no longer a good match for the Hugoniots of desert alluvium in those experiments where the porosity and moisture content of the medium were appreciably different from those assumed (Figure 1.13 or 1.20). If this is true, then the data of Figure 1.17 will require some correction after the influence of porosity and moisture content on the Hugoniot of desert alluvium is known. Another observation that water content may significantly alter the medium Hugoniot has been made[19] by correlating time-of-arrival data from various experiments with some gross measure of water content in the medium obtained from drilling logs. If experiments are grouped as "dry," "damp," and "average" according to moisture condition indicated for the medium, the three separate distance-time curves, similar to the one shown in Figure 1.18, are obtained from the data for desert alluvium. A best fit made to each of these three groups of data reveals a smaller standard deviation than that for the average curve given in Figure 1.18 when all data are taken together. The interpretation of this result is that moisture content in the medium does noticeably alter the medium Hugoniot.

A somewhat different modification of the impedance-mismatch gage was used to measure peak pressure of a shock wave generated by a nominal 5-kiloton nuclear explosion (Hardhat) in granite. For construction of the gage a core of granite was obtained from near the point of measurement and machined into a circular disk 7 inches in diameter and 2 inches thick. The granite disk was placed in direct contact with a 7-inch-diameter, 2-1/2-inch-thick disk of (2024) aluminum as shown in Figure 1.19. Shock transit times through each disk were recorded with PZT crystals placed at the granite front surface, where contact with the shock was first made, at the granite-aluminum interface, and at the aluminum back surface. Three sets of three crystals positioned in this manner and on axes 120 degrees apart were installed as insurance against the possible failure of one or more crystals. If at least two of the three sets of crystals functioned without failure, then, in addition to shock velocity in each disk, the tilt of the shock wave with respect to the longitudinal axis of the circular disks would be obtained from Equation 1.8. One cable for each of the three sets of crystals was used to bring out the signals.

The gage assembly was inserted at the bottom of a drill hole whose axes made an angle of 36 degrees with a line joining the gage position and the explosion center. The hole was then filled with a grout whose sonic impedance matched that of granite. Shock impedance of the grout mixture was not known.

PUSH ROD
2" PIPE

CONNECTOR PLATE

GAGE CANISTER

ALUMINUM DISK (7" DIAM. X 2 1/2" THICK)

3 SHOCK DETECTORS
AT GRANITE ALUMINUM
INTERFACE

3 SHOCK DETECTORS
AT ALUMINUM
BACK SURFACE

GRANITE DISK
(7" DIAM. X 2" THICK)

FRONT SURFACE
SHOCK DETECTORS
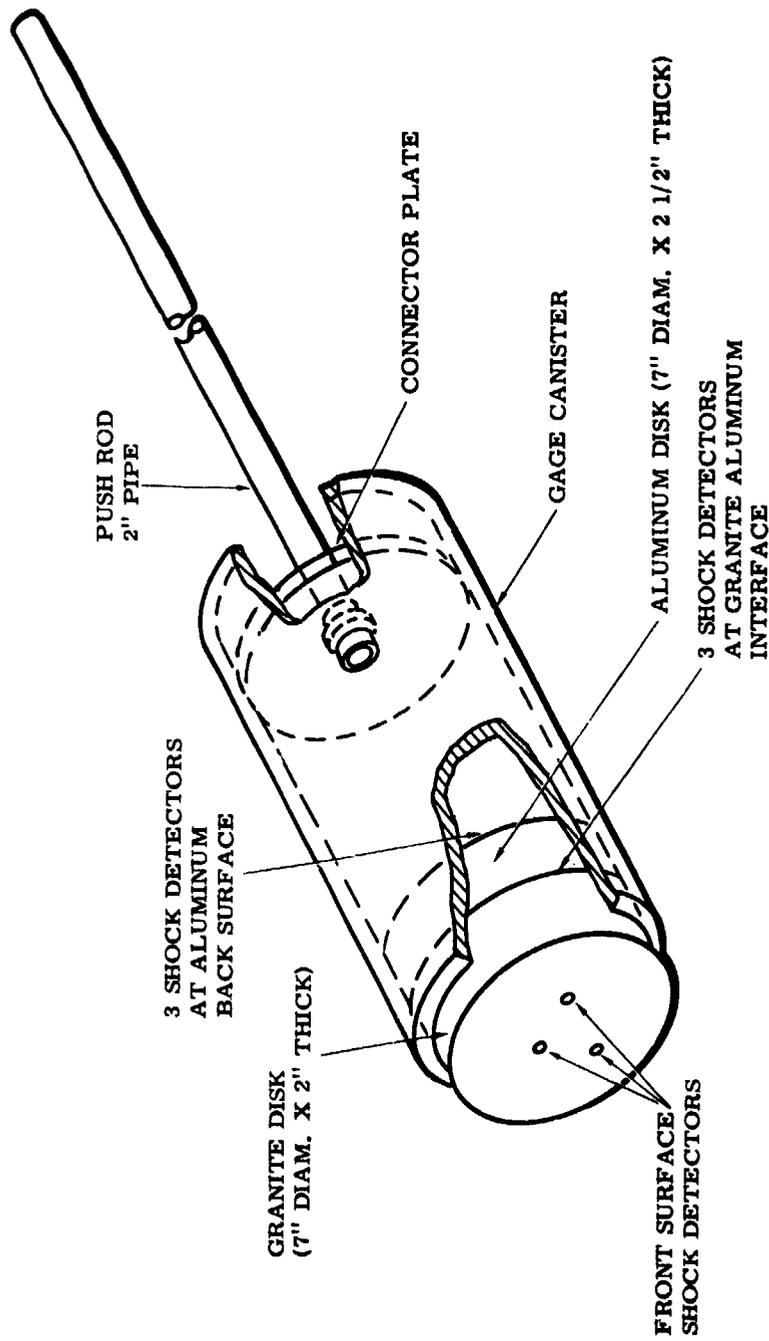
Figure 1.19   Illustration of Shock Pressure Gage Used in Granite

41

Insufficient time was available prior to the experiment to prepare a grout whose Hugoniot matched that of granite at the pressure level expected.

Because the instrument drill hole was not truly radial it was desirable to obtain a measurement of shock tilt. It was for this purpose that the three sets of three shock detectors were employed.

Results of the granite shock pressure experiment are shown in Table 1.1. From measured shock velocities pressures were determined using Equations 1.1 and 1.6.

TABLE 1.1

Shock Pressures From a Nuclear Explosion in Granite

Disk	Density (gm/cm^3)	Shock path (cm)	Transit time (μsec)	Shock velocity $(mm/\mu sec)$	Pressure in disk (kb)
Granite	2.68	4.07	6.27	6.48	450 ± 50
Aluminum	2.79	5.08	6.10	8.33	514 ± 100

The shock wave pressure measured in granite during the Hardhat explosion is consistent with an independent measurement made by Lombard[7] at a nearby position.

It must be noted again that the pressures listed in Table 1.1 are not direct measurements but were deduced from shock velocities by assuming that the Hugoniots for granite[2] and aluminum[1] were known.

The purpose of placing an aluminum disk behind the granite disk is now seen to be an attempt to check the validity of the assumption regarding the granite Hugoniot. If the Hugoniot assumed for granite were the same as that for the granite disk in the gage, then the reflection Hugoniot for granite (Equation 1.7), passing through the measured granite pressure point, would intersect, in a P-u plot such as Figure 1.2, the accurately known aluminum Hugoniot (Equation 1.6) at the pressure measured in the aluminum disk. Apparently the Hugoniot assumed for granite was correct since the 514-kilobar pressure measured in aluminum was within experimental error of the 540 kilobars indicated by the solutions of Equations 1.5 and 1.6.

For a more comprehensive description of the hydrodynamic measurement performed on the Hardhat experiment, Reference 8 should be consulted.

Aside from experimental errors it is seen from the measurements of shock pressure performed thus far that the greatest uncertainty associated with the data resides in the assumption that the medium Hugoniot is well known. Accuracy of the shock pressure data from experiments in desert alluvium

depends on the validity of the assumption that the Hugoniot of in situ desert alluvium is the same as the laboratory determined Hugoniot of dry reconstituted alluvium samples and nearly the same as the Hugoniot of the Plexiglas used in gages. As pointed out, there are strong indications that these assumptions for desert alluvium are not absolutely correct because the moisture content of the medium was not zero for all the field experiments but apparently varied. This variation from zero moisture content results in a Hugoniot different from that for a perfectly dry material. Accordingly, the desert alluvium pressure data have inherited a certain unknown inaccuracy resulting from the Hugoniot assumption.

The granite pressure of Table 1.1 is consistent with the pressure measured in aluminum and indicates that within experimental error the Hugoniot assumed (least square fit of available data) for the in situ medium was correct. However, had the granite and aluminum pressures been widely inconsistent, no pressure data would have been obtained and the only information provided by experimental results would be that the assumed Hugoniot was probably incorrect.

If there is a high degree of confidence that a medium Hugoniot is well known then there is absolutely no need for attempting elaborate and difficult pressure measurements. All that is required is a measurement of shock wave arrival time at various positions from an explosion center to obtain a distance-time curve such as that shown in Figure 1.18. Since the medium Hugoniot is considered well known and time-of-arrival measurements can be made simply and accurately, shock pressure may be deduced at various positions from the explosion as was done to obtain the dashed curve of Figure 1.7. However, it seems unlikely that we will ever have this much confidence in a Hugoniot assumed for any geologic material in situ.

To make our shock pressure measurements more meaningful, it is important to divorce the measurement technique from any assumptions regarding the medium Hugoniot and to attempt some relatively direct measurements of shock pressure. Hopefully, the impedance mismatch pressure gage can accomplish this task, at least in rock type geologic media.

Hugoniots of Porous Earth Materials

In conjunction with development of shock pressure gages for use in soil media, an examination of soil Hugoniots has been necessary. Since, as mentioned previously, cores of poorly consolidated soils cannot easily be worked and prepared for fabrication of shock pressure gages, a particular material whose Hugoniot is very nearly the same as that of the soil in question is substituted in the gage. After laboratory

determination of the soil Hugoniot, the properties required by the substitute material Hugoniot are made known. Hugoniot data on soils are also necessary for performing calculations of shock wave propagation in these media.

Data have been obtained on the Hugoniots of desert alluvium, volcanic tuff, and a medium called playa. Volcanic tuff is a porous rock, well consolidated (relatively well cemented and firm). Desert alluvium is a very poorly consolidated (friable) soil, and playa is an alluvial soil relatively well consolidated. These materials are representative of the media in which shock-pressure measurements are currently being made. Core samples of desert alluvium and of tuff which underlies this alluvium were obtained at various depths from Area 3 of the Nevada Test Site (NTS). Playa samples were obtained from Frenchman Flat, Area 5 of NTS.

Sample preparation of these materials and the techniques employed to obtain Hugoniot data are given in another report.[20] Majority of the data are from samples that were completely dry, i.e., any moisture contained in the samples obtained from cores was removed by baking before Hugoniot experiments were conducted. The remainder of the data are results of investigations into the effects of porosity and water content on the Hugoniot of the dry material. Data are summarized in Table 1.2 at the end of this section.

In Figure 1.20 are plotted data for dry desert alluvium. Porosity of this material is about 30 percent, and the initial density of samples ranges between the values of 1.38 and 1.80 gm/cm^3. The squares and triangles of Figure 1.20 represent data from the earlier work of McQueen and Marsh.[21] Shock wave velocity and particle velocity behind the wave, plotted in the figure, indicate raw data from which shock pressure and density may be determined using Equations 1.1 and 1.2. It is pointed out that the squares and triangles of the figure are data obtained from soil samples taken from one location in the medium. Circles represent data from samples taken at different locations in the same medium, which probably accounts for the scatter in the data, since the alluvium is highly inhomogeneous. Also shown in Figure 1.20 for comparison is a line through Hugoniot data[1] for aluminum and a line estimated[17] for nonporous desert alluvium. A synthesized Hugoniot[17] for dry desert alluvium of 40 percent porosity is also plotted on the figure.

Curves may be drawn through the data of Figure 1.20 in a number of ways. We have drawn two curves to designate the range of densities likely to be encountered in a desert alluvium medium and for which there are some data. It is seen that most of the data fall within that region of the figure bordered by the two curves. Hugoniot data and the curves of Figure 1.20 have been replotted in Figure 1.21 to show shock pressure as a function of relative specific volume, v/v_o, where v is shocked volume of the medium and v_o is initial specific volume. For the dry samples of alluvium whose initial density, ρ_o,
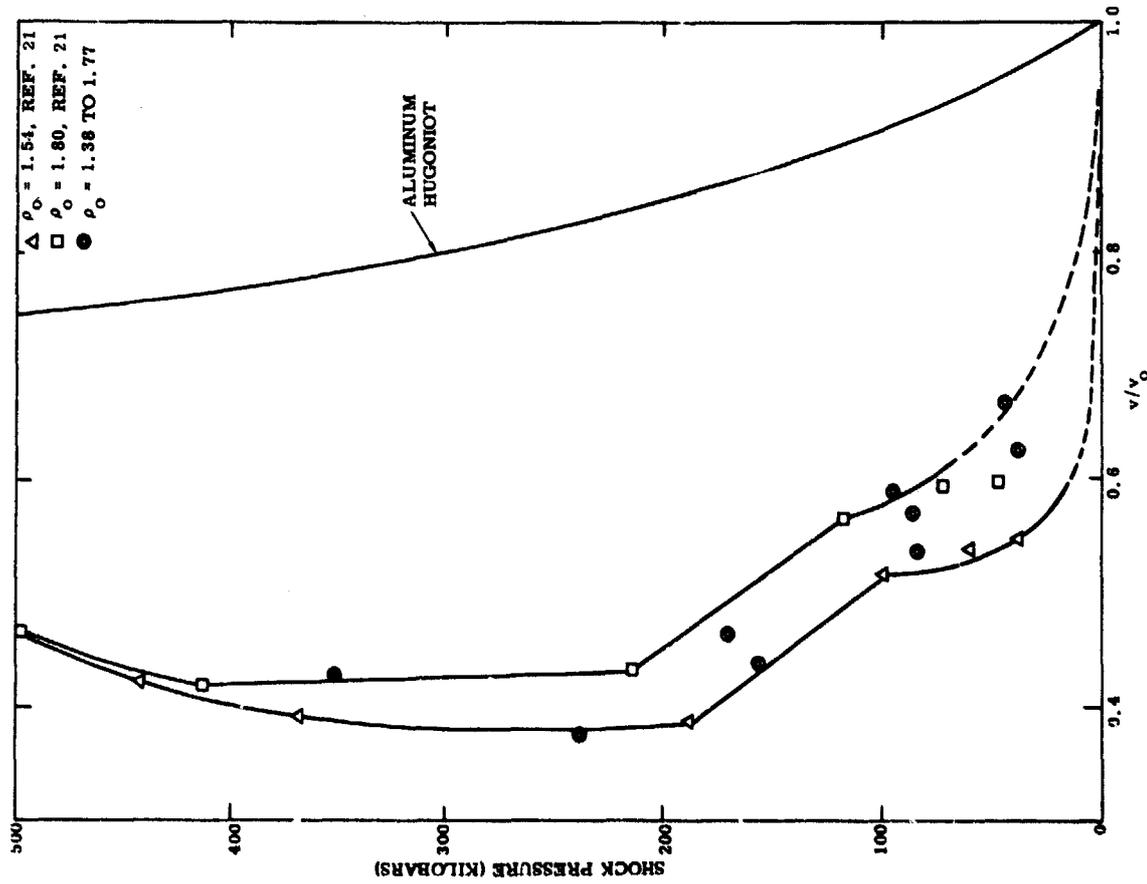
Figure 1.21 Desert Alluvium Hugoniot, Shock Pressure Versus Relative Specific Volume
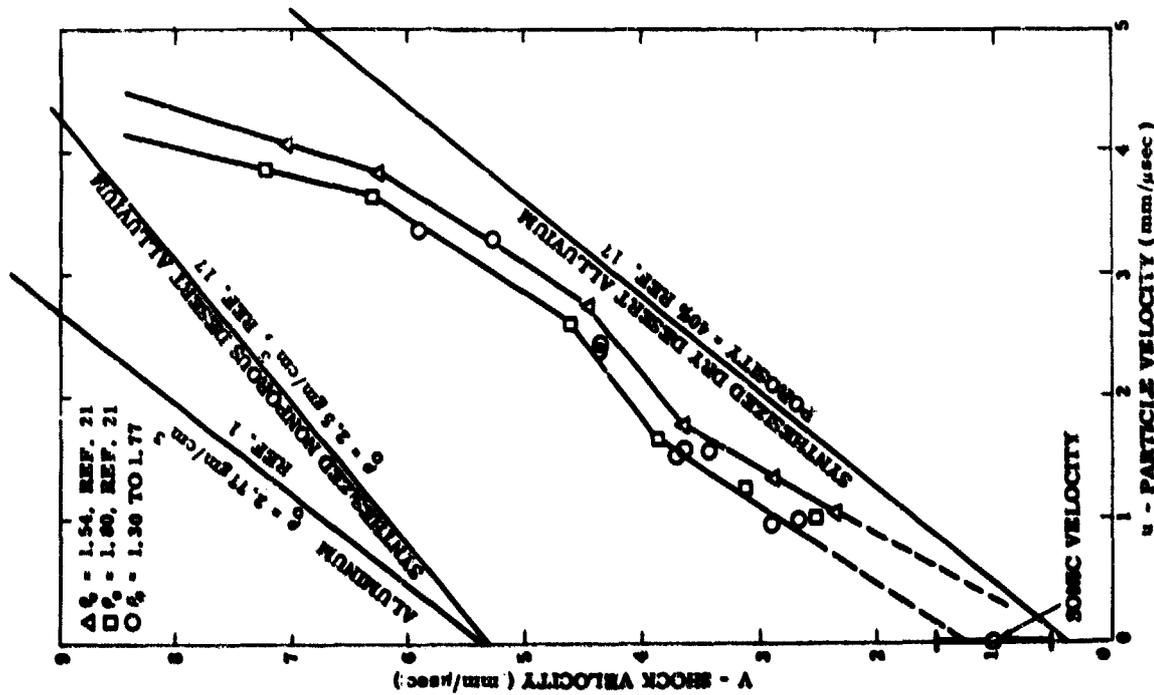
Figure 1.20 Desert Alluvium Hugoniot, Shock Velocity Versus Particle Velocity

45

was 1.8, the derived[21] grain density was 2.46 gm/cm^3, and for the samples of density ρ_o = 1.54, grain density is given as 2.24 gm/cm^3.

By comparison with Hugoniots of most other (nonporous) materials the Hugoniots of desert alluvium are most unusual. It is seen that the alluvium Hugoniots are double valued functions of density and that the Hugoniot has a region of pressures over which the slope,$(\partial P/\partial \rho)$, of the curve is negative. Hugoniots of porous metals have been found[22,23] which demonstrate similar characteristics.

A qualitative explanation of the shape of alluvium Hugoniot curves may be as follows. In porous soil individual particles of density ρ_G are separated by void spaces so that the average density is ρ_o. A shock wave passing through the material does work by collapsing the void spaces, by overcoming the internal friction between particles and by deforming and compressing the particles. The increase in internal energy (Equation 1.3) as a result of shock compression is greater for a porous medium than for a similar nonporous medium when shock pressures in each medium are equal. This may be seen from the diagram of Figure 1.22.
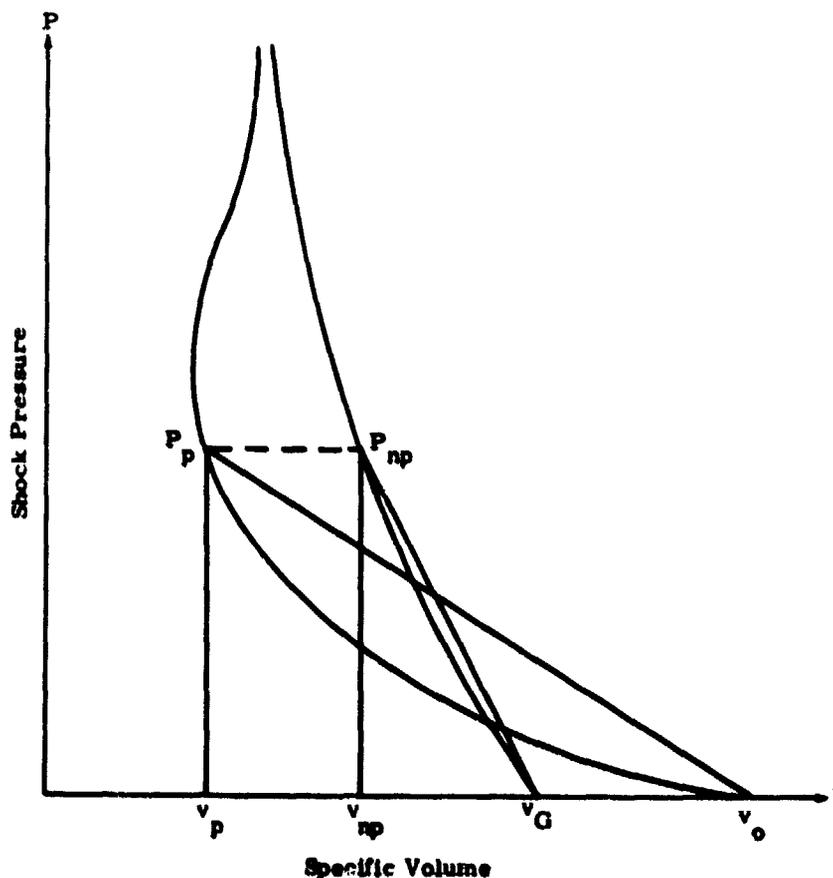
Figure 1.22 Comparison of Energy Deposition by Shock Waves in Porous and Nonporous Solids

The increase in specific internal energy given by Equation 1.3 is represented in Figure 1.22 by the triangular area, $v_G P_{np} v_{np}$, for the nonporous material and is less than the area $v_o P_p v_p$ for the porous

material. Since the increase in internal energy behind the shock wave is equal to the increase in material kinetic energy (from Equations 1.1 and 1.2) it is also seen that the kinetic energy imparted to a porous material will be greater than that imparted to a similar nonporous material when shock pressures in both materials are equal. It is for this reason that porous Hugoniot curves such as shown in Figure 1.20 will be below the Hugoniot of the nonporous material. Consequently, in porous materials similar to desert alluvium, internal energy and particle velocity will be greater and shock wave velocity will be less than that produced by a shock wave of the same pressure in the material with no void spaces. Because internal energy in the porous material is greater than in the nonporous material, temperatures behind the shock waves in porous materials will be greater. These higher temperatures in porous materials may have effects such as shock-induced phase changes at pressures lower than those at which phase changes occur in nonporous materials. Also the higher temperatures resulting in porous media from shock compression may account for the region of negative slope, $(\partial P/\partial \rho)$, demonstrated by the Hugoniots in Figure 1.21.

The shape of the alluvium Hugoniots in Figure 1.21 between 0 and 100 kilobars is possibly described by the collapsing of void spaces, the principal mechanism of medium deformation in this pressure range. A small change in shock pressure results in a large change in specific volume. Between about 100 and 200 kilobars phase changes are being initiated by shock waves passing over particles of the medium. At pressures in excess of 200 kilobars the effect of shock heating is sufficiently intense in the porous material that increases in shock pressure are accompanied by decreases in density. Also in this pressure region the two alluvium Hugoniot curves appear to be coalescing, i.e., as shock pressure increases above about 300 kilobars fewer and fewer void spaces remain, and a given shock pressure compresses both materials, of different initial density, to very nearly the same density. Eventually, at pressures of the order of half a megabar, both porous and nonporous materials are compressed to the same density by a shock wave of a given pressure. It may be that at some pressure greater than about 0.5 megabar the Hugoniot curves of porous alluvium are identical to a Hugoniot of a nonporous alluvium medium. It must be remarked that, in all the alluvium experiments conducted, space in the samples was occupied by air at atmospheric pressure. What influence this small mass of gas may have on the Hugoniot is not actually known.

While these qualitative speculations may not be particularly illuminating they serve to illustrate the complexity of phenomena involved and the difficulties likely to be encountered in formulating theoretical descriptions of porous soil Hugoniots.

The 0.5-megabar Hugoniot point for desert alluvium represents the upper limit of shock pressures attainable in laboratory experiments. It is practically impossible to generate pressures much higher than

this by conventional methods. As a consequence of this limitation additional Hugoniot information in the pressure region above 0.5 megabar must come from other sources such as experiments about nuclear explosions or theoretical investigations. While experiments with nuclear explosions will be considerably more difficult than laboratory experiments, shock pressures as high as 10 or even 100 megabars may be achieved and valuable Hugoniot and thermodynamic information can be obtained. Attempts[17,27,28,29,30] have been made to calculate Hugoniots of materials for shock pressures between 0.1 and 1 megabar; however, the successes of these methods have not been striking and great reliance cannot be placed on the calculated results. Much more work is required in the theoretical calculation of Hugoniots for geologic media, particularly those media with high void content.

An implication of the alluvium Hugoniot data shown in Figure 1.21 is that Gruneisen's parameter, $\Gamma = v(\partial P/\partial E)_v$, for desert alluvium is not a constant but likely a strongly varying function of specific volume, $v = \frac{1}{\rho}$. This implication is significant to theoretical calculations of spherical shock wave propagation in desert alluvium or other porous geologic media. In these theories[24,25] the Mie-Gruneisen equation of state, which contains the parameter Γ, is commonly invoked and Gruneisen's Γ is usually taken to be constant. While for many materials[1,10] Γ is nearly constant or only a slowly varying function of specific volume, the data for alluvium indicate that Γ is not constant but varies appreciably with specific volume.

Gruneisen's parameter for solids is analogous to the ratio of specific heats for gases and determines how rapidly pressure falls off behind the shock front and the amount of cooling experienced by a medium particle in adiabatic expansion. These processes are important in determining how rapidly peak shock pressure falls off with distance and the rate at which a shock wave is propagated from the explosion source.

From the alluvium data of Figure 1.21 estimates of Gruneisen's Γ and its variation with volume may be made in a number of ways. For example from the measured Hugoniot and the Dugdale-MacDonald or Slater relations[1] for Γ, values of Γ for desert alluvium may be computed. Also estimates of Γ may be obtained using the method of Al'tshuler[26] for porous iron. Evaluations of Gruneisen's parameter for desert alluvium by these various methods results in a confusing array of values.

Theoretical calculations[8,24,25] of spherical shock wave propagations in desert alluvium with constant value of Γ (both 0.5 and 1) have yielded predictions of shock position versus time which are generally in excellent agreement with experimental data (e.g., see Figure 1.15 and also Figure 2 of Reference 25). Since the desert alluvium Hugoniot data indicate that Γ is definitely not constant, one

wonders how the spherical shock calculations can give correct answers with constant values of Γ. It is not known whether agreement between calculations and data is fortuitous, whether shock position versus time is not sensitive to large changes in Γ demonstrated by alluvium, or whether the Mie-Gruneisen equation of state is not applicable to a porous soil medium. However, in order to have confidence in the calculations the Γ variation indicated by desert alluvium must be understood and its implications for theoretical results must be evaluated more fully.

Figure 1.23 shows data obtained for a volcanic tuff from Areas 3 and 16 of the Nevada test site. The dry tuff has a density of 1.46 gm/cm^3 and a porosity of 27 percent. These Hugoniot data are different from those reported by Lombard[2] for tuff from Area 12 at NTS. Lombard's tuff had a density of 1.7 and a porosity of about 24 percent. His data points for dry tuff lie above those shown for the dry tuff in Figure 1.23. Data for saturated tuff are also shown in Figure 1.23.

Figure 1.24 presents Hugoniot data for the playa medium of Area 5 at the Nevada test site. The density of samples received from the field was 1.47 gm/cm^3. Completely dry, these samples had a density of 1.41 gm/cm^3. The porosity of playa is estimated to be about 50 percent.

From Figures 1.20, 1.23, and 1.24, it is observed that between 50 and 200 kilobars the Hugoniots of dry desert alluvium, dry tuff, and playa are essentially identical.

In Figure 1.25 are shown the results of a few experiments with a fine, pure silica sand. These experiments were conducted to obtain information on the effects of porosity and water content on Hugoniots.

The silica sand used is composed of particles 80 percent of which have diameters less than 75 microns. Maximum particle size is about 150 microns. Grain density of the sand is 2.65 gm/cm^3, the same as that of crystalline quartz. For experiments, the sand was packed[20] to dry densities of 1.58 and 2.05 gm/cm^3. Corresponding porosities are 41 percent and 22 percent. It is seen that the higher density dry sand data lie above those of the lower density dry sand and in a direction toward the Hugoniot curve for crystalline quartz[32, 33] shown at the top of Figure 1.25. Also shown in the figure are data for water-saturated sand with a density of 1.98. Since the porosity of the water-saturated sand is the same as that of the lowest curve in the figure, it is seen that addition of water to fill the void space in this sand shifts the Hugoniot upward by a considerable amount, making the saturated sand much less compressible. Thus a decrease in porosity or an increase in water content of a porous material results in a higher shock pressure if the same relative density is achieved (see Figure 1.26).

Figure 1.24 Playa Shock Hugoniot

Figure 1.23 Shock Hugoniots of Wet and Dry Volcanic Tuff
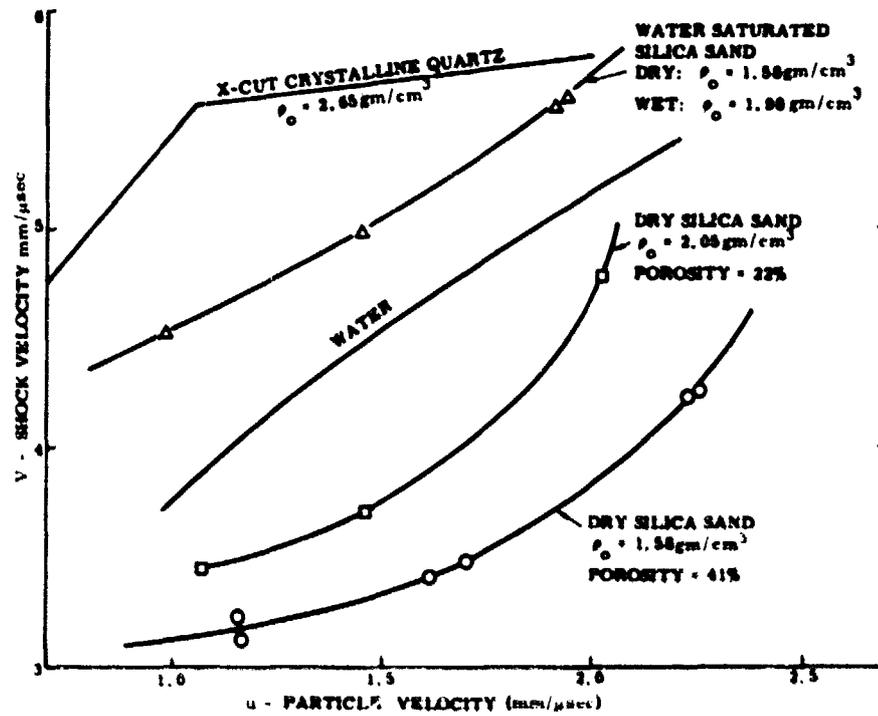
Figure 1.35 Silica Sand Hugoniot. Shock Velocity Versus Particle Velocity
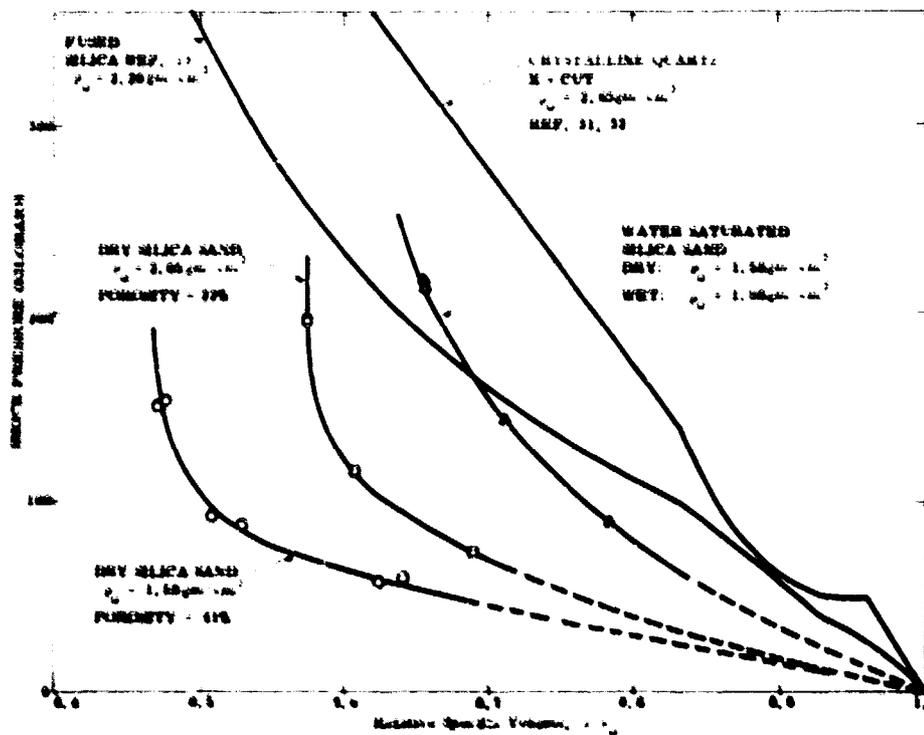
Figure 1.36 Silica Sand Hugoniot. Shock Pressure Versus Relative Specific Volume

In the close-in region about buried explosions in porous media, this means that stronger than expected shock waves will be propagated if the water content of the medium is greater than expected or if the porosity is less than expected. For experiments with explosions in porous media it will be essential to obtain information on the in situ porosity and water content.

Summary

An impedance-mismatch pressure gage has been developed which is capable of measuring peak shock wave pressures of amplitude 0.1 to 1 megabar in the hydrodynamic region about buried explosions. In addition the gage provides information on the medium Hugoniot and a means of measuring degree of tilt of the shock wave.

Techniques employed in measuring shock wave pressures have been tested, and shock pressures have been measured in experiments with buried nuclear explosions. By comparison with independent hydrodynamic measurements the shock pressure data have been shown to be reliable. These data are currently being employed to evaluate and refine theoretical calculations of spherical shock wave propagation in solid media.

Limited investigations have been made of Hugoniots of porous geologic media. Some unusual features of Hugoniots for porous media have been revealed which were not previously observed in Hugoniot studies of other (nonporous) materials. Moisture content and porosity are found to be significant parameters influencing the Hugoniot of porous materials. Possible applications of the Hugoniot data for porous media to theoretical calculations of shock propagation in these media have been pointed out.

TABLE 1.2

Hugoniot Data for Porous Earth Materials

ρ_0 (gm/cm^3)	V (mm/µsec)	u (mm/µsec)	P (kb)	ρ_o/ρ	Source
Dry Desert Alluvium - Porosity, 25 to 30%					
1.44	2.66	1.00	38	0.624	NTS, Area 3
1.58	2.90	0.97	44	0.666	NTS, Area 3
1.54	3.41	1.58	83	0.537	NTS, Area 3
1.50	3.65	1.57	86	0.570	NTS, Area 3
1.70	3.70	1.52	96	0.589	NTS, Area 3
1.46	4.35	2.45	156	0.437	NTS, Area 3
1.64	4.36	2.39	171	0.452	NTS, Area 3
1.38	5.25	3.27	237	0.377	NTS, Area 3
1.77	5.89	3.37	351	0.428	NTS, Area 3
Dry Volcanic Tuff - Porosity, 27%					
1.46	2.34	0.95	31	0.576	NTS, Area 3 (1500' depth)
1.46	3.70	1.58	85	0.573	NTS, Area 3 (1500' depth)
1.46	4.28	2.28	145	0.467	NTS, Area 3 (1500' depth)
1.46	4.30	2.50	153	0.405	NTS, Area 3 (1500' depth)
1.46	4.76	2.90	202	0.393	NTS, Area 3 (1500' depth)
1.46	2.68	1.00	39	0.627	NTS, Area 16
1.46	3.56	1.57	82	0.566	NTS, Area 16
1.46	4.03	2.50	147	0.390	NTS, Area 16
1.46	4.24	2.46	153	0.420	NTS, Area 16
Water Saturated Volcanic Tuff					
1.72	3.42	0.90	53	0.737	NTS, Area 16
1.74	4.26	1.45	108	0.660	NTS, Area 16
1.75	5.49	2.81	270	0.488	NTS, Area 3

TABLE 1.2 (Cont.)

$\bar{\rho}_o$ (gm/cm^3)	V (mm/μsec)	u (mm/μsec)	P (kb)	ρ_o/ρ	Source
Playa - Porosity, ~50%; Water Content, ~6%					
1.41*	2.70	1.04	40	0.615	NTS, Area 5
1.41*	4.40	2.48	148	0.436	NTS, Area 5
1.47	3.00	1.08	48	0.640	NTS, Area 5
1.47	2.58	1.04	39	0.597	NTS, Area 5
1.47	3.69	1.60	87	0.566	NTS, Area 5
1.47	4.47	2.52	166	0.436	NTS, Area 5
1.47	4.36	2.50	160	0.427	NTS, Area 5
1.47	5.07	3.54	264	0.302	NTS, Area 5
1.47	5.24	3.52	271	0.328	NTS, Area 5
Dry Silica Sand - Porosity, 40%					
1.58	3.13	1.17	58	0.626	
1.58	3.23	1.16	59	0.641	
1.59	3.42	1.61	88	0.529	
1.58	3.47	1.70	93	0.510	
1.56	4.26	2.25	150	0.472	
1.62	4.24	2.23	153	0.474	
Dry Silica Sand - Porosity, 22%					
2.03	3.45	1.07	75	0.690	
2.14	3.70	1.46	116	0.605	
2.03	4.78	2.03	197	0.575	
Water Saturated Silica Sand, Porosity, 40%					
2.03	4.53	0.98	90	0.784	
1.97	5.00	1.45	143	0.710	
1.95	5.63	1.94	213	0.655	
2.00	5.59	1.93	216	0.655	

*Samples obtained from 100-foot depth were completely dry.
Remainder of experiments were with samples from about
11-foot depth as received from field, sealed in wax containers.

LIST OF REFERENCES

1. Rice, M. H., McQueen, R. G., and Walsh, J. M., "Compression of Solids by Strong Shock Waves," Solid State Physics, Vol. 6, pp. 1-63, Academic Press, New York, 1958.

2. Lombard, D. B., The Hugoniot Equation of State of Rocks, UCRL-6311, Lawrence Radiation Laboratory, Livermore, California, February 1961.

3. Lombard, D. B., Lawrence Radiation Laboratory, Livemore, California, private communication.

4. Keough, D. D., and Bernstein, D., Pressure Transducer for Measuring Shock Wave Profiles, Technical Summary Report No. 2, SRI Project No. PGU-3713, Stanford Research Institute, Menlo Park, California, January 1963.

5. Anfinsen, L., et al., Stress Sensor Development, ARF Report No. K 6023-2, Armour Research Foundation of Illinois Institute of Technology, Chicago 16, Illinois, August 1962.

6. Schiffman, T. H., Armour Research Foundation of Il'inois Institute of Technology, Chicago 16, Illinois, private communication.

7. Lombard, D. B., and Power, D. V., "Hydrodynamic-Pressure Measurement in Granite Near an Underground Explosion," Bulletin American Physical Society, Series II, Vol. 8, No. 4, 1963.

8. Chabai, A. J., and Bass, R. C., Measurements on a Spherical Shock Wave in Granite, Final Report, Hardhat Event, SC-4741(RR), Sandia Corporation, Albuquerque, New Mexico, 1963.

9. Chabai, A. J., Bass, R. C., and Hawk, H. L., Section I of Close-in Phenomena of Buried Explosions, Third Semiannual Report, SC-4746(RR), Sandia Corporation, Albuquerque, New Mexico, November 1962.

10. McQueen, R. G., and Marsh, S. P., "Equation of State of Nineteen Metallic Elements from Shock-Wave Measurements to Two Megabars," Jour. Appl. Phys., Vol. 31, No. 7, July 1960.

11. Courant, R., and Friedricks, K. O., Supersonic Flow and Shock Waves, Interscience Publishers, Inc., New York, 1948.

12. Duvall, G. E., "Some Properties and Applications of Shock Waves, Response of Metals to High Velocity Deformation," Metallurgical Society Conference, Vol. 9, pp. 165-203, Interscience Publishers, New York, 1960.

13. Coleburn, N. L., The Dynamic Compressibility of Solids from Single Experiments Using Light-Reflection Techniques, NAVWEPS Report 6026, U.S. Naval Ordnance Laboratory, White Oak, Maryland, October 1960.

14. Levesque, A. L., and Smith, C. E., Report on the Development of a Shock-Pressure Gage, SCTM 39-63(72), Sandia Corporation, Albuquerque, New Mexico, February 1963.

15. Reynolds, C. E., and Seay, G. E., "Two-Wave Shock Structures in the Ferroelectric Ceramics Barium Titanate and Lead Zirconate Titanate," Jour. Appl. Phys., Vol. 33, No. 7, July 1962.

16. Caffey, T., Peak Pressure Gage Multiplexer, SCTM 235-62(54), Sandia Corporation, Albuquerque, New Mexico, November 1962.

17. Chabai, A. J., Synthesis of Shock Hugoniots for Rock Materials, Fifth Symposium on Rock Mechanics, p. 347, Pergamon Press, Headington Hill Hall, Oxford, 1963.

18. Hawk, H. L., A Transducer for Measuring Hydrodynamic Pressure, SCTM 124-63(54), Sandia Corporation, Albuquerque, New Mexico, May 1963.

19. Brownlee, R., Los Alamos Scientific Laboratory, Los Alamos, New Mexico, private communication.

20. Bass, R. C., Hawk, H. L., and Chabai, A. J., Hugoniot Data for Some Geologic Materials, SC-4903(RR), Sandia Corporation, Albuquerque, New Mexico, June 1963.

21. McQueen, R. G., and Marsh, S. P., Equation of State of Nevada Alluvium, GMX-6-491, Los Alamos Scientific Laboratory, Los Alamos, New Mexico.

22. Kormer, S. B., Funtikov, A. I., Urlin, V. D., and Kolesnikova, A. N., "Dynamic Compression of Porous Metals and the Equation of State with Variable Specific Heat at High Temperatures," JETP (USSR) Vol. 42, March 1962.

23. Krupnikov, K. K., Brazhnik, M. I., and Krupnikova, V. P., "Shock Compression of Porous Tungsten," JETP (USSR) Vol 42, March 1962.

24. Brownlee, R., and Cox, A., Los Alamos Scientific Laboratory, Los Alamos, New Mexico, private communication.

25. Holzer, F., Marks, R., and Butkovich, T., Sedan Yield and Shock Arrival Times, Memorandum UOPKA 63-6, Lawrence Radiation Laboratory, Livermore, California, April 1963.

26. Al'tshuler, L. V., Krupnikov, K. K., Ledenev, B. N., Zhuchikhin, V. L., and Brazhnik, M. L., "Dynamic Compressibility and Equation of State of Iron Under High Pressure, JETP (USSR) Vol. 34, April 1958.

27. Chaszeyka, M. A., and Porzel, F. B., Study of Blast Effects in Soil, Final Report ARF Project No. D119, Armour Research Foundation, Illinois Institute of Technology, Chicago 16, Illinois, August 1958.

28. Lyakhov, G. M., "Shock Waves in Multi-Component Media," Izvestia Akademii Nauk SSSR, Otdel Tekhnicheskikh Nauk, Mekhanika i Mashionostroyeniye, Moscow, No. 1, January 1959.

29. Seidl, F. G. P., Properties of Lollipop Granite, Memorandum UOPK 60-7, Lawrence Radiation Laboratory, Livermore, California, April 1960.

30. Brode, H. L., and Smith, A. E., Dynamic Properties of Matter Under High Stress-Thermodynamic Descriptions, Memorandum RM-3361-PR, The Rand Corporation, Santa Monica, California, November 1962.

31. Walsh, J. M., and Rice, M. H., "Dynamic Compression of Liquids from Measurements on Strong Shock Waves," J. Chem. Phys., Vol. 26, 1957.

32. Fowles, G. R., Shock Wave Compression of Quartz, Tech. Report 003-61, Stanford Research Institute, Menlo Park, California, October 1961.

33. Wackerle, J., "Shock Wave Compression of Quartz," Jour. Appl. Phys., Vol. 33, No. 3, March 1962.

Section 2

DYNAMIC RESPONSE OF GEOLOGIC SOLIDS TO LARGE AMPLITUDE STRESS WAVES

R. C. Bass, H. L. Hawk, and A. J. Chabai

Introduction

Propagation of large amplitude stress waves in solids is reasonably well understood when compressive stresses are in excess of about 100 kilobars. At these stress levels material rigidity is negligible, the stress wave is a steep-fronted shock, and a fluid model is used to describe wave propagation in the solid. For small amplitude stresses, say less than about 1 kilobar, an elastic model is often sufficient to describe the response of the solid. Between these limits, when amplitudes of compressive stresses are of the order of 1 to 100 kilobars, there is no general model which effectively describes the dynamic behavior of solids, particularly geologic solids.

In this range of nonfluid-nonelastic stresses phenomena such as yielding, fracture, strain rate and relaxation effects, anomalous compression and viscosity are expected to occur and may play dominant roles in determining the detailed structure of the compressive wave profile. Principally because an adequate model does not exist for the description of nonfluid-nonelastic behavior of geologic solids, there is at present no theory of spherical wave propagation from buried explosions which is capable of reproducing wave profiles that have been observed in experiments. It is believed that, once a reasonably realistic model were formulated, theoretical calculations of spherical wave disturbances could be made which would yield wave profiles similar to those observed in experiments.

If a model can be obtained allowing accurate calculations of nonfluid-nonelastic stress wave propagation, then elastic disturbances resulting from buried explosions in geologic media can be predicted and seismic phenomena may thereby be better understood.

To study nonfluid-nonelastic behavior of solids, use is made of plane compressive waves of large amplitude, σ, produced by explosives or by high velocity projectile impacts. In these experiments, a one-dimensional state of strain, $\epsilon = (1-\rho_0/\rho)$, is achieved. Often the single, step-function type of wave pulse introduced into the test specimen by these means is unstable because the condition for

57

stability,[1] $\partial^2\sigma/\partial\epsilon^2 > 0$, has been violated. As a result two waves are propagated through the specimen. Simple examples of some stress-strain curves leading to double wave profiles are shown in Figure 2.1.

IDEAL FLUID MEDIUM

(a)

FLUID MEDIUM, NONZERO ELASTIC LIMIT

(b)

MEDIUM WITH MIXED PHASE REGION

(c)

MEDIUM WITH ANOMALOUS COMPRESSION

(d)
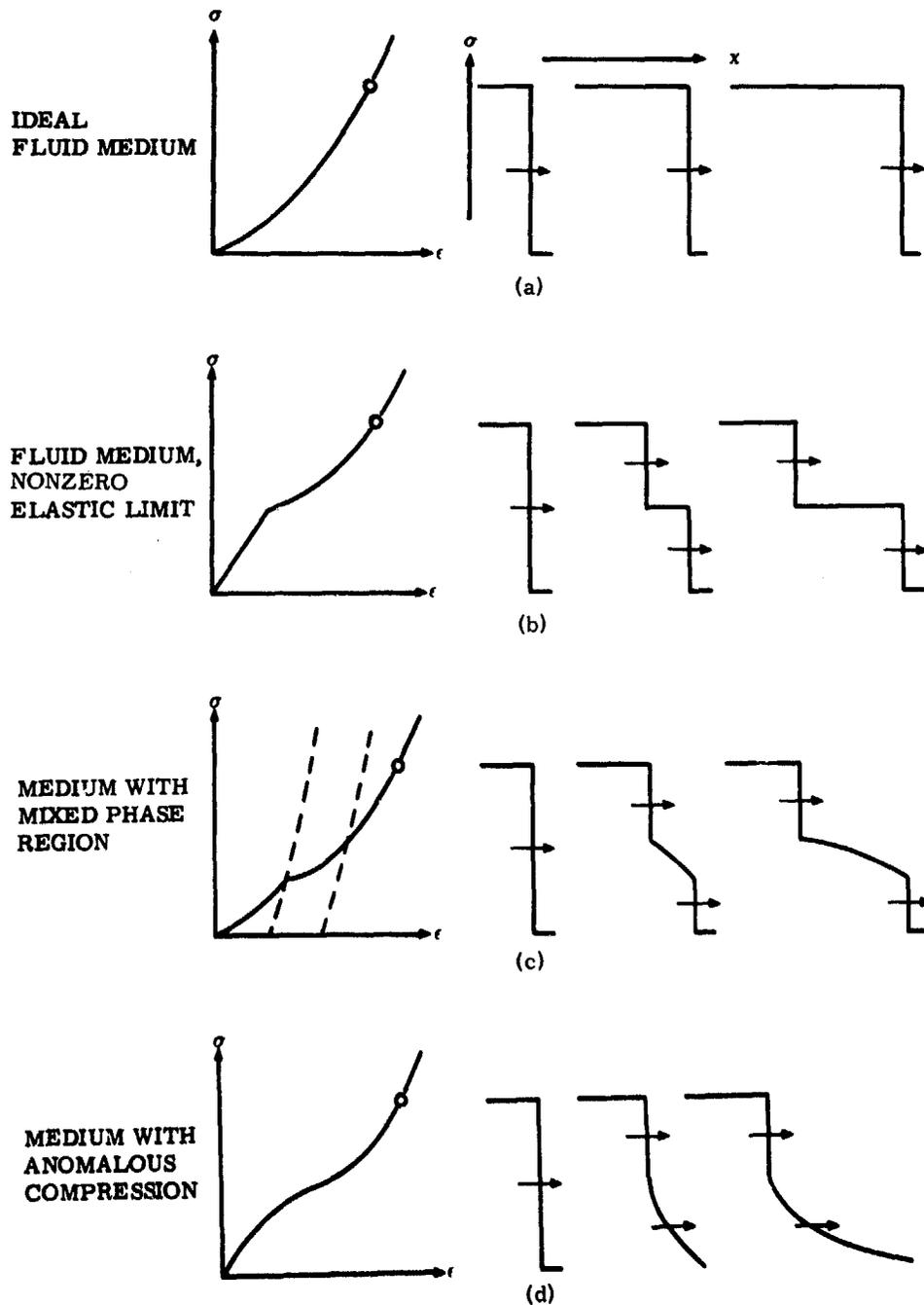
Figure 2.1   Some Stress-Strain Curves Leading to Two-Wave Profiles

Figure 2.1(a) is an example of a stress-strain relation or "Hugoniot" (Equation 1.5 of Section 1) for an ideal solid in which waves of any amplitude are stable. In Figure 2.1(b) is illustrated a

stress-strain curve exhibiting a finite yield strength or "Hugoniot elastic limit." This curve gives rise to a double wave structure consisting of an elastic precursor which propagates with the sonic velocity of the specimen and a second higher amplitude wave of slower velocity. Double wave profiles resulting from yielding have been observed in metals,[2, 3, 4] in quartz,[5, 6] and also in rock materials.[7]

A double wave structure as shown in Figure 2.1(c) may also result from polymorphic phase transitions induced in the test specimen by the incident wave. The phase transition mechanism has been invoked to explain double waves observed in iron,[2] quartz,[6, 8] and rocks.[7, 9, 10] Phase transitions induced in solids by shock waves seem to occur generally at stresses in excess of 100 kilobars. However, Gregson and Grine[7] suggest that in carbonate rocks phase transitions may occur at stresses as low as 30 kilobars.

Figure 2.1(d) illustrates a medium with a stress-strain curve having a region of anomalous compressibility. Over this range of stresses a steep-fronted wave cannot be propagated and becomes elongated as it travels through the specimen. Plane wave experiments[6] have shown that fused silica has a stress-strain curve similar to that of Figure 2.1(d).

If a medium is characterized by viscous or dissipative effects the rise time of a wave front such as shown in Figure 2.1(a) will not be steep but will appear more like that illustrated in Figure 2.2(a). That viscous effects may be significant has been demonstrated by noticeable variation in rise times observed in plane wave experiments with metals.[4, 11]

If relaxation phenomena occur in conjunction with yielding, wave profiles such as shown in Figure 2.1(b) may appear more like those of Figure 2.2(b). Very definite relaxation effects have been witnessed in iron,[4, 11] steels,[4] and quartz.[5, 6]

It is apparent that a realistic model describing nonfluid-nonelastic behavior of geologic solids may be quite complex since a natural material may, for example, exhibit several of the phenomena illustrated in Figures 2.1 and 2.2. Mechanisms of these various phenomena are largely unknown, even for metals. For comprehensive discussions of wave instability, viscosity, anomalous compression, relaxation, and yielding, the reader is referred to the literature, particularly two excellent review articles by Duvall[12, 13] and the references contained therein.

The extent to which geologic solids demonstrate nonfluid-nonelastic effects such as considered above has not been sufficiently investigated. The purpose of the work described here has been to initiate experiments by which these various effects may be observed and to perform a survey of a few rock

materials with large amplitude (1 to 100 kilobars) stress waves of high strain rates (10^3 to 10^6 sec^{-1}) under conditions similar to those created by buried explosions. These experiments were designed to yield sufficient data to at least characterize the responses of various rock materials and to provide guiding information which might assist in formulations of reasonable models. More specifically, objectives were to investigate in rock materials of current interest the magnitude of the dynamic yield point if one exists, the extent of viscous properties which might influence the rise times of propagated waves, the possibility of occurrence of anomalous compression in rocks, and whether or not rock materials demonstrate relaxation effects.

(a) Wave in Viscous Medium

(b) Wave in Medium With Nonzero Elastic Limit Demonstrating
Stress Relaxation
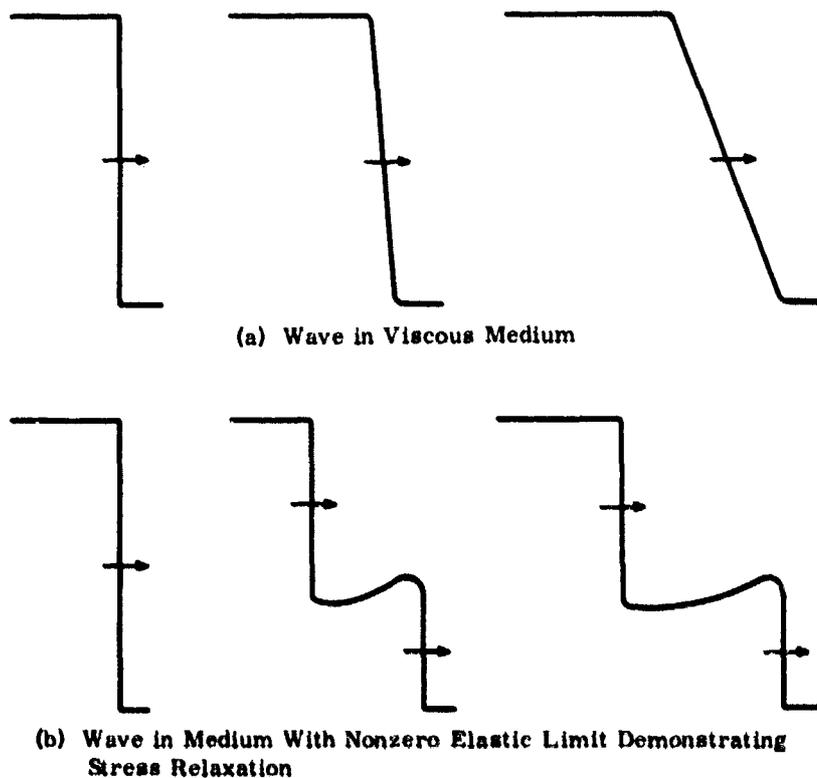
Figure 2.2 Wave Profiles for a Viscous Medium and Wave Profile With Stress
Relaxation After Yielding

In order to realize these aims it has been necessary to develop an instrument capable of measuring large amplitude stresses with high time resolution.

Description of Quartz Stress Gage

The new X-cut* quartz crystal technique perfected by Neilson[4, 14] et al. for examination of stresses in metals has been adopted for the observation of stresses in geologic solids. Since quartz has a higher dynamic elastic limit than that expected of most geologic materials, it is an ideal transducer for investigation of stress-time wave profiles. The dynamic elastic limit of X-cut quartz has been reported[5, 6] as about 50 kilobars. X-cut quartz has also been shown[15] to have a linear piezoelectric response to at least 25 kilobars.

Quartz transducers used to obtain stress-time profiles in solids have been found to compare favorably with other techniques such as the optical, [5, 6] capacitor, [11, 16] slanted resistance wire, [17] and pin[2, 3] methods, all of which measure free surface velocities rather than stress directly. The great advantages of quartz transducers are their ability to measure stresses directly, their high time resolution, and the relatively little effort required for their use.

Illustrated schematically in Figure 2.3 are two experimental arrangements for observing stress-time profiles in rock specimens. An explosively generated plane shock wave is transmitted into the specimen and then into the positively oriented‡ X-cut quartz crystal.

(a) with aluminum foil electrode

(b) with stress transmitting quartz crystal and evaporated gold electrode
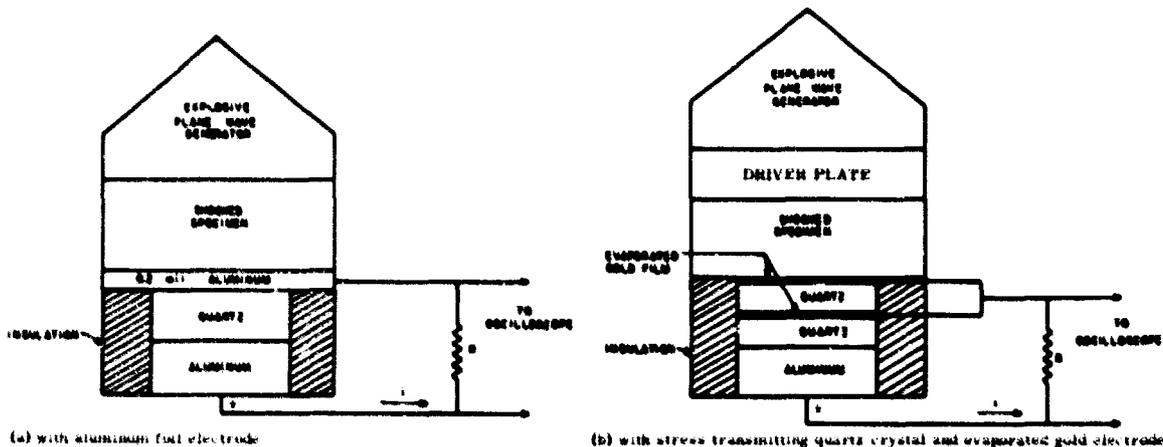
Figure 2.3 Schematic of Wave Profile Experiments

---

* Crystals oriented so that the stress wave is made to propagate along the crystallographic X-direction.

‡ The crystal is positively oriented when a compressive stress produces on the face farthest from the specimen a voltage which is positive with respect to that on the other face.

For small values of the resistor, R, the circuit current, i, is given[4,14] by

$$i = -\frac{AdC_Q}{w}\int_{x_F}^{x_B}\frac{\partial\sigma_Q(x,t)}{\partial x}dx = \frac{AdC_Q}{w}\left[\sigma_Q(x_F,t) - \sigma_Q(x_B,t)\right] ,$$ (2.1)

where A is the area and $w = (x_B - x_F)$, the thickness of the quartz crystal. The sonic velocity in quartz is C_Q; $d = e_{11}/c_{11}$ is the one-dimensional strain piezoelectric coefficient; $\sigma_Q(x_F,t)$ is the time variation of the stress wave in the crystal at the front surface, x_F, next to the shocked specimen; and $\sigma_Q(x_B,t)$ is the time variation of the wave leaving the back face, x_B. Note that for $t < w/C_Q$, before the stress wave front reaches the back surface, $\sigma_Q(x_B,t) = 0$, so that time variations in current give a direct measure of the pressure-time profile in quartz at the quartz-specimen interface. For times $t \geq w/C_Q$ the current is proportional to the stress difference across the crystal.

To determine the amplitude of the stress history in the shocked specimen from the quartz stress history at the interface, the degree of mismatch at the interface must be examined.

Consider the one-dimensional wave system at a time just after transmission of the wave into quartz.

Interface
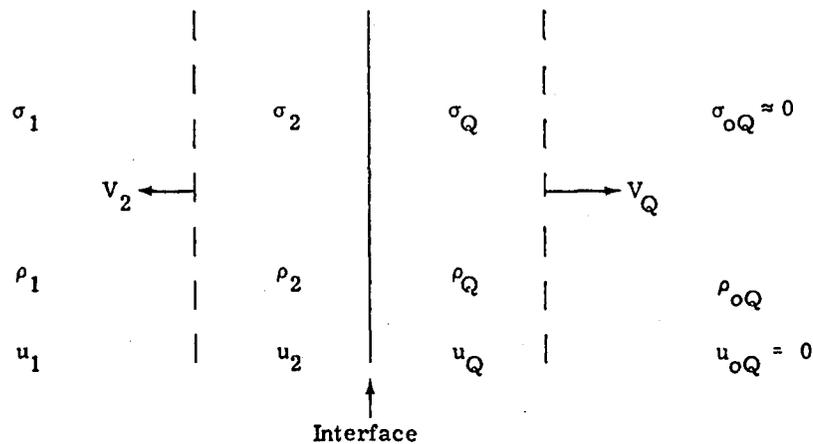
By conservation of momentum across the transmitted wave in quartz, we have

$$\sigma_Q = \rho_{oQ}V_Q u_Q = Z_Q u_Q ,$$ (2.2)

where σ_Q and u_Q are stress and particle velocity, respectively, behind the transmitted wave, ρ_{oQ} is the quartz density ahead of the wave, V_Q is the wave velocity in quartz, and Z_Q is the quartz impedance. Similarly, across the incident wave in the sample we had before the wave reached the interface

$$\sigma_1 = \rho_{o1}V_1 u_1 = Z_1 u_1 .$$ (2.3)

62

Across the reflected wave, momentum conservation gives

$$\sigma_2 - \sigma_1 = \rho_1 (V_2 + u_1)(u_1 - u_2) = Z_{1r}(u_1 - u_2) \quad , \tag{2.4}$$

where Z_{1r} is the reflected wave impedance of the sample relative to the flow ahead of the wave.

Dividing Equation 2.4 by Equation 2.3 and making use of the interface boundary conditions, $u_2 = u_Q$, $\sigma_2 = \sigma_Q$ results in

$$\frac{\sigma_Q}{\sigma_1} - 1 = \frac{Z_{1r}}{Z_1}\left(1 - \frac{u_2}{u_1}\right) \quad . \tag{2.5}$$

Since $\dfrac{u_2}{u_1} = \dfrac{u_Q}{u_1} = \dfrac{\sigma_Q}{\sigma_1}\dfrac{Z_1}{Z_Q}$, Equation 2.5 reduces to

$$\frac{\sigma_Q}{\sigma_1} = \left(\frac{1 + \dfrac{Z_{1r}}{Z_1}}{1 + \dfrac{Z_{1r}}{Z_Q}}\right) \quad .$$

Thus the stress $\sigma_1(t)$ behind the incident wave in the specimen is given in terms of the quartz interface stress, $\sigma_Q(t)$, and an impedance factor as

$$\sigma_1(t) = \left(\frac{1 + \dfrac{Z_{1r}}{Z_Q}}{1 + \dfrac{Z_{1r}}{Z_1}}\right)\sigma_Q(t) = Z\sigma_Q(t) \quad , \tag{2.6}$$

provided the transmitted wave in quartz has not reached the back face, x_B .

Having limited ourselves to stresses in quartz less than the elastic limit, the crystal impedance is simply $Z_Q = \rho_{oQ}C_Q$, where C_Q is the appropriate elastic wave velocity.

To completely determine the impedance factor of Equation 2.6, it is necessary to make the approximation that $Z_{1r} = Z_1 = \rho_{o1}C_1$, where C_1 is the elastic wave velocity in the specimen. The close agreement of stress time profiles obtained by quartz transducers with those obtained by other means mentioned above indicates that the impedance approximation is sufficiently accurate.

The use of quartz crystals for stress transducers functioning as described and according to Equation 2.1 is novel and different from the usual application of quartz crystals to measure stresses. In the common application, dimensions of the crystal transducer are small compared to a stress wavelength; the wave transit time in quartz is much less than the time variations in the stress wave, and the

total charge released by the crystal is proportional to the average stress imposed on it. In the Neilson application, wave transit time in quartz is much greater than time variations in the applied stress, waves of length less than the transducer dimensions may be measured, and the specimen-quartz-interface stress is proportional to the quartz current output.

In all our experiments X-cut crystals of synthetic alpha quartz* were used. The crystals were positively oriented‡ and generally were 1/2 inch in diameter and 1/8 inch thick. Crystals of this size were calibrated by R. A. Graham of Sandia Corporation with step-function type wave profiles at two pressures, 14.5 and 23.7 kilobars, resulting from high velocity projectile impacts. At these pressures the piezoelectric constant, d (average value = 2.05×10^{-8} coulombs/cm^2-kilobars), of Equation 2.1 was found to vary less than 5 percent for the initial step-function rise of the input wave. At a time when the wave has progressed halfway through the crystal the value of d has increased by about 10 percent. When the wave has reached the back surface of the quartz crystal the value of d is on the average 40 percent higher than it was initially, but at this time the stress-profile measurement is completed. That d is not strictly constant is a consequence of both mechanical and electrical edge effects in the crystal. In our survey of stress profiles from rock materials we have neglected the variation of d with distance of wave travel into the crystal and have used a constant value, $d = 2 \times 10^{-8}$ coulombs/cm^2-kilobar.

The primary purpose for using the configuration of Figure 2.3(b) was to increase the separation between the elastic precursor and the main shock wave entering the transducer crystal from the shocked rock specimen. For some of the rock materials studied it was found that the elastic precursor and main shock wave had velocities which were not greatly different. As a result the main shock wave entered the transducer crystal immediately after entry of the precursor and made examination of the precursor amplitude and profile difficult if not impossible.

The time-distance diagram of Figure 2.4 illustrates the difficulty encountered. For a given driving pressure at the rock-explosive interface, two waves are generated in the rock specimen, the elastic precursor wave of nearly constant velocity, C_S, and a shock wave of velocity V_S, whose value depends on the driving pressure. At the rock-quartz interface, the elastic precursor first enters the transducer at time t_1 and, after adjusting its amplitude according to the degree of impedance mismatch (Equation 2.6)

---

*Obtained from the Valpey Crystal Corp., 1244 Highland Street, Holliston, Mass.
‡ Negatively oriented crystals may also be used but only over a limited range of stresses.[18]

between rock and quartz, proceeds through quartz with the elastic velocity of quartz, C_Q, emerging at time t_3. However, before time t_3, the rock shock wave enters quartz at time t_2, transmitting a shock wave into the transducer.
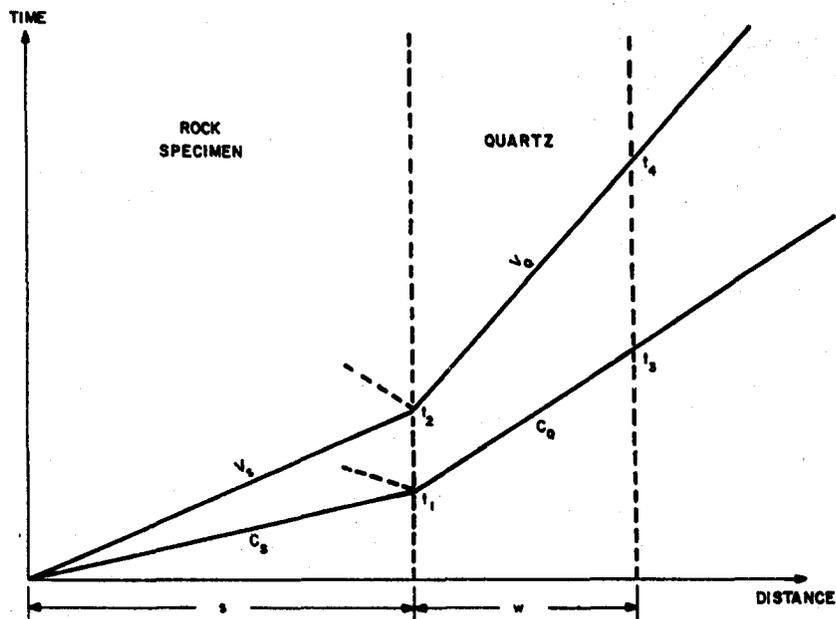
Figure 2.4 Time-Distance Diagram of Double-Wave System in Rock and Quartz Transducer

If the transmitted wave of velocity V_Q has a sufficiently large amplitude, impurity atoms of the quartz lattice in the region behind this wave are ionized, as suggested by Neilson[14] et al. As a result of ionization the electric field breaks down and conduction of electrons occurs behind the shock wave. Thus, after time t_2, the quartz no longer operates according to Equation 2.1 but by other means.[19]

In order to obtain information on the elastic precursor, we must try to satisfy $(t_2 - t_1) \geq (t_3 - t_1)$, which gives us a condition on the ratio of specimen-to-transducer thicknesses, $S/w \geq C_S V_S / C_Q (C_S - V_S)$. Since C_Q is fixed and the quartz thickness, w, cannot be greatly varied, specimen thickness, S, is governed by the magnitudes of precursor velocity, C_S, and shock velocity, V_S, in the specimen. Another condition of the thickness, S, is that the thickness-to-diameter ratio of the specimen be sufficiently small so that a true plane wave is maintained in the specimen as it progresses into the quartz transducer.

At some shock pressure (overdriving pressure) in the specimen, which is determined by the shape of the specimen Hugoniot, the elastic-plastic two-wave structure is no longer generated, the elastic wave is said to be overdriven by the larger amplitude shock or plastic wave, and at this pressure V_S is

65

equal to C_S. At shock pressures somewhat below this level, $C_S > V_S$ but the difference $(C_S - V_S)$ is small and the condition on S/w cannot be met. In the range of pressure from the Hugoniot elastic limit pressure to the overdriving pressure, Hugoniots of rock materials under test are either not well defined or not known at all. As a result, it is not possible, prior to making a wave profile measurement, to accurately estimate magnitudes of V_S which may be achieved by different driving explosives so that the condition on S/w can be realized.

By making the quartz crystal shown in Figure 2.4 a stress transmitter rather than the transducer and placing another quartz crystal as transducer behind it, the difficulty of an early entry of the shock or plastic wave is alleviated. In this configuration, the first and second wave arrivals are separated in time by an amount $(t_p - t_e)$ which is greater than the separation time $(t_2 - t_1)$ when no stress transmitter is used.

In Figure 2.5 are shown oscillograms of the elastic precursor in Armco iron, which was used to test the two transducer assemblies of Figure 2.3. The amplitude of the elastic wave just after the initial rise is about 6 kilobars. Sweep speed for all traces in Figure 2.7 was $0.2 \mu sec/cm$, except for the top trace in (a), where it was $0.1 \mu sec/cm$. All the quartz crystals used to obtain the records shown had diameters of 1/2 inch and thicknesses of 1/8 inch. TNT was the driving explosive in each experiment.

The record traces of Figure 2.5(a) were obtained from quartz crystals in direct contact with a 1/2-inch-thick piece of Armco iron, which served as one electrode for the transducer. The symbol A-Q is used to note this type of assembly. In this experiment the plastic wave from Armco entered the front surface of the quartz transducer after entry of the precursor but before the precursor arrived at the transducer back surface. Thus one sees the 6-kilobar precursor followed in time by the large-amplitude (> 100-kilobar) plastic wave which takes the trace off scale. These records are similar to those observed by others[4, 11, 14] in Armco iron.

Figure 2.5(b) compares the signals from one experiment with two quartz transducers on a 1-inch-thick piece of Armco. The top trace of (b) is from a transducer in direct contact with Armco (A-Q), and the lower trace is from a transducer with a 0.2-mil aluminum foil placed between the Armco and quartz (A-Al-Q), as shown in Figure 2.3(a). The traces are essentially identical, indicating that the 0.2-mil aluminum foil is not a serious perturbation to the wave from Armco. In this experiment the plastic wave from Armco does not arrive at the front surface of the quartz until after the precursor transmitted into quartz has traversed the thickness of quartz. The time at which the precursor wave in quartz reaches the quartz back surface is noted by an abrupt swing of the trace downward, owing to the

ELECTRODE ASSEMBLY		RELATIVE GAIN	SWEEP $\mu sec/cm$	ARMCO THICKNESS (in.)

A-Q   1   0.1

       1/2

A-Q   1/2   0.2

(a)

A-Q   1   0.2

       1

A-Al-Q   1   0.2

(b)

A-Q   1   0.2

       1

A-Q-Q   1   0.2

(c)

Figure 2.5 Quartz Transducer Oscillograms from Armco Iron

With Three Types of Electrode Assemblies:
(a) quartz directly on Armco iron,
(b) quartz with aluminum foil on Armco,
(c) quartz on quartz on Armco with gold electrode.

term $\sigma_Q(x_B, t)$ of Equation 2.1. The time difference between the start of the trace and the time at which it turns downward is, within experimental error, the calculated elastic wave transit time in quartz.

Records of Figure 2.5(c) are from an experiment identical to that described for Figure 2.5(b) except that the lower trace of (c) is from a transducer in contact with a quartz blank (A-Q-Q), as shown in Figure 2.3(b). This transducer arrangement is also shown in Figures 2.6 and 2.7. The traces of oscillograms (b) and (c) indicate that the Armco elastic precursor is very well reproduced by quartz transducers in either assembly configuration of Figure 2.3. From these experiments with Armco iron it was concluded that the quartz transducer technique would be adequate to examine stress-time profiles in rock materials.
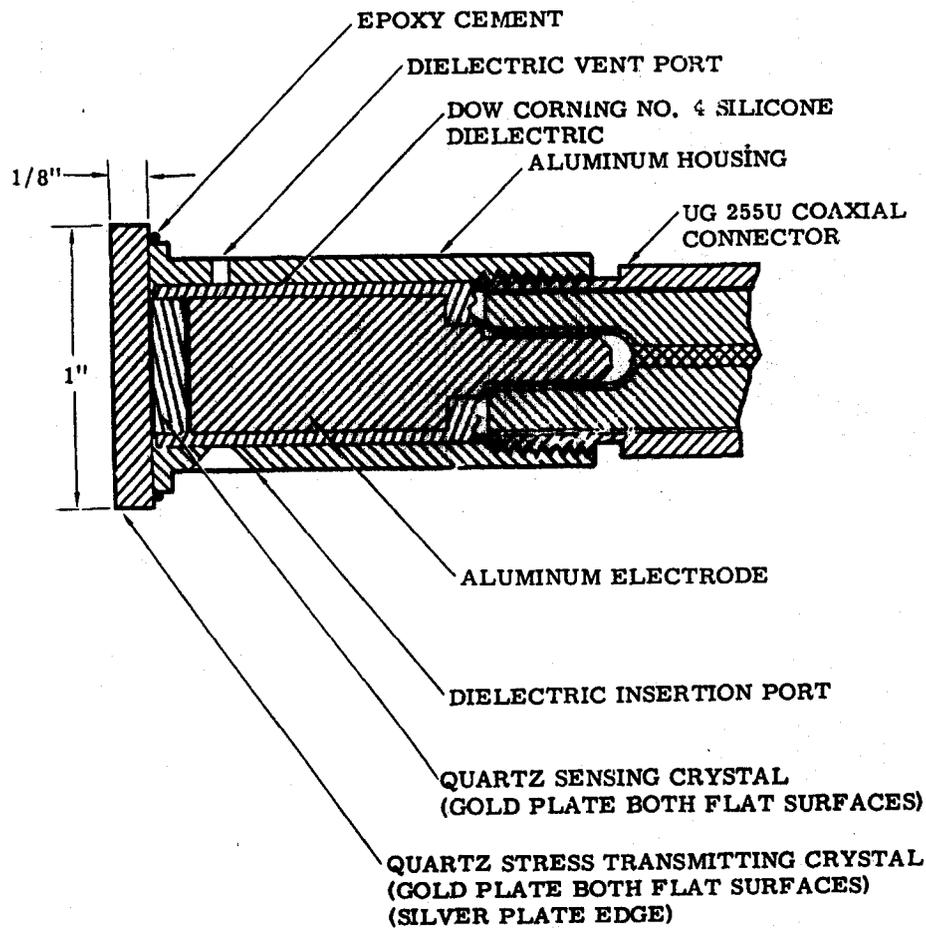
Figure 2.6 Assembly Drawing of Quartz Crystal Transducer

Figure 2.7 Photo of Quartz Stress Transducer

Experimental Results

Rock samples examined with the quartz crystal transducer were obtained from drill cores, cut to various thicknesses and ground smooth and flat. The diameter-to-thickness ratio of samples was always in excess of 2.5. Aluminum (2024) or steel (4340) was the driver plate placed between sample and explosive as shown in Figure 2.3(b). Explosives used were TNT, Baritol, and Nitroguanidine. The quartz transducer employed for all experiments described here was that of Figures 2.3(b), 2.6, or 2.7. Current output of transducers was measured on Tektronix 555 and 581 oscilloscopes as the voltage drop across a 50-ohm resistor. Timing markers and voltage calibration signals were also recorded along with signal traces. In many, but not all, experiments velocity of the first wave was measured by recording wave transit time through the specimen.

Granite

Granite rock samples utilized in experiments reported here were obtained from a location near Fallon, Nevada and are referred to as Shoal granite. Typical wave profiles recorded by the quartz transducer on two thicknesses of Shoal granite are shown in Figure 2.8. Rise times of waves to the first peak are noted by arrows labeled t_r. Time of arrival of the second wave is noted by arrows labeled $t_s = (t_4 - t_3)$. The scale to the right of the figure indicates the magnitude of stresses in the granite wave and is derived from the voltage scale to the left using $d = 2 \times 10^{-8}$ coulombs/cm^2-kilobar in Equation 2.1 and $Z = 1$ in Equation 2.6. Between the times t_r and t_s there appears to be a relaxation of peak stress in the first wave. The stress profiles of Figure 2.8 prior to the time t_s are believed to be elastic precursor waves in granite.
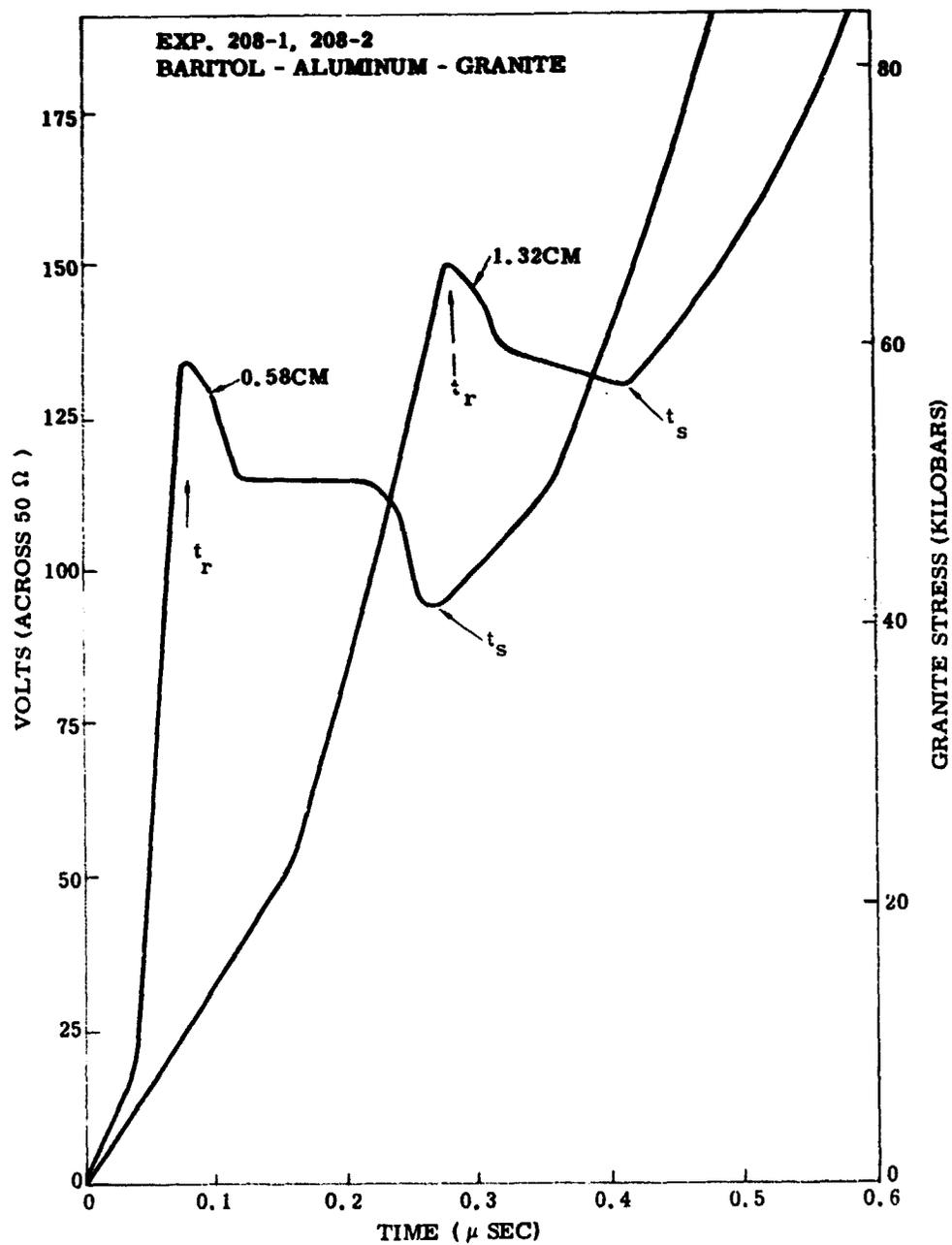
Figure 2.8 Stress Wave Profiles Observed in Two Thicknesses of Granite

Although the dynamic yield stress of granite is expected to be quite high (Grine[20] has reported 36 kilobars for another type of granite), it cannot be concluded from the records of Figure 2.8 that Shoal granite has an elastic limit of 60 kilobars. There are two reasons for this. First, the dynamic piezoelectric coefficient, d, for quartz is not well known at stress levels near or above 50 kilobars, and second, at about 50 kilobars quartz itself begins to yield[5, 6] and is no longer an adequate transducer.

Calibration of quartz crystals with diameter-to-thickness ratio of 5 by projectile impact experiments has shown[21] that d increases fairly linearly with increasing stress, being 2.05×10^{-8} and 2.48×10^{-8} coulombs/cm^2-kilobar at 25 and 45 kilobars, respectively.

From this information we may surmise that the peak amplitudes of waves in Figure 2.8 are somewhat more than 40 kilobars and probably less than 50 kilobars. Because the precursor amplitude in granite is higher than was expected, the wave profiles observed were obtained with the quartz transducer operating in a region where its piezoelectric properties are not well known. Consequently, the wave profiles obtained for granite (except for experiment number 188) must be regarded as being of a qualitative nature.

Table 2.1 is a list of experiments performed with various thicknesses of Shoal granite showing the explosives used and the rise times and second wave arrivals observed.

TABLE 2.1

Shoal Granite Experiments
(1 cm thick Aluminum Driver)

Experiment No.	Explosive type	Sample thickness S_G(cm)	Rise time t_r (μsec)	Second wave arrival time t_s (μsec)
215-1*	TNT	0.340	~ 0.1**	~ 0.24
215-2*	TNT	0.986	0.14	0.40
189	TNT	2.480	0.34	0.47
197	TNT	4.032	0.71	0.80
216	Baritol	0.340	0.06	0.22
208-1‡	Baritol	0.582	0.08	0.27
204	Baritol	0.824	0.16	0.28
203	Baritol	1.062	0.16	0.38
208-2‡	Baritol	1.320	0.28	0.42
192	Baritol	2.415	~ 0.55	--
188	Nitroguanidine	2.615	~ 0.6	--

* Both granite samples on one TNT experiment
**Doubtful result
‡ Both granite samples on one Baritol experiment

In Figure 2.9 are plotted granite wave profiles obtained from experiments with TNT. Since from Table 2.1 rise time, t_r, appears to increase linearly with increasing sample thickness we have plotted as abscissa the dimensionless time, $\tau = tC_G/S_G$, using the average value of first wave velocity in granite, $C_G = 0.57 \pm 0.03$ cm/μsec, obtained from independent measurements. Small arrows in the figure indicate the times, t_s, considered to be second wave arrivals. The pressure scale on the right of

the figure is provided to show only the magnitude of stresses involved and, just as in Figure 2.8, over-estimates stresses particularly at higher stresses and later times. From Figure 2.9 it is seen that the reduced rise time is roughly constant for all thicknesses of granite except for the thinnest sample, S_G = 0.34 cm. The wave profile for this sample seems to be anomalous. The reason for the anomaly is unknown; it may be that the wave in the sample was not plane or was tilted or possibly that the sample was not uniform and homogeneous. That the reduced rise time is nearly constant for all the other sample thicknesses suggests that granite exhibits dissipative or viscous effects.

Granite wave profiles produced by Baritol explosives are shown plotted in Figure 2.10. Here again the reduced rise time for all thicknesses of granite is roughly constant. Note that the reduced rise time for the sample of 0.34 cm thickness is about the same as for the other thicker samples and does not appear to be anomalous as was the case for the 0.34 cm thick sample driven by TNT.
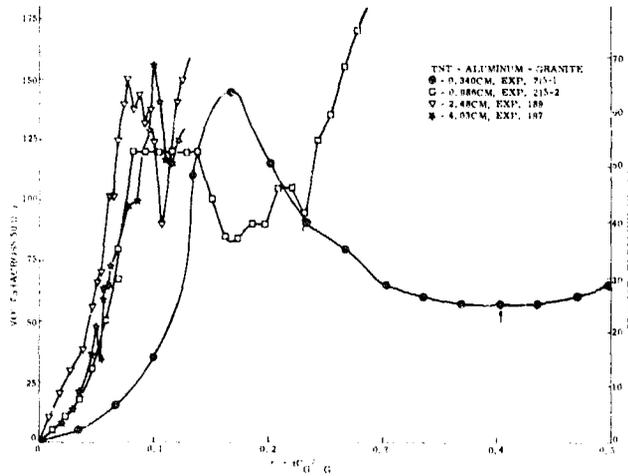
Figure 2.9 Granite Stress Wave Profiles as a Function of Reduced Time for TNT Experiments
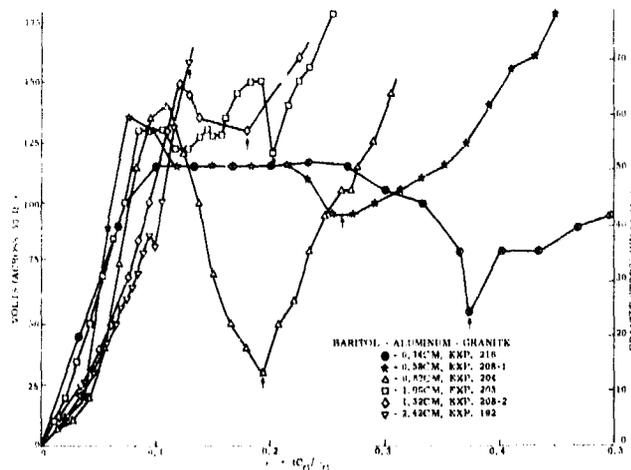
Figure 2.10 Granite Stress Wave Profiles as a Function of Reduced Time for Baritol Experiments

The influence of driving pressure on the rise time of waves in granite is seen in Figure 2.11 where profiles initiated by TNT, Baritol, and Nitroguanidine in samples about 2.5 cm thick are shown. Driving pressures produced in granite by TNT, Baritol and Nitroguanidine are about 200, 130 and 40 kilobars, respectively. Evidently the rise time decreases as driving pressure increases. The wave profile from the Nitroguanidine experiment is particularly interesting. Peak amplitude of the wave is about 35 kilobars, and this value may be considered as having some reliability since quartz transducers function properly at these stress levels. There is no evidence of a second wave arrival before one transit time of the wave in quartz, from which we may conclude that the Hugoniot elastic limit in Shoal granite is in excess of 35 kilobars. If the elastic limit were less than about 35 kilobars a double wave structure would certainly have been observed. The Nitroguanidine plane wave generator used in this experiment was fabricated by W. Benedick of Sandia Corporation. Density of the explosive was 0.41 gm/cm^3. Shock pressures generated in aluminum by Nitroguanidine with this density are found[22] to be between 40 and 50 kilobars.
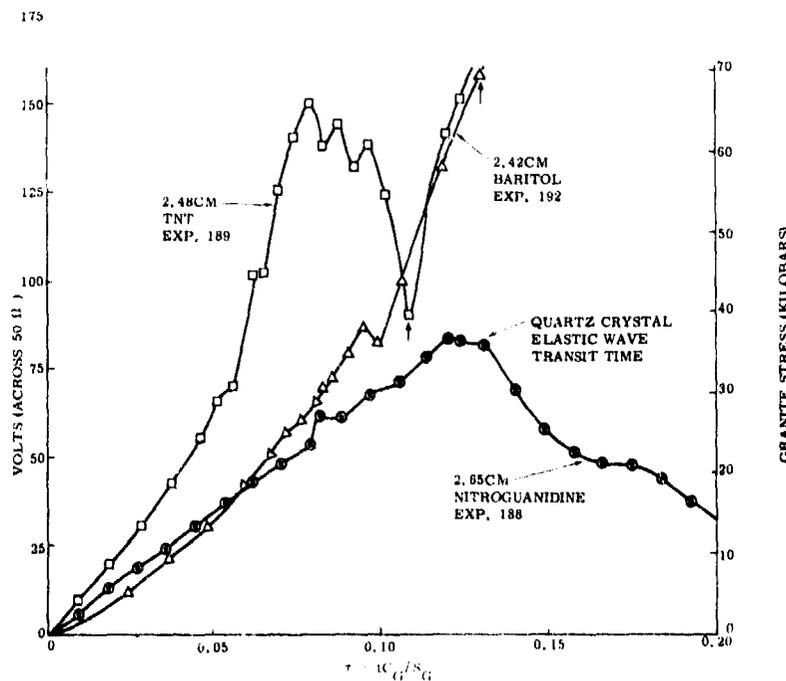
Figure 2.11   Effect of Driving Pressure on Rise Time of Waves in Granite

Because the first wave stresses in granite were so high the quartz crystal transducers found themselves operating at stress levels where their piezoelectric properties are not known and at stress levels near which quartz itself yields. Consequently we do not have great confidence in the times denoted for second wave arrivals in Figures 2.9 and 2.10. There are, however, other indications that a double

wave structure is exhibited by Shoal granite. First wave velocities appear to be nearly constant, C_G = 0.57 ± 0.03 cm/μsec, regardless of sample thickness and driving explosive. If a single shock wave were stable in granite the more energetic explosives would produce waves of higher velocity; this was not observed. Also, if the first wave velocity is constant the second or shock wave velocity, V_G, in granite may be calculated from

$$V_G = \left(\frac{t_s}{S_G} + \frac{1}{C_G}\right)^{-1} \tag{2.7}$$

and compared with other Hugoniot data for Shoal granite. From the values of t_s and S_G listed in Table 2.1 one obtains the average values of second wave velocity, V_G = 0.500 cm/μsec, from TNT experiments and V_G = 0.493 cm/μsec from Baritol experiments. Knowledge of the shock pressure generated in the aluminum plate by TNT and Baritol enables one to determine the pressure and particle velocity associated with the second wave in granite. By the standard impedance-mismatch technique (e. g. , see Figure 1 of Reference 6) one obtains the following Hugoniot data for Shoal granite:

P_2 = 163 Kbar, u_2 = 0.118 cm/μsec, V_G = 0.500 from TNT

P_2 = 133 Kbar, u_2 = 0.096 cm/μsec, V_G = 0.493 from Baritol.

To obtain the above figures it was necessary to estimate the Hugoniot elastic limit, P_1, of Shoal granite. This was taken as 50 kilobars. Other assumed values of P_1 between 40 and 60 kilobars change the values of P_2 listed above by less than 10 percent. The two Hugoniot data obtained from the quartz crystal measurements are shown along with other Hugoniot data[23] in Figure 2.12. That the quartz crystal data are consistent with Hugoniot data obtained by other means suggests to us that a double wave structure is actually being observed by the quartz transducers.

Results of wave profile experiments with quartz crystal transducers strongly point to the existence of a two-wave structure in Shoal granite at driving pressures below about 300 kilobars. The experimental records do not demonstrate this positively, however. If a double wave structure exists, as appears to be the case, the granite precursor amplitude or dynamic yield strength is felt to be in excess of 35 kilobars and probably between 40 and 50 kilobars.

In the wave profiles measured there appears to be a relaxation of stress after the first peak or yield stress in granite is achieved. As noted before, this relaxation may be instead some idiosyncrasy of the quartz transducer. Further calibration experiments on quartz transducers are required with 50-kilobar waves and with various wave profiles or strain rates before the relaxation can be definitely assigned to the granite waves.
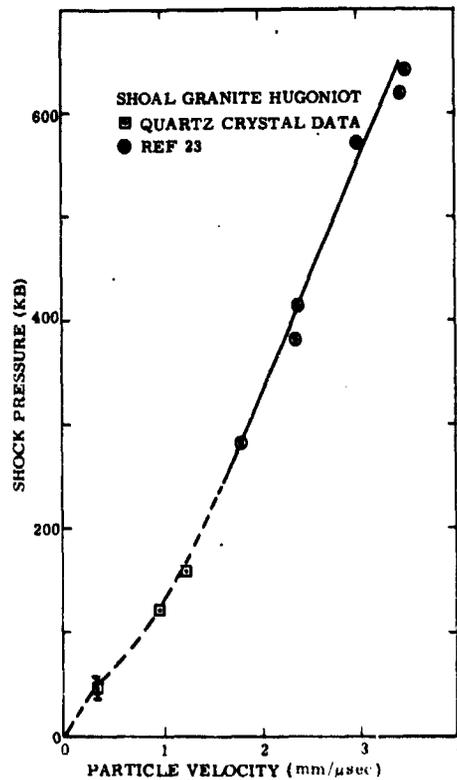
Figure 2.12 Quartz Crystal Data Plotted With Hugoniot Data for Granite

A more definite result of the granite experiments is that the rise time of the first (and possibly only) wave increases with increasing distance of wave travel in granite. This observation is considered as evidence for viscous behavior of granite.

It must be emphasized that the interpretations given the records obtained from Shoal granite with quartz crystal transducers are largely qualitative and certainly not unique. Before more definitive information on granite may be obtained further experiments are required.

Salt

Samples of rock salt used in wave profiles experiments were obtained from a location near Winnfield, La., and are referred to as Cowboy salt. All samples were highly nonuniform in the sense that they were permeated by numerous cleavage and shatter cracks. Density of Cowboy salt was 2.15 gm/cm^3 and the average first wave velocity measured was 0.40 ± 0.02 cm/μsec, slightly less than the reported[24] seismic velocity, 0.438 cm/μsec.

The crystal transducer of Figure 2.6 was used in all experiments. Because a very low precursor amplitude in salt was expected, of the order of 1 or 2 kilobars,[25] explosives in direct contact with salt

or explosives with a driver plate such as aluminum could not be used as it was feared that the high driving pressures generated would overdrive the elastic precursor. The driver plate chosen for the salt experiments was 4340 steel from which waves of amplitude 16 to 25 kilobars are obtained,[4] depending on the Rockwell C hardness of the steel. These waves in 4340 are actually the elastic precursors of steel. TNT explosive was used to initiate the waves in steel.

In Figures 2.13 and 2.14 are shown the results of wave profile measurements in salt. For each experiment a quartz transducer was placed on the back surface of the 4340 driver plate as well as on the salt sample. By this means the wave profile produced in steel by TNT and transmitted into salt was measured. The topmost profiles of Figures 2.13 and 2.14 are the waves entering the salt samples; lower profiles in the figures are those from salt.

Salt sample thicknesses for Figures 2.13(a) and 2.13(b) were 2.54 and 2.01 cm, respectively. In each of these experiments the 4340 driver plate was 7.62 cm thick. The quartz transducer used to obtain the profiles of Figure 2.13(a) was 1/4 inch in diameter by 1/8 inch thick, while that used to measure profiles of Figure 2.13(b) was 1/2 inch in diameter by 1/4 inch thick.

In Figures 2.14(a) and 2.14(b) the 4340 driver plate was 2.54 cm thick, and the salt sample thicknesses were 1.05 and 0.886 cm, respectively. Diameter and thickness dimensions of quartz transducers were 1/2 inch by 1/8 inch for both experiments of Figures 2.14(a) and 2.14(b).

Impedance factors, Z, of Equation 2.6 used to reduce records were 2.02 for steel to quartz and 0.784 for salt to quartz.

That the wave profiles measured in 4340 steel are not identical in Figures 2.13 and 2.14 is due to the fact that the steel driver plates did not all receive the same heat treatment, and consequently they are expected to yield different profiles.[4] The Rockwell C hardness of steel drivers in Figure 2.13 is not known. For the steel drivers of Figure 2.14 the hardness is estimated to be between 35 and 50.

It is difficult to make a comparison of the stress profiles from salt because of the different stress profiles transmitted into it and because of its different thicknesses. Nevertheless, it can be seen that under roughly similar conditions (see Figure 2.13) the salt profile amplitudes at a given time may differ by as much as a factor of two. Perhaps these differences in salt profiles are a result of the nonuniformities in samples. All of the salt stress profiles do, however, have the same general shape, a slowly rising wave form without prominent maxima or peaks. If Cowboy salt had a Hugoniot elastic limit at about 1 or 2 kilobars and a stress-strain curve similar to that of Figure 2.1(b), a double wave structure should have been observed from the driving pressure of 4340 steel. Since the wave profiles observed in
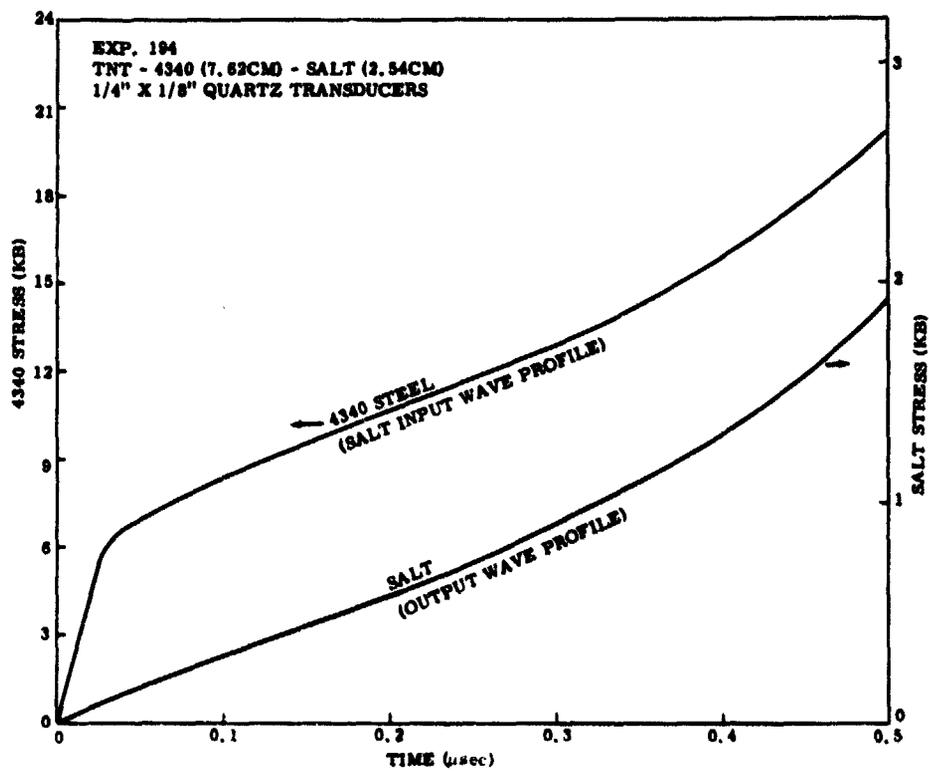
(a)
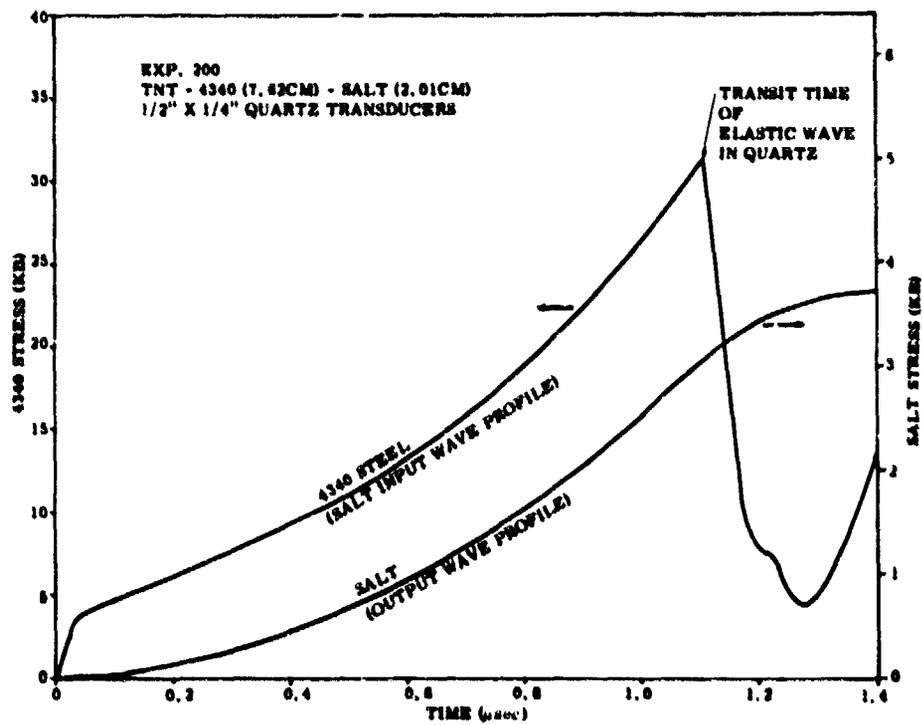
(b)

Figure 2.13 Stress Wave Profiles in Salt, 3-Inch 4340 Steel Driver
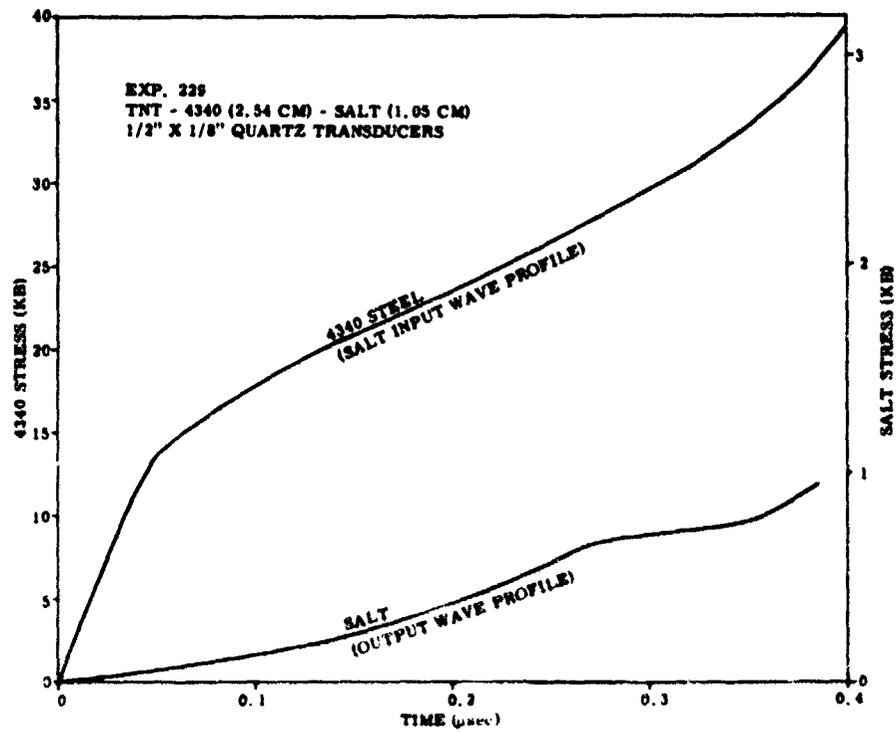
(a)
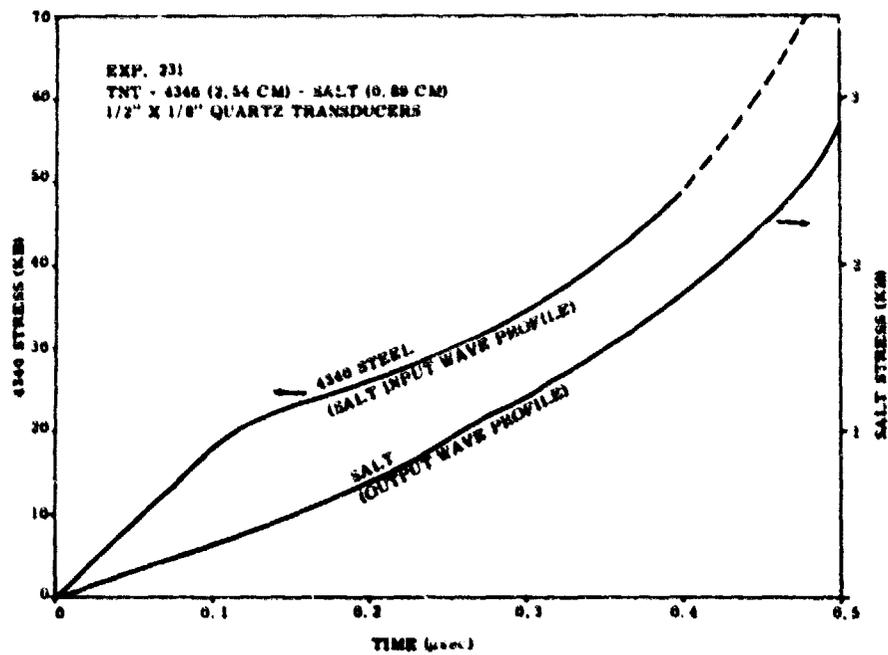
(b)

Figure 2.14   Stress Wave Profiles in Salt, 1-Inch 4340 Steel Driver

salt are more nearly similar to those of Figure 2.1(d) it is felt that the stress-strain relation of Cowboy salt has a region of anomalous compressibility for stresses in salt less than 20 kilobars.

Basalt

From Area 18 (Danny Boy site) of the Nevada test site a sample of basalt rock was obtained for wave profile experiments. A stress wave profile measured in basalt is shown in Figure 2.15. A plane wave explosive generator, Baritol explosive, a 1 cm thick aluminum driver plate, and the transducer assembly of Figure 2.6 were used to obtain the profile of Figure 2.15. Density of the basalt sample was 2.67 gm/cm^3 and measured first wave velocity was 0.524 cm/μsec.

EXP. 230
BARITOL - ALUMINUM (1CM) - BASALT (1.902CM)
1/2" X 1/8" QUARTZ TRANSDUCER
Z - 6.962

38KB

SECOND WAVE ARRIVAL.
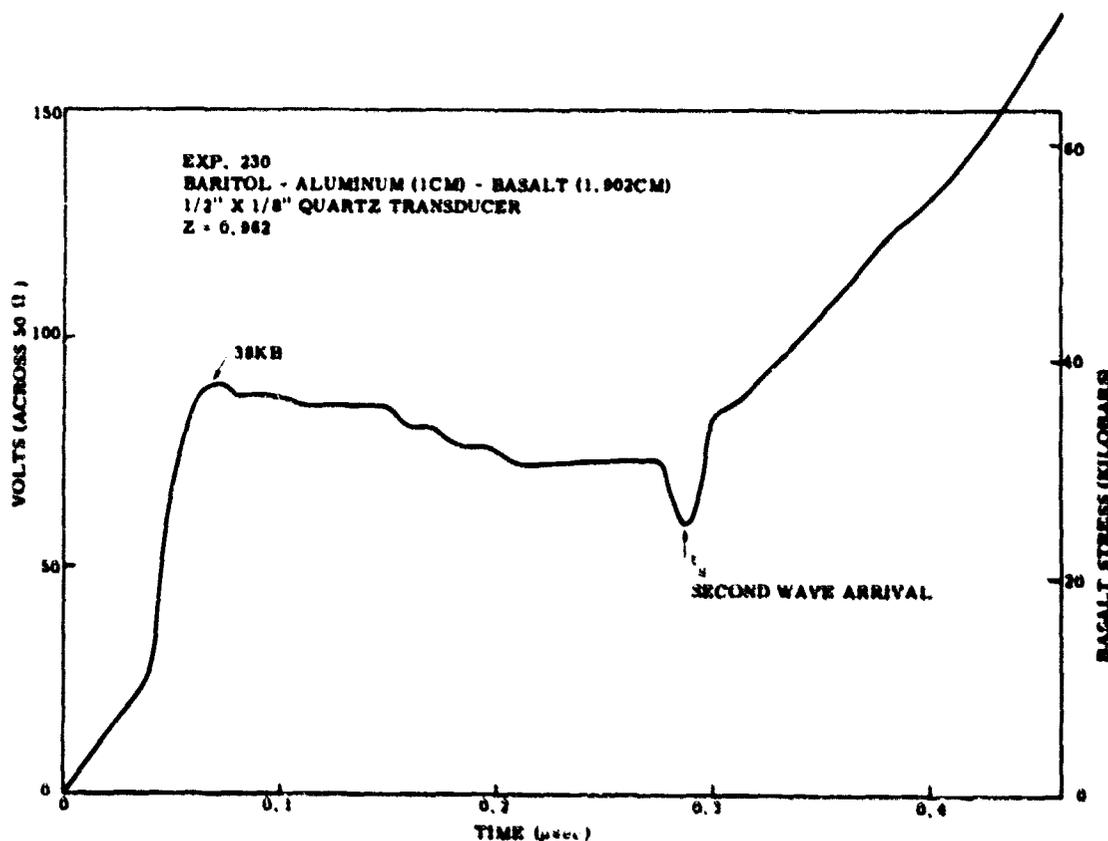
Figure 3.15 Stress Wave Profile in Basalt

The peak stress occurring at 0.07 μsec indicates a Hugoniot elastic limit of 38 kilobars for basalt. This precursor amplitude may be compared with the 50-kilobar Hugoniot elastic limit observed by Erkman[26] in a basalt of density 2.82 gm/cm.^{3} Between the time of peak stress and the time of second wave arrival a relaxation in stress of about 7 kilobars occurs.

The second wave arrival time is clearly noted. From Equation 2.7, we may estimate the second

wave velocity, as was done for granite, and calculate a point on the basalt Hugoniot. Shock velocity is

found to be 0.485 cm/μsec. Using 38 kilobars as the Hugoniot elastic limit and the appropriate aluminum

reflection Hugoniot, shock pressure and particle velocity associated with the second wave are 127 kilobars

and 0.102 cm/μsec. This datum is consistent with other Hugoniot data[23] for basalt.

Unlike the transducer used with granite, the quartz transducer which measured the basalt profile

of Figure 2.15 operated at stress levels below the dynamic yield stress of quartz where the piezoelectric

response of quartz is relatively well known. As a result, considerably more reliability may be attached

to the basalt profile than to the granite profile.

Conclusions

The quartz crystal technique developed by Neilson[14] for the measurement of stress wave profiles

in metals has been adapted for studies of stress waves in rock materials. This new technique is capable

of measuring stresses directly with high time resolution at stress levels below about 45 kilobars.

A cursory examination has been made of three rock materials to investigate the properties which

characterize nonfluid-nonelastic stress wave propagation. Results of experiments indicate that Shoal

granite exhibits a viscous nature whose effect is to lengthen the rise time of a step-function type stress

wave as it propagates in granite. Rise times of waves in granite appear to be influenced by the driving

pressure. The Hugoniot elastic limit of Shoal granite is in excess of 35 kilobars and probably is

between 40 and 50 kilobars.

Cowboy salt appears not to have a Hugoniot elastic limit during times over which observations were

made; rather the wave profiles observed in salt suggest that the stress-strain relation for salt is such

that compressions are anomalous at stresses below about 20 kilobars.

A wave profile measured in basalt established the Hugoniot elastic limit as nearly 40 kilobars and

also indicated that relaxation effects exist in basalt.

While these initial experiments have not provided reliable quantitative information on the rock

materials examined, they have pointed out some effects which will require consideration in the formula-

tion of models of nonfluid-nonelastic behavior of geologic solids. Before accurate calculations can be

made of nonfluid-nonelastic stress wave propagation from buried explosions, the results of laboratory

plane wave experiments must first be understood.

LIST OF REFERENCES

1. Rice, M. H., McQueen, R. G., and Walsh, J. M., "Compression of Solids by Strong Shock Waves," Solid State Physics, Vol. 6, pp. 1-63, Academic Press, New York, 1958.

2. Bancroft, D., Peterson, E. L., and Minshall, S., "Polymorphism of Iron at High Pressure," Jour. Appl. Phys., Vol. 27, No. 3, 291, 1956.

3. Minshall, S., "Properties of Elastic and Plastic Waves Determined by Pin Contactors and Crystals," Jour. Appl. Phys., Vol. 26, No. 4, 463, 1955.

4. Jones, O. E., Neilson, F. W., and Benedick, W. B., "Dynamic Yield Behavior of Explosively Loaded Metals Determined by a Quartz Transducer Technique," Jour. Appl. Phys., Vol. 33, No. 11, 3324, Nov. 1962.

5. Fowles, G. R., Shock Wave Compression of Quartz, Technical Report 003-61, Stanford Research Institute, Menlo Park, Calif., Oct. 1961.

6. Wackerle, J., "Shock Wave Compression of Quartz," Jour. Appl. Phys., Vol. 33, No. 3, March 1962.

7. Gregson, V. G., and Grine, D. R., Vela-Uniform Dynamic Properties of Rocks, Semiannual Technical Report No. 2, SRI, Project No. PGU-3630, Stanford Research Institute, Menlo Park, Calif., April 1962.

8. McQueen, R. G., Fritz, J. N., and Marsh, S. P., "On the Equation of State of Stishovite," Jour. Geophys. Res., Vol. 68, No. 8, 2319, April 1963.

9. Hughes, D. S., and McQueen, R. G., "Density of Basic Rocks at Very High Pressures," Trans. Am. Geophysical Union, Vol. 39, No. 5, 959, Oct. 1958.

10. Adadurov, G. A., et al., "A Study of the Volumetric Compressibility of Marble at High Pressure," Bull. Acad. Sci., USSR, Vol. 5, Geophysics, May 1961.

11. Taylor, J. W., and Rice, M. H., "Elastic-Plastic Properties of Iron," Jour. Appl. Phys., Vol. 34, No. 2, 364, Feb. 1963.

12. Duvall, G. E., "Some Properties and Applications of Shock Waves," Response of Metals to High Velocity Deformation, Metallurgical Society Conference, Vol. 9, pp. 165-203, Interscience Publishers, New York, 1960.

13. Duvall, G. E., "Concepts of Shock Wave Propagation," Bull. Seismological Soc. Am., Vol. 52, No. 4, pp. 869-893, Oct. 1962.

14. Neilson, F. W., Benedick, W. B., Brooks, W. P., and Graham, R. A., Electrical and Optical Effects of Shock Waves in Crystalline Quartz, SCR-416, Sandia Corp., Albuquerque, N. M., June 1961.

15. Graham, R. A., "Piezoelectric Behavior of Impacted Quartz," Jour. Appl. Phys., Vol. 32, No. 3, 1961.

16. Rice, M. H., "Capacitor Technique for Measuring the Velocity of a Plane Conducting Surface," Rev. Sci. Instr., Vol. 32, No. 4, 449, 1961.

17. Barker, L. M., Determination of Shock Wave and Particle Velocities from Slanted Resistor Data, SC-4611(RR), Sandia Corp., Albuquerque, New Mexico, May 1961.

18. Graham, R. A., Dielectric Anomaly in Crystalline Quartz, SCTM 299-61(51), Sandia Corp., Albuquerque, New Mexico, September 1961.

19. Neilson, F. W., and Benedick, W. B., The Piezoelectric Response of Quartz, Beyond its Hugoniot Elastic Limit, SCR-502, Sandia Corp., Albuquerque, New Mexico, April 1962.

20. Grine, D. R., Dynamic Strength of Rocks, 29th Shock and Vibration Symposium sponsored by Office of Naval Research, Oakland, California, Nov. 1960.

21. Graham, R. A., Sandia Corporation, Albuquerque, New Mexico, (private communication).

22. Benedick, W. B., Sandia Corporation, Albuquerque, New Mexico, (private communication).

23. Bass, R. C., Hawk, H. L., and Chabai, A. J., Hugoniot Data for Some Geologic Materials, SC-4903(RR), Sandia Corporation, Albuquerque, New Mexico, 1963.

LIST OF REFERENCES (Cont.)

24. Nicholls, H. R., Hooker, V., and Duvall, W. I., Dynamic Rock Mechanics Investigations, Project Cowboy, Report APRL 38-3.2, U. S. Bureau of Mines, College Park, Md., September 1960.

25. Lindsay, W. F., et al., Project Cowboy Close-In Pressure Measurements with Tourmaline Crystals on Tamped Detonations, UCRL-6184, Lawrence Radiation Laboratory, Univ. of Calif., Livermore, Calif., Nov. 1960.

26. Erkman, J. O., Hydrodynamic Theory and High Pressure Flow in Solids, Progress Report No. 21, SRI Project PGU-3712, Stanford Research Institute, Menlo Park, Calif., March 1963.

Section 3

LONG-PERIOD DISPLACEMENT GAGES

J. W. Wistor, J. A. Beyeler, and G. J. Hansen

Instrument development for observation of long-period earth displacement produced by underground explosions has been directed toward relative displacement devices (long-base strain gages), inertial displacement gages, and electronic single and double integrators.

Stretched-Wire Gages

The spring-loaded wire gages used by Sandia Corporation on Plumbbob Projects 1.5 and 26.4b are typical examples of state-of-the-art stretched-wire relative displacement gages. The gage system comprises a spring-loaded music wire stretched under continuous tension between a fixed anchor and a spring-loaded drum in the transducer unit. An auxiliary helical extension spring is used to preload the main music wire to ensure optimum frequency response from the system. The music wire is operated within a flexible metal tube, which permits free movement of the wire and effectively decouples it from the surrounding medium (Figure 3.1). This instrument had a usable displacement range of about ±20 inches and a response of 20 milliseconds per foot to a step displacement. A modified form of this gage was used at several locations on the Small Boy event at NTS.

The Small Boy instrumentation consisted of three deep drill holes which contained particle motion gages at various depths between the surface and 400 feet. The displacement gages used in these drill holes were constructed in the following manner:

A large canister at the bottom end of each instrument array housed the spring-loaded displacement pickoffs and the preload springs. The remote displacement zeroing and spring tensioning mechanisms were housed in satellite canisters at various locations in the uphole portion of the array. These satellite canisters, which also contained velocity gages and accelerometers, acted as the forward anchor points for the displacement gage arrays (see Figures 3.2, 3.3, 3.4, and 3.5). These gages could measure up to 70 inches of relative displacement and were operated over spans of from 100 feet to 375 feet.
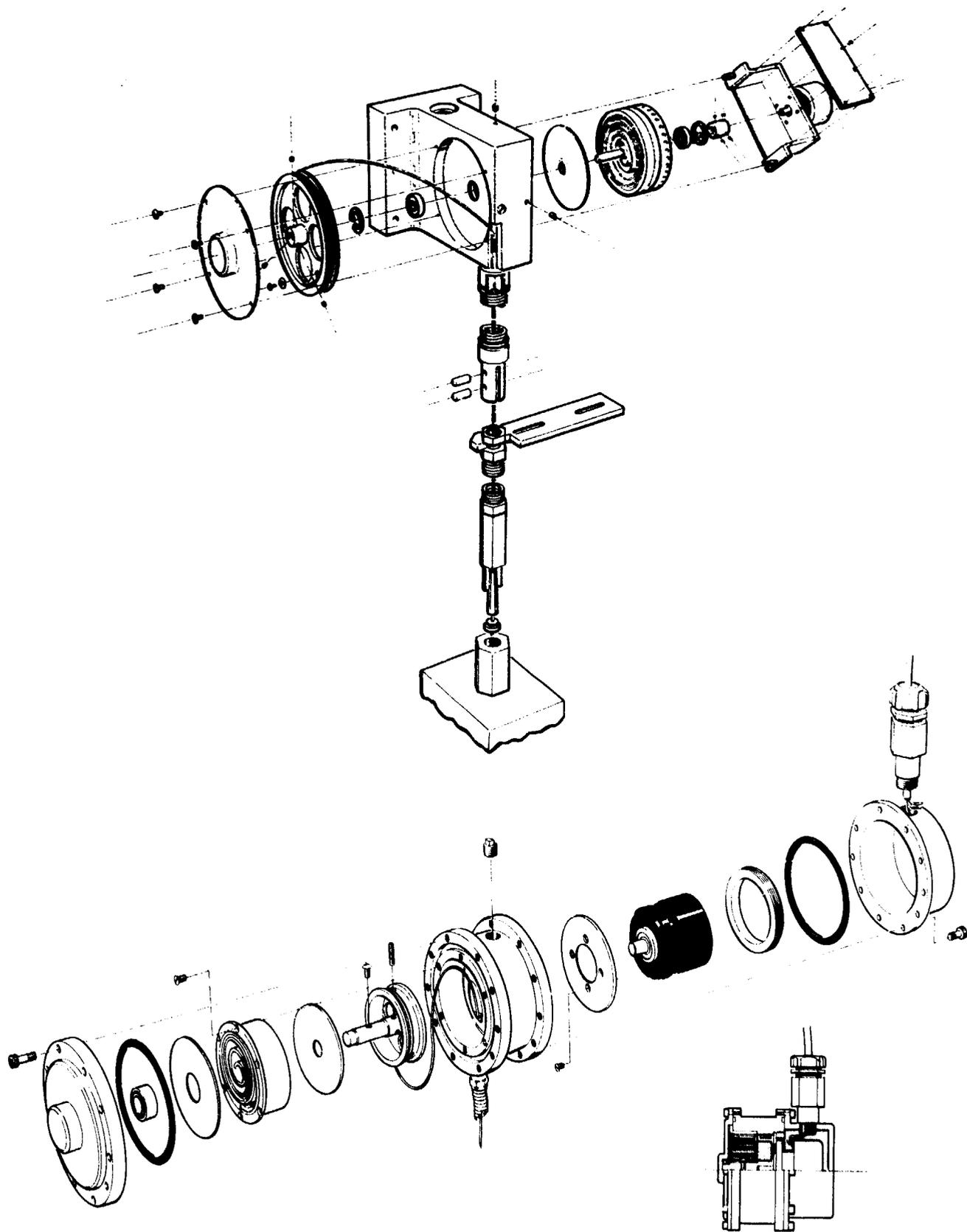
Figure 3, 1   Stretched-Wire Relative Displacement Gage (two configurations)

Figure 3.2 Assembled View of Small Boy 375-foot Instrument Array

Figure 3.3   Installation of Small Boy 375-foot Instrument Array
(Note main canister and one satellite canister.)

Figure 3.4   Small Boy Main Canister Detail
Showing Four Displacement Pickoffs
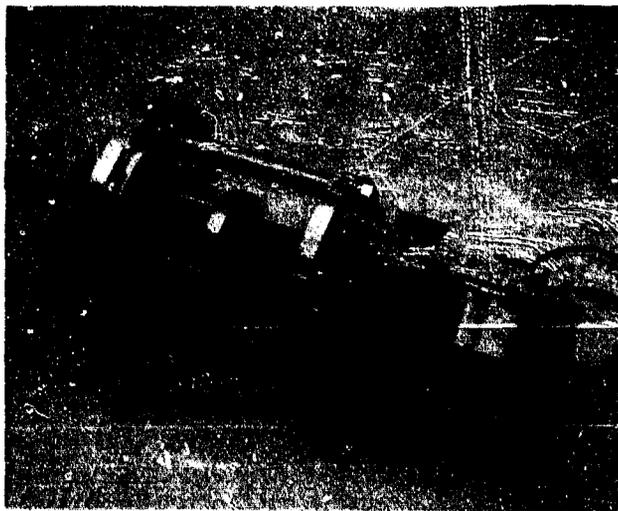
Figure 3.5 Small Boy Satellite Canister Detail Showing
Music Wire Takeup Winch and Canister Orienting Unit

In retrospect several recommendations can be made with respect to long-span displacement gage assemblies. First, any long-base, spring-loaded music wire gage system should be limited to about a 200-foot span. For longer spans frictional forces between the music wire and flexible metal decoupling tubing become so large that, even with additional wire preloading, gage response time is seriously affected. Second, for the particular type of relative displacement gage under discussion — i.e., one in which the displacement pickoffs and music wire preloading springs are located at the bottom or remote end of the instrument array — overall system response time is influenced by several additional considerations. In this system the ground displacement signal arriving at the forward anchor at time t_o is not sensed by the displacement pickoff until some later time $(t_o + \Delta t)$, where the additional delay time Δt is determined by the transit time of a sonic wave in the associated length of music wire and the response time of the displacement transducer-music wire system. In this system the frictional and inertial forces required to accelerate the music wire assembly degrade the system response. In the alternate system (displacement transducer and preload spring forward), the response time of the displacement pickoff is the most significant part of the delay time. Fortunately the portion of the delay time associated with the transit time of the sonic wave can be calibrated out of the response equation with reasonable accuracy. For the Small Boy event the advantages associated with remotely locating the displacement pickoff were felt to outweigh the disadvantages, particularly because of the peculiar geometry of the Small Boy instrumentation plan. Primary advantages were of course associated with the additional shielding afforded by remote location. Thus instrument disturbances due to nuclear and electromagnetic radiations and to ground shock were minimized. For performance details consult Reference 1.

For additional information on the Plumbbob type relative displacement gage system, see References 2 and 3.

Rigid-Rod Gages

A second type of relative displacement device consists of a rigid rod, one end of which is securely anchored to the test medium. The rod is enclosed within a flexible metal housing containing self-aligning bearings at fixed intervals. The metal housing decouples the rod from the test medium, and the bearings permit free rod movement and damp out transverse rod vibrations. A distance transducer is used to measure the relative displacement between the free rod end and a second fixed anchor (Figures 3.6 and 3.7). Several 10-foot gages in various configurations, set

NOTE: All Dim.
called out in inches

Scale: None

5.00 Dia.

Remotely Adjustable
Variable Differential
Transformer and Rod
Unlocking Unit

14.00 to
18.00

Ball-Loc Disconnect

Schaevitz Differ-
ential Transformer

3/8 Aluminum Rod

1/2 I.D. Corrugated Metal
Tubing, Seamless

Gage, Long-Span
Displacement

Scale: 1/8 Approx.

120.00

3/8 Aluminum Rod

3/4 Pipe Union (Bronze)

Nylon Bushing

Anchor Plate
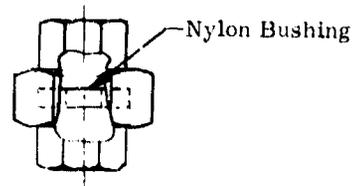
3/4 Pipe Union
With Bushing

6.00 Dia.

Scale: 1/2 Approx.

Figure 3.6   Rigid-Rod Relative Displacement Gage

Figure 3.7   Rigid-Rod Relative Displacement Gage,
Detail

89

up in the laboratory to simulate the buried condition, were excited by an electrodynamic shaker. First significant resonances for 3/8- and 1/2-inch-diameter rods occurred in the region of 300 to 450 cycles per second. Smaller diameter rods resonate laterally at frequencies so low as to preclude their use. Two 10-foot gages were buried near each of two 5000-pound HE bursts and performed satisfactorily (Figure 3.8a). Several 10-foot gages were built with a remote zeroing capability for Gnome and NTS. A record obtained from this gage at a distance of 950 feet from the Gnome explosion is shown in Figure 3.8b, and an NTS record in Figure 3.8c.

Recently the original 10-foot relative displacement gage has been extensively redesigned. These modifications have produced several advantages. Smaller and more sensitive displacement pickoffs can now be used. This reduces the active gage span from 10 feet to 3 feet with no reduction in gage sensitivity. Strains between the limits 2 microinches per inch to 20,000 microinches per inch can be measured with this device. For deep hole installations the remote rod unlatching and transducer zeroing mechanisms have been redesigned; this has produced a shorter and smaller diameter motor and transducer housing, consistent with installation in smaller diameter drill holes. The length has been reduced from a nominal 16 inches to 10 inches and the diameter from 5 inches to 2.25 inches. A recent test of this device near a buried 1000-pound HE detonation at the Coyote test field yielded good displacement data.

Inertial Displacement Gages

In order to measure ground motion directly, a reference point must be chosen which remains fixed with respect to the earth. Since such a reference point must, in general, be located at a great distance from the point of motion, it is more convenient to use an inertial type of displacement gage. Furthermore, when studying large-amplitude displacements, a gage having a sensing-element motion (with respect to the gage case) of only a fraction of the case movement is desirable.

Two mechanical-type inertial displacement gages were designed and constructed. In both of these, the relative motion between sensing mass and case is reduced by coupling the linearly moving sensing mass to a flywheel. This is accomplished with a rack-and-pinion gear in the first gage and a recirculating ball nut in the second.

The moving rack in the first instrument is fastened to a mass carried on a ball bushing which rolls on a splined shaft. The flywheel-and-pinion shaft is mounted on precision ball bearings (Figure 3.9). If M is the mass of the ball bushing assembly, R is the pinion gear radius, and I is the moment of inertia of the flywheel assembly, then the case motion, D, is given by:
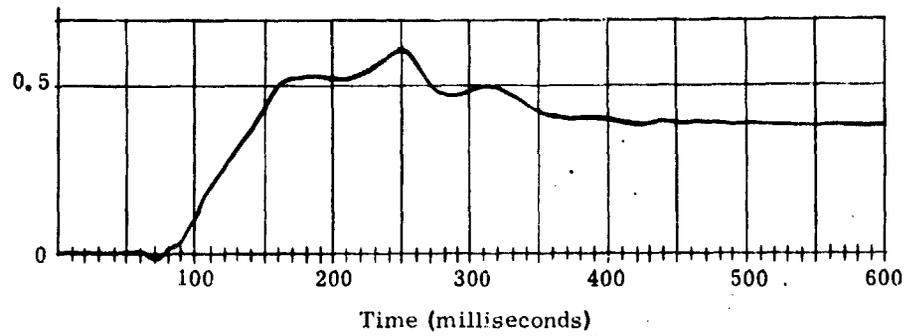
(a) 5000 pounds HE surface burst - tangential motion 50 feet from burst at depth of 2 feet.
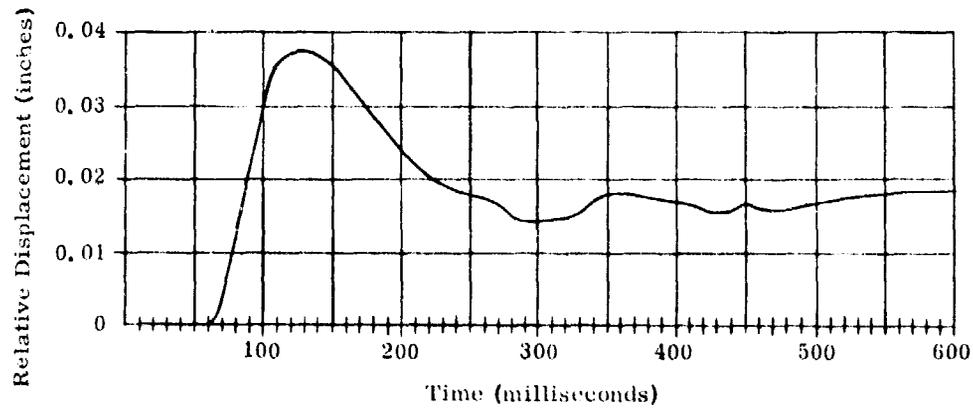
(b) Gnome event - tangential motion 950 feet from burst at shot depth.
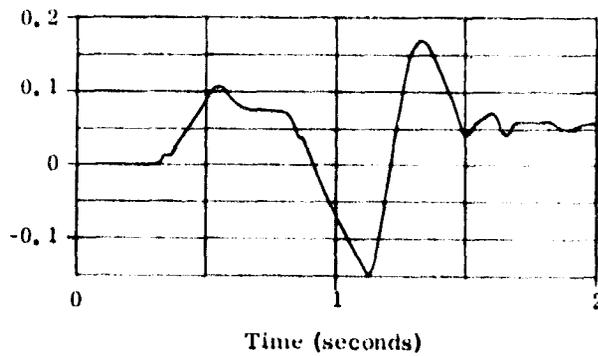
(c) Hognose event at NTS - tangential motion at depth of 2 feet, 1000-foot slant range.

Figure 3.8   Typical Records From Relative Displacement Gage
(10-foot rigid-rod type)
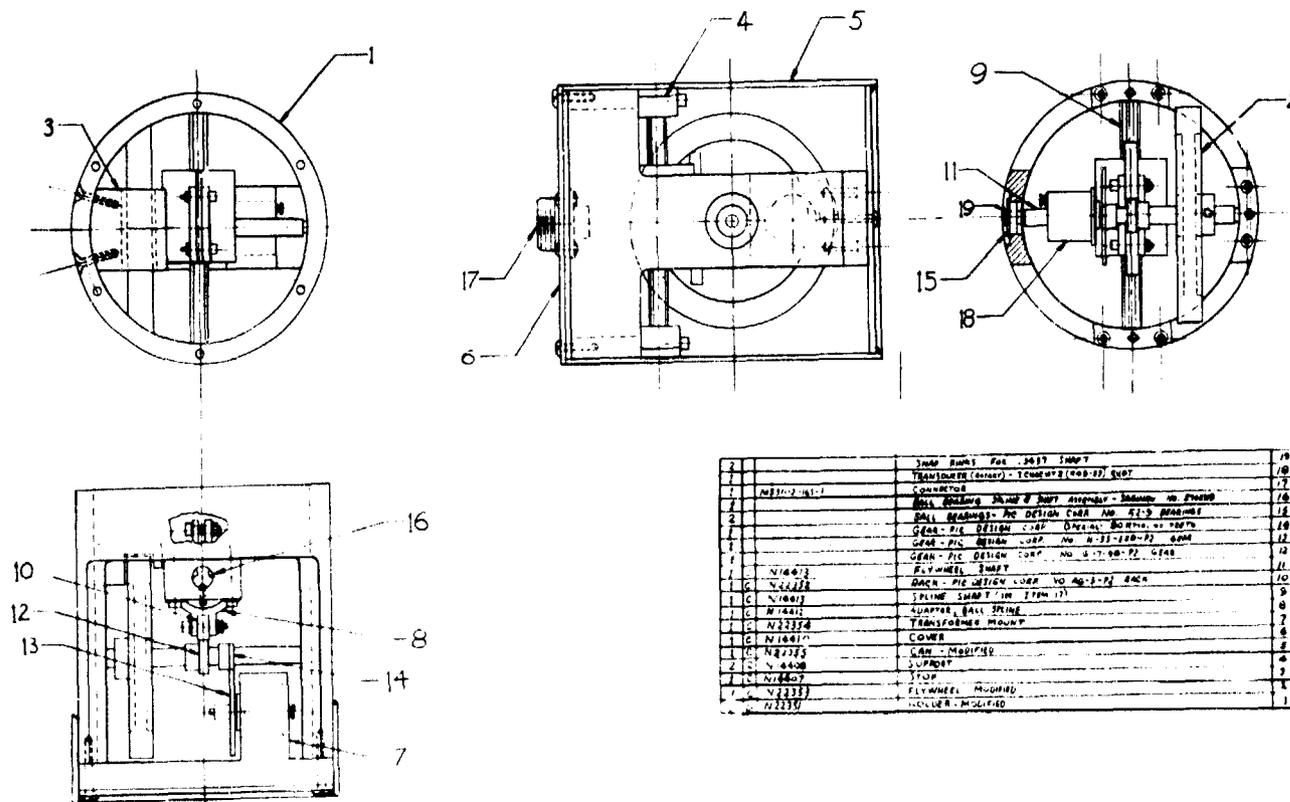
Figure 3.9 Displacement Measuring Mechanism Assembly - Model II

$$D = \left(1 + \frac{I}{MR^2} \right) y, \tag{3.1}$$

where y is the relative motion between the case and the ball bushing.

The output signal is generated from a rotary differential transformer.

The second instrument consists of a helical-splined shaft which supports a recirculating ball-screw nut of the type used on some automotive steering gears. The inductive pickoff includes a ferrite ring mounted on the ball-screw nut and four laminated, soft iron armatures attached to the case. The armatures are tapered and their coils wired in a four-arm bridge configuration (Figure 3.10). In this gage, the case motion, D, is given by:

$$D = \left(1 + \frac{4\pi^2 I}{mp^2} \right) y, \tag{3.2}$$

where I is the moment of inertia of the ball-screw nut assembly, m is the mass, p is the pitch of the screw (linear advance per revolution), and y is the linear displacement of the nut with respect to the case.

Figure 3.10   Spline and Block Assembly

A small sled was constructed for test and evaluation of displacement gages (see Figure 3.11). The sled consists of a carriage approximately 1 foot high which rides on two Thompson ball bushings guided by a pair of parallel steel rods. The carriage is driven by a quick-release coil spring and rebounds from a second coil spring at the far end of the track. The sled displacement output as a function of time is essentially a triangular pulse having an amplitude which is adjustable from zero to 50 inches. The carriage normally makes several round trips, the number depending on the strength of the initial impulse. The largest drive spring can impart an acceleration of well over 100 g to the carriage and gage assembly at full compression.
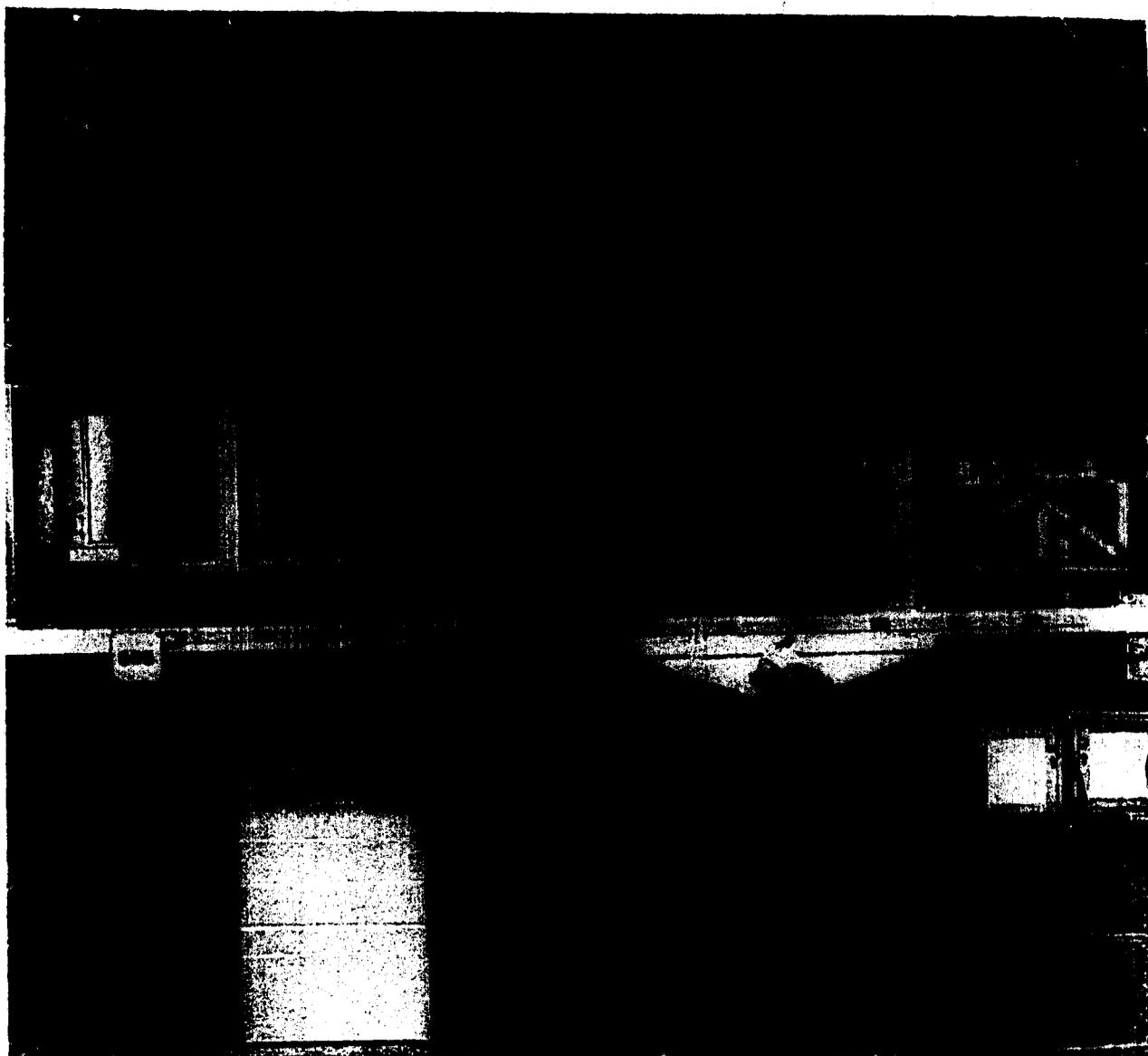
Figure 3.11 Spring-Driven Test Sled

Displacement-versus-time curves were plotted from the displacement sled test data of both the rack-and-pinion and helical-splined inertial displacement gages (Figures 3.12 and 3.13).

Maximum deviation of the rack-and-pinion curve from the true displacement was less than 5 percent of the peak displacement amplitude for the first 1.5 seconds on one run, and 8 percent for the first 2.3 seconds on a second run. These runs were made with different initial driving forces. As the sled slows to a stop, the deceleration forces decrease to a point where they are comparable to the frictional forces in the gage, and the gage error increases. In both of the runs mentioned above, the peak displacement amplitude was about 20 inches, and the sled came to rest in approximately 2-1/2 seconds. The present threshold sensitivity of the gage is 0.04 g.
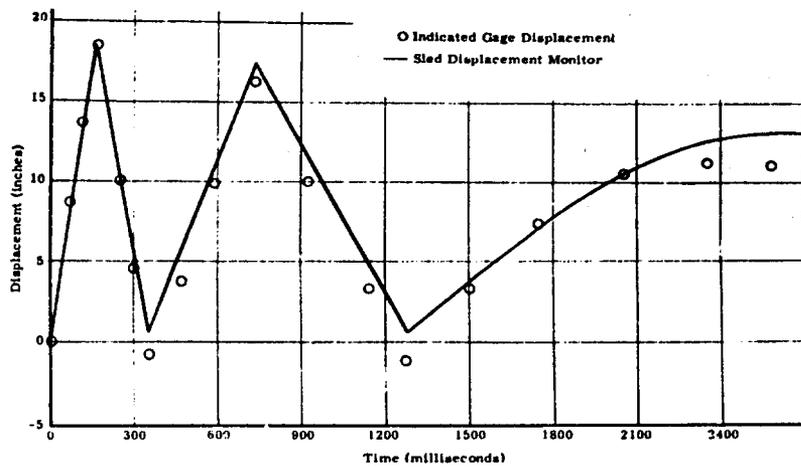
Figure 3.12 Sled Test of Rack-and-Pinion Gage - Model II
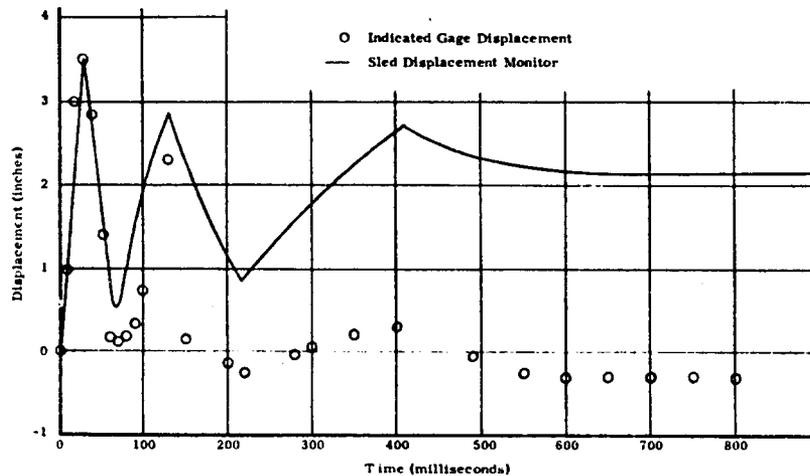
Figure 3.13 Sled Test of Helical-Splined Gage

The internal friction of the helical-splined gage was high enough to produce errors as large as 30 percent of full scale after the first oscillation of the sled. For this reason, together with the facts that its physical size becomes excessive when designed for large displacements and its cost is much greater than the rack-and-pinion device, our efforts were directed toward improvement of the rack-and-pinion gage.

The prototype rack-and-pinion and helical-splined inertial displacement gages were exposed on the HE test mentioned previously. Because of the small motion expected, the flywheel was removed

from the rack-and-pinion gage. Performance of the helical-splined gage was unsatisfactory because of excessive friction. The rack-and-pinion gage indicated a peak displacement of 1.0 inch and a residual permanent offset of 0.25 inch (Figure 3.14a). A precise preshot and postshot survey of a gage-mount bolt showed a permanent displacement of 0.28 inch. Since the maximum relative error of this type of gage usually occurs near the end of the record, and the recorded peaks coincided with the crossover points of a velocity gage located nearby, it is believed that the record was a good representation of actual ground motion. This gage was later used at NTS for surface motion measurements.

(a) 5000 pounds HE surface burst - radial displacement
     50 feet from burst at depth of 2 feet.

(b) Hardhat event, NTS, radial displacement at shot depth,
     600-foot slant range.
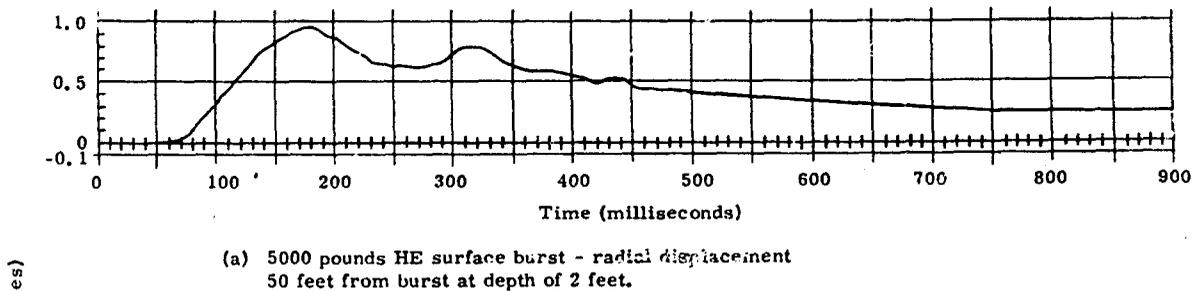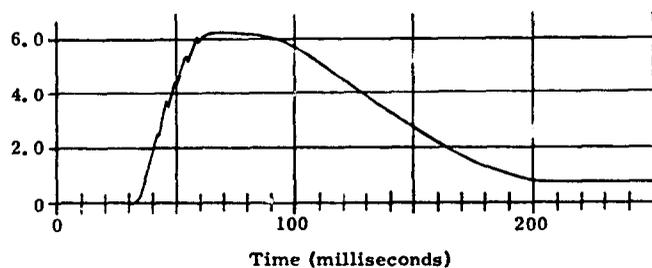
Figure 3.14   Typical Records From Inertial Displacement Gage

The rack-and-pinion gage has been repackaged and modified to permit installation in deep drill holes (both vertical and horizontal). The new external configuration is a 6-inch-diameter sphere, and provision has been made for a remote leveling and calibration capability after the case has been grouted in position (see Figures 3.15 and 3.16). Twelve were built for use at Gnome and NTS. The record obtained at the 950-foot station at Gnome (Figure 3.17a) indicates a residual displacement toward ground zero which is probably not true. This discrepancy is explained by reference to an accelerometer record from the same location (Figure 3.17b). It is seen that accelerations are small after about 0.15 second. Frictional forces in the gage are therefore becoming more significant compared to acceleration forces, and the gage indication is not reliable after this time. This characteristic was also evident on the sled tests. A record from Hardhat at NTS is shown in Figure 3.14b.

Figure 3.15   External Configuration of Inertial Displacement Gage
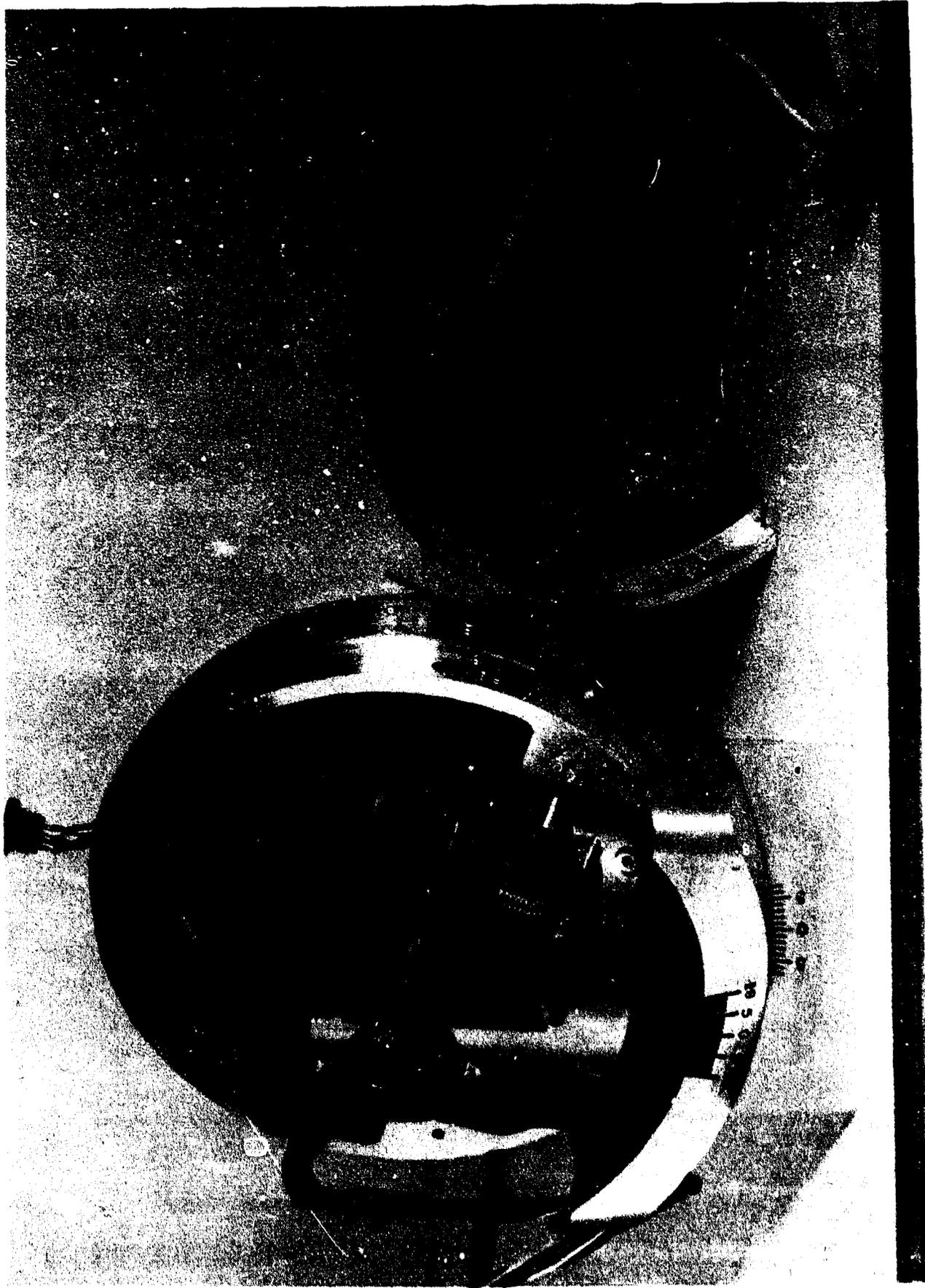
Figure 3.16   Disassembled View of Inertial Displacement Gage
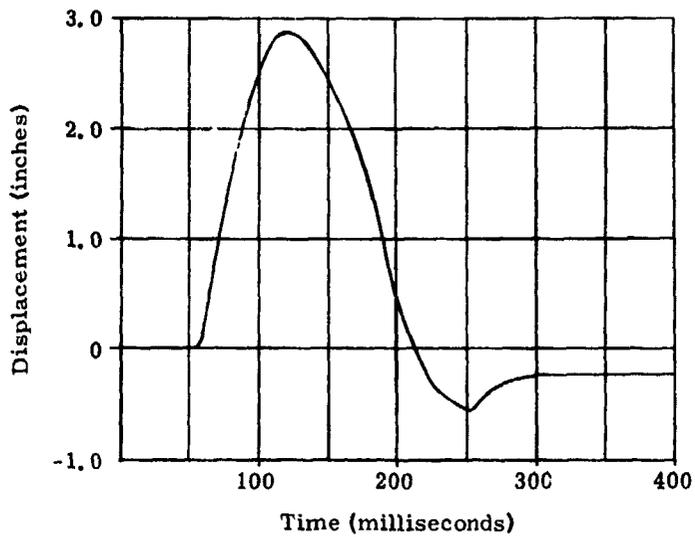
(a) Ground displacement record, 950 feet from Gnome event at shot depth.
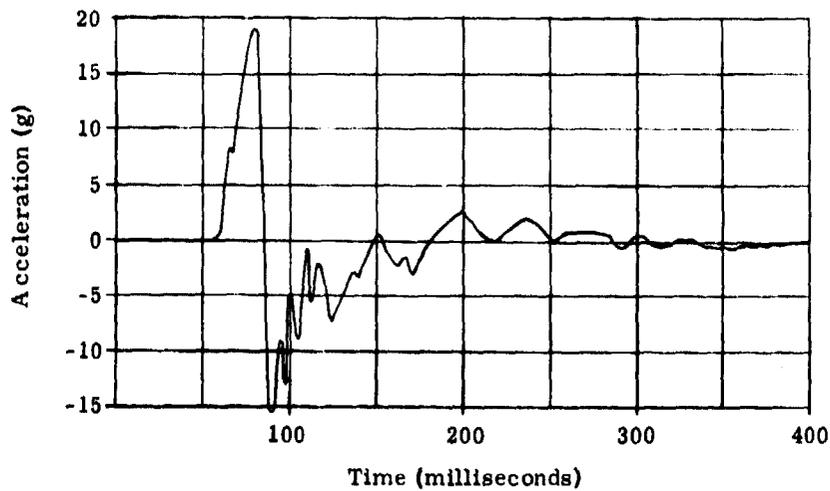
(b) Ground acceleration record, 950 feet from Gnome event at shot depth.

Figure 3.17   Displacement and Acceleration Records From a Nuclear Explosion in Halite

Several ideas have evolved for gage designs which use the same basic operating principle but which should exhibit less friction than present models.

Velocity Gages

Recently considerable effort has been directed toward a redesign of the SRI type velocity gage. This device is basically a highly overdamped, low natural frequency, pendulum accelerometer. This new gage, in conjunction with a single-stage electronic integrator, has yielded good displacement data on experiments conducted with buried HE detonations and the displacement test sled. This modified velocity gage has been specifically designed to extend the range of particle velocity measurements into the 300 ft/sec region and to withstand shock loads in excess of 1200 g. To effect this capability a complete redesign of the pendulum suspension system and pendulum and armature assembly was necessary. Several other changes were made in order to improve the accuracy and repeatability of these gages. A system for filling these gages with DC 200 damping fluid under vacuum was designed. This eliminates damping ratio changes (with consequent amplitude and frequency response errors) caused by air admixture in the damping fluid. To accommodate temperature expansion of the damping fluid a flexible bellows assembly was incorporated in the base of the velocity gage. Figures 3.18 and 3.19 show various views of the present design.
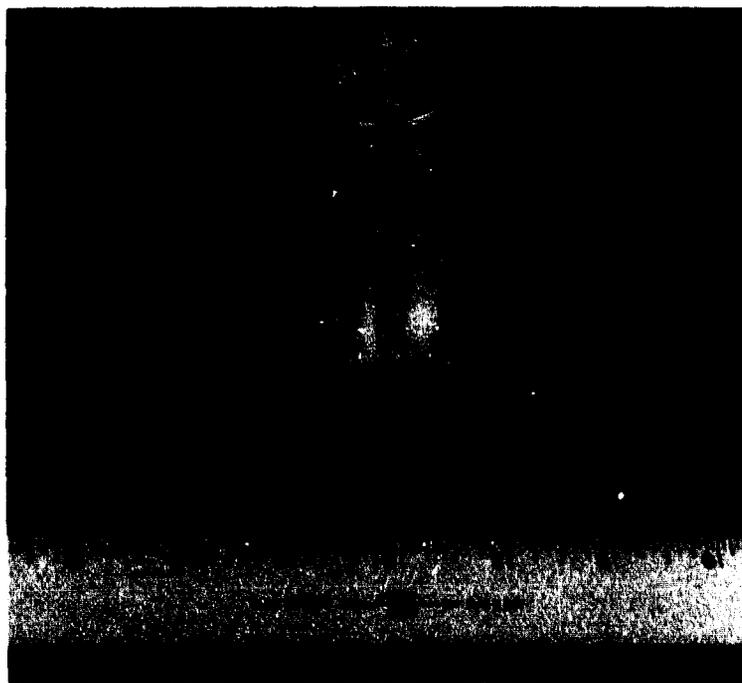
Figure 3.18   Experimental Velocity Gage, Type DS-B(H)
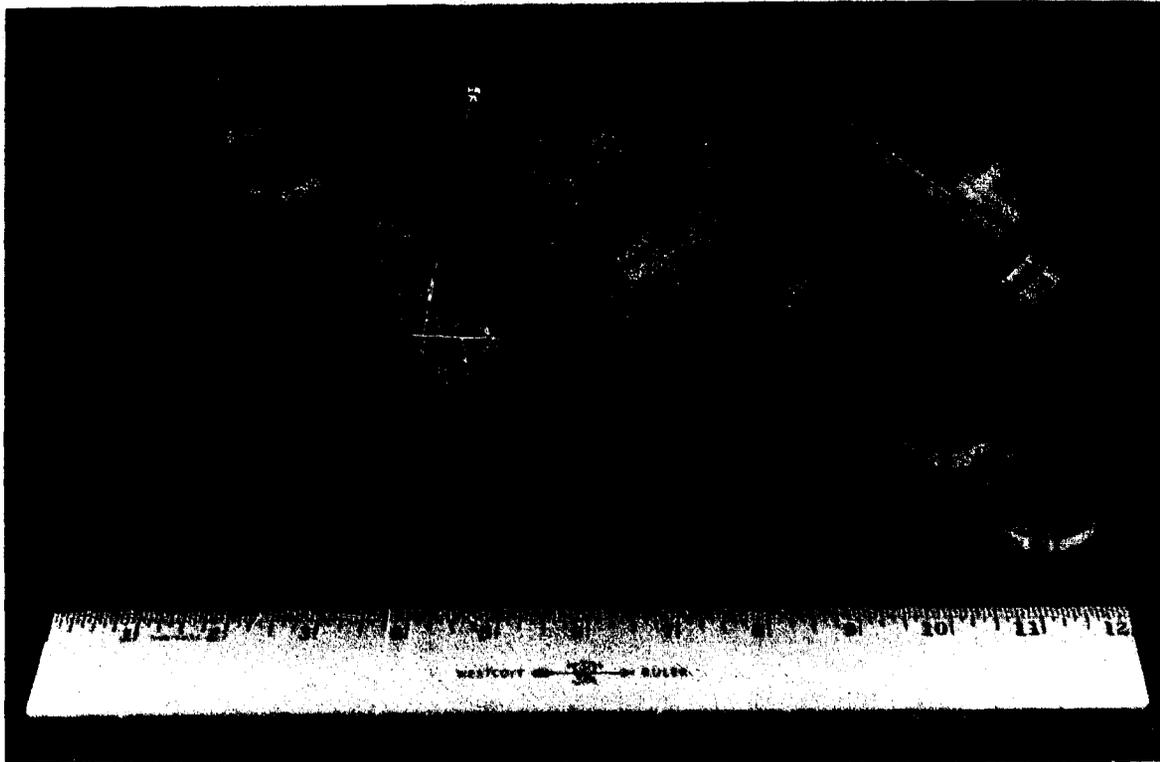
Figure 3.19   Disassembled Experimental Velocity Gage Showing Two Case Configurations

During the recent experiments conducted on subsurface 1000-pound HE detonations, these gages successfully measured peak particle velocities between 0.1 ft/sec and 235 ft/sec; corresponding peak accelerations ranged from 0.5 g to greater than 1500 g. The 235 ft/sec peak velocity was measured at shot depth, 7 feet from the center of a 1000-pound HE sphere, detonated in desert alluvium. A reproduction of this velocity gage record is shown in Figure 3.20.

This velocity gage was later recovered. Extensive postshot tests showed no gage damage; however, a slight loosening of the E-coil hold-down screws was observed. As a result of this test the E-coil hold-down assembly has been redesigned. The hold-down fixture has been strengthened, and epoxy is used to lock the E-coil and hold-down screws in place. Transient gage response records derived from experiments conducted on the displacement test sled are shown in Figures 3.21 and 3.22.

The experimental velocity gages discussed above fall into two categories. One type is basically a low-range model using a brass pendulum, used to measure particle velocities in the range 0.1 ft/sec to 25 ft/sec. Production models of this gage are referred to as type DS-B(H). The "B"

CABLE BROKE SHORTLY
AFTER THIS TIME

COYOTE TEST FIELD HE#3 3-14-63
SHOT DEPTH   12 FT
GAGE DEPTH   12 FT
GAGE RANGE   7 FT
MEDIUM   DESERT ALLUVIUM

TIME MILLISECONDS

PARTICLE VELOCITY FT/SEC
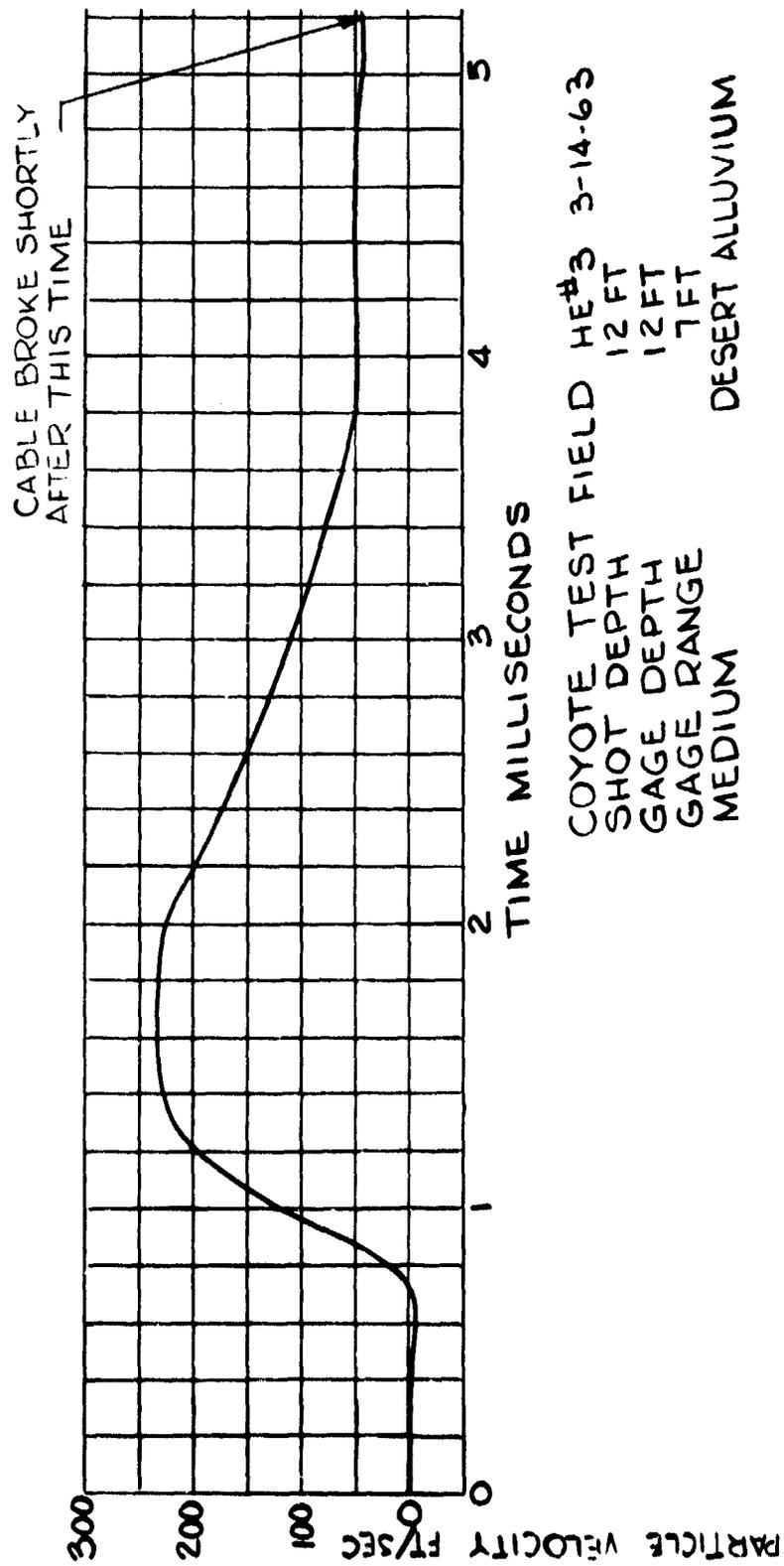
Figure 3.20   Experimental Velocity Gage Record

10 MILLISECOND INCREMENT
TIME

A
63.7G

U_1X
10.67'/SEC

U_2X
10.40'/SEC

AI
10.45'/SEC

D
6.37"

AII
6.0"

1. A=TEST SLED ACCELEROMETER.(WIANCKO±500G)
2. U_1X=EXPERIMENTAL VELOCITY GAGE TYPE I.
3. U_2X=EXPERIMENTAL VELOCITY GAGE TYPE II.
4. AI = ELECTRONIC INTEGRATION OF A.
5. D=SLED DISPLACEMENT MONITOR (SLIDE WIRE PICK-OFF)
6. AII=DOUBLE ELECTRONIC INTEGRATION OF A.

Figure 3.21 Experimental Instrumentation Responses to Impulse From Test Sled

Figure 3.22   Experimental Instrumentation Responses to Impulse From Test Sled

refers to the brass pendulum material and the "H" refers to the horizontal mode of operation. The second type of velocity gage is similar to the above in overall design; however, the pendulum is constructed of aluminum alloy. This model, referred to as type DS-A(H), is designed for operation in high g regions and is normally used to measure particle velocities in the range of 10 ft/sec to 300 ft/sec. The experimental velocity gage record of Figure 3.20 was obtained with a gage of this type. The two experimental velocity gages referred to in Figure 3.21 as $U_1 X$, and $U_2 X$ are identified as follows: $U_1 X$ is an early prototype of the DS-B(H) model; $U_2 X$ is an early prototype of the DS-A(H) model.

Electronic Integrators

Because of the problems of design, calibration, and installation of velocity and displacement instrumentation, we have long desired to be able to obtain velocity and displacement data by integrations of accelerometers. Several attempts to perform integrations using operational amplifiers with capacitive feedback have been made in the past. However, long-term carrier system drift and operational amplifier zero drift have caused the results to be unsatisfactory. This section reports progress made in overcoming these difficulties and describes the development of long-term stabilized single and double integrators.

Single Integrators

The basic circuit for performing integration with operational amplifiers is shown in Figure 3.23a. The current through R is $i = (e_i - e_s)/R$. Since an ideal amplifier draws no input current, this current is also the charging current for the capacitor, C. The voltage across C is

$$V_c = e_s - e_o = (1+A)e_s.$$

Therefore if $A \gg 1$, V_c can be written

$$V_c = Ae_s = -e_o = \frac{1}{C} \int i dt = \frac{1}{RC} \int (e_i - e_s)dt.$$

SUMMING POINT

(a)
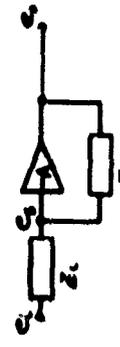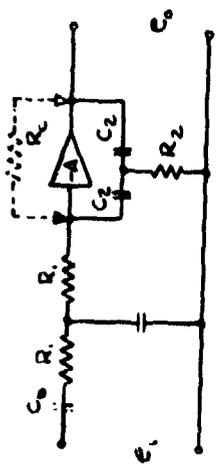
z_f = FEEDBACK IMPEDANCE
z_i = INPUT IMPEDANCE

(b)

(c)

$$z_i = \frac{R_1}{s}\left(s + \frac{1}{R_1 C_1}\right)$$

$$z_f = \frac{1}{C_2\left(s + \frac{1}{R_2 C_2}\right)}$$

(d)
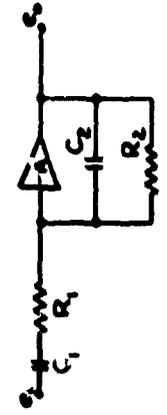
$$z_i = R_1^2 C_1 \left(s + \frac{2}{R_1 C_1}\right)$$

$$z_f = \frac{2\left(s + \frac{2}{R_2 C_2}\right)}{C_2 s^2}$$

(e)

$$z_i = \frac{R_1^2 C_1}{s}\left(s + \frac{2}{R_1 C_1}\right)\left(s + 2R_1 C_b\right)$$

$$z_f = \frac{2}{C_2}\left(\frac{s + \frac{1}{2R_2 C_2}}{s^2 + \frac{2s}{R_1 C_2} + \frac{1}{R_2 R_1 C_2}}\right)$$

(f)

$$z_i = \frac{R_1^2 C_1}{s}\left[s^2 + \frac{2s}{R_1 C_1} s + \frac{1}{R_1 C_1 C_b}\right]$$

$$z_f = \frac{2}{C_3}\left[\frac{s + \frac{R_3 + 2R_2}{2R_2 R_3 C_3}}{\left(s + \frac{1}{R_3 C_3}\right)^2}\right]$$

(g)
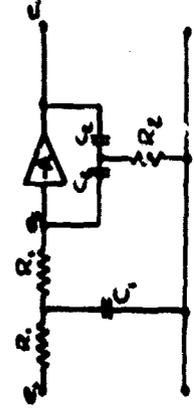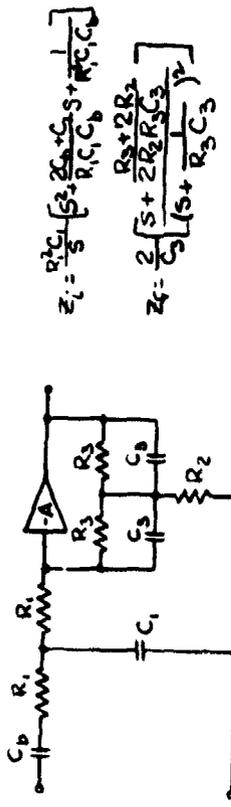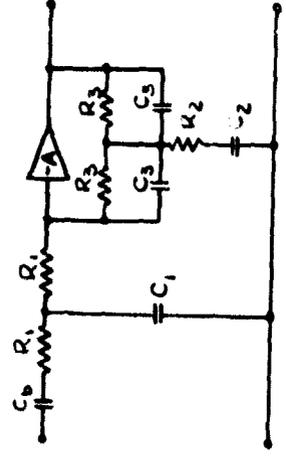
Figure 3.23 Integrator Circuits

Since $e_s = -e_o/A$ and A is very large, the equation becomes $e_o = -\frac{1}{RC} \int e_i \, dt$, which shows that the output voltage is directly proportional to the integral of the input voltage. In general an operational amplifier circuit can be shown as in Figure 3.23b. If A is very large (10^4 to 10^8), then $e_s \cong 0$. Therefore, $E_o/E_i \cong -Z_f/Z_i$.

Using Laplace transform methods to analyze the circuit shown in Figure 3.23a we obtain

$$Z_f = \frac{1}{CS} \text{ and } Z_i = R \text{ where } S = j\omega$$

$$\frac{E_o}{E_i} = -\frac{Z_f}{Z_i} = -\frac{1}{RCS} \text{ or } E_o = -\frac{E_i}{RCS} .$$

Taking the inverse transform we obtain

$$e_o = -\frac{1}{RC} \int e_i \, dt.$$

which is the same answer obtained previously. Therefore the ratio of feedback to input impedance will be used throughout this report to determine circuit performance.

The circuit of Figure 3.23a suffers a number of difficulties in its practical application. A typical instrumentation system consists of a velocity or acceleration gage whose response is amplified by a carrier amplifier; output of the carrier amplifier is then fed to the integration circuitry. The output voltage of the carrier amplifier varies slowly (approximately $\pm$ 50 mv) with time, and, when applied to the circuit of Figure 3.23a, causes e_o to vary several volts, which is sufficient to saturate the signal recorder. In addition, all actual operational amplifiers require a small DC current flowing through Z_f to stabilize them. This current varies from amplifier to amplifier, and for the amplifiers being used (the Astrodata   DA-110) is about 25 to 50 micromicroamperes. This current continuously charges the capacitor C and, unless bled off, allows e_o to again rise to saturation.

To solve these problems the circuit shown in Figure 3.23c was investigated. With this circuit we obtain:

$$\frac{E_o}{E_i} = -\frac{Z_f}{Z_i} = -\frac{S}{R_1 C_2 (S+1/R_1 C_1)(S+1/R_2 C_2)} \cdot$$

Let $T_c = R_1 C_1 = R_2 C_2 =$ stabilization time constant.

Then

$$\frac{E_o}{E_i} = -\frac{S}{R_1 C_2 (S+1/T_c)^2}$$

and for a unit step function input

$$e_o = -\frac{t}{R_1 C_2} e^{-t/T_c} .$$

Therefore it can be seen that, for t less than $0.1 \ t_o$, this circuit will integrate with less than 10 percent error. In practice it is possible to obtain values of $T_c = 30$ seconds or more with good long-term stability. This allows accurate integrations over about 3 seconds. For most measurements the data is obtained in less than 1 second. The single-integration circuit employed in our tests was that of Figure 3.23c.

Double Integrators

The practical problems associated with double-integration circuits are much more severe than those of single integrators. The most common method of performing double integration is to use two single integrators in series. This yields the following form for a step input:

$$e_o = \frac{t^2}{(R_1 C_2)^2} e^{-2t/T_c} .$$

A system of this type will work; however, it has several major problems. The form of the exponential requires that T_c for the two integrators in series be twice as large as T_c for a single integrator to yield the same accuracy. Then too, the output drift of the first integrator is in the pass band of the second and is therefore integrated.

Much of the series amplifier drift problem can be overcome by using the circuit shown in Figure 3.23d for which

$$-\frac{E_o}{E_i} = \frac{2(S + 1/2R_2C_2)}{(R_1S)^2 C_1 C_2 (S + 2/R_1C_1)} \quad .$$

Let $R_1C_1 = 4R_2C_2$. Then for a step input $e_o = t^2/R_1^2 C_1 C_2$, which is the form for true double integration. However, the circuit of Figure 3.23d is very unstable. Some means of compensation must be supplied to eliminate the instability. The simplest method is to apply a leakage path from output to summing point and to block long-term drift in e_i as shown in Figure 3.23e. This circuit produces an oscillatory form in the output voltage for all values of R_c other than $R_c = R_2$. If R_c is made equal to R_2, the circuit is stable and we have

$$\frac{E_o}{E_i} = -\frac{2S}{R_1^2 C_1 C_2} \left[\frac{(S + 1/2R_2C_2)}{(S + 1/R_2C_2)^2 (S + 2/R_1C_1) (S + 1/2R_1C_b)} \right] \quad .$$

If $R_1C_1 = 4R_2C_2$ and $2R_1C_b = R_2C_2$ then

$$-\frac{E_o}{E_i} = \frac{2S}{R_1^2 C_1 C_2} \left[\frac{1}{(S + 1/R_2C_2)^3} \right] = \frac{C_b}{R_2 C_2^3} \left[\frac{S}{(S + 1/R_2C_2)^3} \right] \quad .$$

For a step voltage input we obtain

$$e_o = -\frac{C_b t^2}{2R_2^2 C_2^3} e^{-t/R_2C_2} = -\frac{C_b t^2}{2C_2 T_c^2} e^{-t/T_c} \quad .$$

This is the form desired, performing short-term double integration but having long-term stability.

$T_c = R_2C_2$ must be made large to obtain accurate data. R_2 is limited to $\leq 2\times10^9$ ohms for stability; therefore C_2 is determined when T_c is specified. This means the gain of the circuit is controlled by the value of C_b. For the actual circuit C_b is calculated to be several hundred

microfarads. Low-leakage capacitors of this magnitude become physically impractical, and there-fore this circuit has limited application. To attempt to eliminate these problems the circuit in Figure 3.23f was investigated. If $C_b >> C_1$ and $R_3 >> R_2$ we obtain

$$-\frac{E_o}{E_i} = \frac{Z_f}{Z_i} = \frac{2S}{R_1^2 C_1 C_3} \left[\frac{(S + 1/2R_2 C_3) \cdot}{(S + 1/R_3 C_3)^2 (S^2 + 2S/R_1 C_1 + 1/R_1^2 C_1 C_b)} \right] =$$

$$\frac{2S}{R_1^2 C_1 C_3} \left[\frac{(S + 1/2R_2 C_3)}{(S + 1/R_3 C_3)^2 (S + 2/R_1 C_1)(S + 1/2R_1 C_b)} \right] ,$$

and if $R_1 C_1 = 4R_2 C_3$ and $2R_1 C_b = R_3 C_3$, then we again obtain the proper form

$$-\frac{E_o}{E_i} = \frac{2S}{R_1^2 C_1 C_3} \left[\frac{1}{(S + 1/R_3 C_3)^3} \right] = \frac{C_b}{R_2 R_3 C_3^3} \left[\frac{S}{(S + 1/R_3 C_3)^3} \right] .$$

In this case we find that if R_3 and C_3 are specified and C_b is limited to a reasonable value, gain can still be adjusted by varying R_2. This circuit can be built with reasonable components and double integrates nicely; however, it is very unstable because the voltage divider formed by R_3 and R_2 severely limits the steady state stabilization current flowing from output to summing point. Stabilization can be restored by placing a capacitor in series with R_2 to block the direct current path. The circuit shown in Figure 3.23g is then obtained. Making the assumptions that $C_b >> C_1$ and $R_3 >> R_2$ we see that

$$Z_i = \frac{R_1^2 C_1}{S} \left[(S + 2/R_1 C_1)(S + 1/2R_1 C_b) \right]$$

$$Z_f = \frac{2}{C_3} \left[\frac{(S + 1/2R_2 C_3)(S + 2/R_3 C_2)}{(S + 1/R_3 C_3)^2 (S + 1/R_2 C_2)} \right]$$

Let $R_1C_1 = 4R_2C_3$ and $R_3C_2 = 4 R_1C_b$ and $R_2C_2 = R_3C_3 = T_c$.

Then

$$-\frac{E_o}{E_i} = \frac{Z_f}{Z_i} = \frac{2}{R_1^2 C_1 C_3}\left[\frac{S}{(S + 1/R_3C_3)^3}\right] = \frac{2C_b}{T_c^2 C_3}\left[\frac{S}{(S + 1/T_c)^3}\right],$$

which is again the form desired.

This circuit has been constructed and operated with many values of T_c and gain. With values of $R_3 \leq 2\mathrm{x}10^9$ it will hold zero to ±100 mv for long periods of time. It can be constructed with components of reasonable value and, depending upon the gain desired, accurate double integrations over several seconds can be obtained. Results of some recent experiments using the displacement test sled are shown in Figures 3.21 and 3.22.

Sample Determination of Components

For purposes of example the sled run shown in Figure 3.22 will be used. In this case it was desired to (a) single integrate acceleration to obtain velocity, (b) single integrate velocity to obtain displacement, and (c) double integrate acceleration to obtain displacement.

Acceleration $(A) = 50$ g

Velocity $(U) = 10$ ft/sec

Displacement $(D) = 3$ feet

Using the relationships $U = At$, $D = Ut$, and $D = (1/2) At^2$, the values of the integrator gain constants can be determined. For case (a) above we obtain

$R_1C_2 = t = U/A = 10/(50)(32.2) = 6.21 \times 10^{-3}$ seconds where all components are designated as shown in Figure 3.23c.

Next, values for R_2 and C_1 are chosen as large as possible consistent with the desired stability. For the example, $R_2 = 2 \times 10^9$ ohms and $C_1 = 18\mathrm{x}10^{-6}$ farads.

If $R_1C_1 = R_2C_2 = T_c$, then

$$T_c^2 = R_1R_2C_1C_2 = (6.21 \times 10^{-3})(2 \times 10^9)(18 \times 10^{-6}) = 224$$

or

$$T_c = 14.95 \text{ seconds}$$

$$R_1 = T_c/C_1 = 14.95/18 \times 10^{-6} = 8.30 \times 10^5 \text{ ohms}$$

$$C_2 = T_c/R_2 = 14.95/2 \times 10^9 = 7.5 \times 10^{-9} \text{ farads.}$$

Using the same method for case (b) we obtain

$$R_1C_2 = t = D/U = 3/10 = 0.30 \text{ second.}$$

Let

$$R_2 = 2 \times 10^9 \text{ ohms}$$

$$C_1 = 18 \times 10^{-6} \text{ farads.}$$

Then

$$T_c^2 = (0.30)(2 \times 10^9)(18 \times 10^{-6}) = 10800,$$

or

$$T_c = 104 \text{ seconds,}$$

$$R_1 = T_c/C_1 = 104/18 \times 10^{-6} = 5.8 \times 10^6 \text{ ohms,}$$

$$C_2 = T_c/R_2 = 104/2 \times 10^9 = 52 \times 10^{-9} \text{ farads.}$$

For case (c) the circuit of Figure 3.23(g) is used and we obtain

$$T_c^2 C_3/C_b = t^2 = 2D/A = 6/(50)(32.2) = 3.73 \times 10^{-3}.$$

Let $R_3 = 2 \times 10^9$ ohms and $C_b = 18 \times 10^{-6}$ farads.

Then

$$C_3^3 = t^2 C_b/R_3^2 = (3.73 \times 10^{-3})(18 \times 10^{-6})/(4 \times 10^{18}) = 16.8 \times 10^{-27},$$

$$C_3 = 2.56 \times 10^{-9} \text{ farads}$$

and

$$T_c = R_3C_3 = (2 \times 10^9)(2.56 \times 10^{-9}) = 5.12 \text{ seconds.}$$

For the equations to hold, R_3 must be much greater than R_2. Therefore let

$$R_3 = 100\ R_2.$$

Then

$$R_2 = 2 \times 10^7 \text{ ohms}$$

and

$$C_2 = T_c/(2 \times 10^7) = 2.56 \times 10^{-7} \text{ farads.}$$

Since

$$R_3 C_2 = 4 R_1 C_b$$

$$R_1 = (2 \times 10^9)\,(2.56 \times 10^{-7})/(4)\,(18 \times 10^{-6}) = 7.1 \times 10^6 \text{ ohms}$$

and

$$C_1 = 4 R_2 C_3/R_1 = (4)\,(2 \times 10^7)\,(2.56 \times 10^{-9})/(7.1 \times 10^6) = 2.88 \times 10^{-8} \text{ farads.}$$

These circuits were constructed and the data shown in Figure 3.22 were obtained. It can be seen that in all cases waveforms from integrated channels closely resemble the output of transducers measuring the functions directly. In addition all peak data are accurate to well within ± 10 percent.

LIST OF REFERENCES

1. Perret, W. R., Ground Motion Near Nuclear Explosions in Desert Alluvium, VUF-2000, Sandia Corporation, Albuquerque, N. M. (to be published).

2. Perret, W. R., Ground Motion Studies at High Incident Overpressure, Operation Plumbbob, Project 1.5, WT-1405, Sandia Corporation, Albuquerque, N. M., June 1960.

3. Perret, W. R., Subsurface Motion from a Confined Underground Detonation, Part I, Operation Plumbbob, Project 26.4b, WT-1529, Sandia Corporation, Albuquerque, N. M., August 1961.

Section 4

SPHERICAL SHOCK WAVES FROM UNDERGROUND EXPLOSIONS

R. H. Bishop

Introduction

In order to improve understanding of cratering and seismic-coupling phenomena -- especially for extrapolating from chemical to nuclear explosions -- an analysis of shock waves in solid media has been made. Only spherically symmetric waves are assumed, in uniform unbounded media; these waves are analyzed throughout the entire range of distances from close to the explosion center to distances where linear elastic theory is applicable. Principal results derived from the analysis are pressure-distance decay laws for various geologic materials. Time history profiles are not obtained, but the "effective shell thickness" parameter (which is obtained as a function of the radial distance) indicates the general scale of the shock-wave radial profile, without reference to its shape.

The partial differential equations expressing conservation of mass, momentum and energy, the constitutive relations of the medium in which an explosion occurs, and the appropriate boundary and initial conditions are in principle sufficient to describe completely the wave disturbance generated by an explosion. In practice, however, a general and complete solution is extremely difficult mathematically. Considerable progress toward a solution has been made in the last few years by use of electronic computers, particularly in the immediate or hydrodynamic vicinity of the explosion. Nevertheless, at present there appears to be no computer calculation capable of predicting values for an explosion disturbance which agree with experiments in the variety of media in which data have been obtained and over the complete pressure range from hydrodynamic to elastic.

In addition to the mathematical difficulties, lack of knowledge of media constitutive relations is a major shortcoming. Since methods of solution by computer techniques are relatively difficult and not readily available for general use, a simple, analytical, and easily applied method of solution is highly desirable. It is the aim of this report, first, to make those simplifying approximations and reasonable assumptions for the unknown constitutive relations of the medium so that an analytic solution may be obtained; and, second, to evaluate the resulting solutions by comparison with experimental data.

In the present report, solutions are obtained which are analytic in each of the several different pressure ranges associated with explosive disturbances. Over each range, an approximate relation between stress and strain is described by a set of constant parameters, and a corresponding analytic expression relating pressure and distance is obtained which holds only within that range.

It is known experimentally and from theoretical considerations that an arbitrary initial pressure-distance profile generated by an intense initial disturbance in a medium is generally not maintained during subsequent propagation; it rapidly approaches a certain "steady-state" ultimate shape. The "front" of this ultimate hydrodynamic profile is very steep, almost discontinuous, and the "tail" has a nearly unchanging shape during propagation, being roughly exponential. Taylor (1950)[22] has shown that the shape of the hydrodynamically stable profile of a sufficiently strong spherical shock wave depends only on the adiabatic exponent of the medium. Moreover, the profile remains always "similar" -- i. e., a given fraction of the front pressure is always located at the same relative location between the explosion center and the shock front position at each instant of time, provided the shock remains sufficiently strong. During subsequent propagation at lower pressures, two changes take place: (1) the scale of the profile varies as the front moves along; (2) the shape of the profile varies with R. As a simplifying assumption, we ignore the change in profile shape (2). This change is small as long as the transition from ambient pressure to front pressure is irreversible. Even assuming an invariant profile shape, one must still take account of the change of scale (1), since this is a first-order effect and cannot be neglected even in an approximate analysis. It is useful to define a separate parameter to account for the change in scale of the radial profile which occurs during propagation at relatively low front pressures -- i. e., when the shock is not "strong" in the sense defined by Taylor. This parameter is related to the radial distance (at any instant) from the wave front to a point on the profile where the pressure has decreased to a given fraction of the front pressure. This distance defines a "shell thickness," y, which contains most of the wave energy.

Use of the "shell-thickness" parameter simplifies the mathematical description of shock propagation. The fundamental partial differential equations, which contain time as an independent variable, are required to describe the transient approach to a steady radial profile shape. Assuming a steady shape to have been reached at some early time, we derive ordinary differential equations in which the independent variable is the wave front radius, R, at any instant of time. Integration of these equations gives the curve of pressure as a function of radial distance in any given medium. This latter curve is the principal object of concern in the following analyses, since most of the available data from experiments

can be compared with it. In order to derive the curve, however, the constitutive (stress-strain) relations of the medium must be known in each pressure range. The initial steady shape of the radial profile is determined from Taylor's analysis, but the change of shape which actually occurs during subsequent propagation is ignored in our analytic approximate solutions.

Stress-Strain Description of a Solid Medium

The Hugoniot curve refers to the set of all shock front conditions (p_s, ρ_s) that can be reached from a given initial condition (p_1, ρ_1). In a gas, one may use the following Hugoniot (Taylor, 1950),[22]

$$v_s/v_1 = \rho_1/\rho_s = \frac{\gamma + 1 + (\gamma - 1)(p_s/p_1)}{\gamma - 1 + (\gamma + 1)(p_s/p_1)} \quad ,$$

provided that the parameter γ is defined as

$$\gamma = 1 + (p_s v_s - p_1 v_1)/(E_s - E_1) \quad ,$$

in which p is pressure, v is specific volume or reciprocal of density, and E is specific internal energy. The subscripts 1 and s refer to regions ahead of and behind the shock wave, respectively.

The parameter γ is equivalent to the exponent of a reversible adiabat only for "weak" shocks, so that $p_s - p_1$ is small compared to p_1. In general, γ is a function of p_s.

In terms of the relative fractional change of volume, or "strain," $\epsilon = 1 - v_s/v_1$, and the over-pressure, $\sigma = p_s - p_1$, the Hugoniot may be reduced to

$$1/\epsilon = (1/2)(\gamma + 1) + \gamma p_1/\sigma \quad . \tag{4.1}$$

When σ is large compared to p_1, Equation 4.1 approaches the well known limit $\rho_s/\rho_1 = (\gamma + 1)/(\gamma - 1)$ for "strong" shocks; and when σ is small compared to p_1 Equation 4.1 corresponds to the differential form of the reversible adiabat, $(d\sigma/d\rho)_1 = \gamma_1 p_1 \rho_1^{-1}$, in which γ_1 is the value of γ corresponding to the ambient condition (p_1, ρ_1). That is, γ approaches γ_1 as σ approaches zero.

Equation 4.1 can be applied to a solid medium, but the parameter γ may vary rapidly with the front pressure, σ. For solid media, we make the assumption that the product γp_1 in Equation 4.1 may be replaced by the reversible adiabatic elastic modulus S_1. The quantity γ in this product must also be replaced by γ_1. By definition, $S_1 = \rho_1 (d\sigma/d\rho)_1$, and it is well known that the plane wave propagation velocity, C_1, corresponding to infinitesimal longitudinal strains is $(d\sigma/d\rho)_1^{1/2}$. Thus,

$S_1 = \gamma_1 p_1 = \rho_1 C_1^2$. Equation 4.1 is then expressed in terms of S_1 for any solid medium,

$$\sigma/\epsilon = \rho_1 C_1^2 (1 + x) = S_1 (1 + x) = S_s \quad , \tag{4.2}$$

in which x is defined as

$$x = (\gamma + 1)\sigma \big/ \left(2\rho_1 C_1^2\right) \quad . \tag{4.3}$$

The stress-strain ratio σ/ϵ in Equation 4.2 defines a finite-strain modulus, or "shock modulus," S_s. Thus, we interpret x as the relative fractional correction which converts the elastic-wave modulus, S_1, to the shock modulus, S_s.

The modulus correction, x, in Equation 4.2, has a simple expression in terms of the shock-front propagation velocity, U. This is derived from the Rankine-Hugoniot equation for conservation of mass across a shock front, $u_s/U = \epsilon$, in which u_s is the particle velocity at the front. Eliminating ϵ between this equation and Equation 4.2 and using the momentum equation, $\sigma = \rho_1 u_s U$, we obtain

$$x = (U/C_1)^2 - 1 \quad . \tag{4.4}$$

It should be recognized that the strain, ϵ, in Equation 4.2, takes place in a direction parallel to the direction of plane-wave propagation, so that there is no change of volume in any transverse direction. However, there is always a transverse stress field accompanying the longitudinal stress, σ.

If x is negligible compared to 1, each stress component is directly proportional to the longitudinal strain, ϵ. In this case the strain at the front is infinitesimal, and the corresponding waves are said to be "sonic" or "acoustic." In a solid medium, the transverse stress field depends on Poisson's ratio as well as on the elastic modulus S_1. When σ is large compared to S_1 and x is large compared to 1, stresses generated in a solid by shock waves are termed "hydrodynamic." When σ is comparable to S_1 and x is comparable to 1, the quantity σ is neither acoustic nor hydrodynamic, nor is it simply related to the longitudinal strain, ϵ.

Reversible Strain

Let us consider a spherical compressive wave in a small volume of rock subjected to a uniform lithostatic pressure, p_1. This pressure is due to the weight of air and rock at depth h_s below the surface and is approximately equal to $B + \rho_h g h_s$, where ρ_h is average density of rock, B is barometric pressure, and g is gravitational acceleration. As a spherical shock moves along, the front pressure will eventually decrease to a value less than that necessary to open radial (hoop-stress) cracks. If the

shock overpressure, $\sigma_R = P_s - p_1$, is replaced by a static overpressure of the same magnitude at the wall of a spherical cavity, Lamb (1960)[8] has shown that the static tangential stress, σ_t, due to the excess radial stress, σ_R, is given by $\sigma_t = (1/2)(\sigma_R - 2p_1)$, provided that the medium is linearly elastic. When σ_R exceeds $2p_1$, the cavity wall is subjected to a tensile hoop stress. When σ_t reaches some critical value, T, radial cracks will be formed. If we assume that this static relationship can be extended to a shock wave, the parameter T is equivalent to a dynamic tensile strength in the medium. Then the shock front stress, σ_R', corresponding to the onset of radial cracking is defined by the equation

$$T = (1/2)(\sigma_R' - 2p_1), \quad \text{or} \quad \sigma_R' = 2(T + p_1) \ .$$

The actual maximum reversible stress, p_r, cannot exceed this limit, but it may have some smaller value. Thus, in general, p_r is less than or equal to $2(T + p_1)$.

Since $S_1 = \gamma_1 p_1 = \rho_1 C_1^2$, the reversible adiabatic exponent γ_1 in a solid medium at a moderate ambient pressure, p_1, may be relatively large. For example, if $\rho_1 = 2$ gm/cm^3, $C_1 = 4$ km/sec and $p_1 = 60$ bars (1000-foot depth), $\gamma > 10^3$.

When x is small compared to 1, the strain is small and γ approaches the limit, γ_1. Since γ_1 is generally large compared to 1 in any solid medium, and $S_1 = \gamma_1 p_1$, Equation 4.3 is practically equivalent to

$$x = \sigma/2p_1 \quad (\sigma < p_r) \ . \tag{4.5}$$

When σ is less than p_r, the relation between stress, σ, and strain, ϵ, is given by Equations 4.2 and 4.5. Evidently, the stress is directly proportional to the strain only when x is negligible compared to 1. In general, the relation may be nonlinear even when the strain is reversible ($\sigma < p_r$), because x is not necessarily negligible compared to 1. To see this, we observe from Equation 4.5 that x may have any value less than $p_r/2p_1$, and p_r, in turn, may have any value less than $2(p_1 + T)$. Thus, x may have any value less than $1 + T/p_1$.

Cracking Zone and Crushing Zone

When the radial stress, σ_R, exceeds the reversible limit, p_r, radial cracks will appear first, due to tangential tensile stresses at the spherical wave front. In a range of higher values of peak radial stress, tangential cracks may be expected to form as a result of shear stress failures. Consequently, separate rock fragments will result from a combination of processes resulting in tangential and radial cracks. As the radial stress increases, the fragments may break up, until a granular composition is left as the "crushing-strength," p_c, is approached. We call p_c the effective dynamic compressive

strength. If the peak radial stress, σ_R, is less than p_c, each fragment tends to retain its shape; in this range of stress there is no excessive transverse bulging, and the tangential compressive stress component is negligible compared to the radial stress component. After the first radial cracks have appeared, the tangential stresses become zero, and the radial stress component becomes dominant. All these conditions apply approximately to any radial stress, σ_R, which is less than the dynamic compressive strength, p_c. The region of a medium in which the stress σ_R has values such that $p_r < \sigma_R < p_c$ is termed the "cracking zone," and in this zone the radial stress component is considered as the only stress of importance in a first approximation.

Because the radial stress, σ_R, is directed perpendicularly to any concentric spherical surface, it will diminish inversely as the square of any radial distance in the cracking zone. This is readily seen from the equilibrium equation in spherical coordinates,

$$\frac{\partial \sigma_R}{\partial R} + \frac{2(\sigma_R - \sigma_t)}{R} = 0 \quad ,$$

in which the tangential stress, σ_t, is set equal to zero. The radial stress, σ_R, which is a solution of this equation, varies inversely as the square of the radial distance, R.

This variation is strictly true only for a static radial stress field. We shall assume that the inverse-square law is also obeyed for wave-front stresses in the cracking zone, $(p_r < \sigma_R < p_c)$. It should be recognized that if the radial stress, σ_R, exceeds the crushing strength, p_c, the transverse stress components can no longer be neglected even in a first approximation. In the cracking zone, each rock fragment tends to resist a change of shape, which is described by a finite-strain shear modulus, μ_s. As the radial stress increases in the cracking zone, resistance to change of shape begins to disappear as fragments are broken down into smaller and smaller particles of more regular shape. These ultimate particles tend to resist change of volume rather than change of shape; hence, the shear modulus, μ_s, becomes negligible in that range of stress which exceeds the crushing strength, p_c; this range will be termed the "crushing zone." Now, the stress-strain relation can be described by a finite-strain shock-wave bulk modulus, k_s.

In order to determine a stress-strain relation for a medium which applies to both the cracking zone and the crushing zone, we express the dynamic shock modulus, S_s, in Equation 4.2 in terms of the shock-wave bulk modulus, k_s, and the shock-wave shear modulus, μ_s. By analogy with the acoustic modulus, S_1, representative of infinitesimal strains and expressed by $S_1 = k + (4/3)\mu = \rho_1 C_1^2$, we define finite strain or shock-wave moduli by the corresponding relation, $S_s = k_s + (4/3)\mu_s$. Using

the well known relation $\mu = \rho_1 C_2^2$, where C_2 is the velocity of infinitesimal shear waves, the acoustic bulk modulus, k, can be expressed in terms of the acoustic plane wave modulus, S_1:

$$k/S_1 = 1 - (4/3)(C_2/C_1)^2 \quad . \tag{4.6}$$

In the cracking zone, it is expected that Poisson's ratio remains nearly the same as its "acoustic" value. Thus, $k_s/\mu_s = k/\mu$, $k_s/k = \mu_s/\mu = f$, and $S_s = fS_1$, where f is a constant factor. Solving Equation 4.2 for x gives

$$x_c = (4/3)(\mu_s/S_1) + f(k/S_1) - 1 \quad , \tag{4.7}$$

in which the subscript c refers to the crushing zone or the cracking zone. In the crushing zone, as already explained, the finite-strain shock-wave shear modulus, μ_s, becomes negligible, and Equation 4.7 reduces approximately to

$$x_c = f\left[1 - (4/3)(C_2/C_1)^2\right] - 1 \quad . \tag{4.8}$$

In the crushing zone, the factor f is not strictly constant, as in the cracking zone, but depends on the amplitude of the stress σ. In the absence of experimental data, we shall assume Equation 4.8 in conjunction with Equation 4.2, for the stress-strain relation in the crushing zone. In Equation 4.8, the factor f is equal to the ratio S_s/S_1, in which S_s is the "rapid-strain" shock modulus, and S_1 is the "slow-strain" acoustic modulus. It has been observed by Wuerker (1959)[26] for "mine rocks" and by Watstein (1953)[24] for concrete that the ratio of a rapid-strain modulus to its corresponding slow-strain modulus is about 2. In accordance with these experiments, we use $f = 2$ in Equation 4.8, so that the modulus correction x_c in the crushing zone becomes

$$x_c = 1 - (8/3)(C_2/C_1)^2 \quad . \tag{4.9}$$

Hydrodynamic and Plastic Ranges

When the front pressure, σ, exceeds a certain minimum value, p_m, individual particles merge to produce a continuous fluid with high viscosity, which exhibits "plastic flow." When the pressure exceeds a still higher limit, p_H, the medium displays a completely hydrodynamic character as a low viscosity fluid. We can determine an approximate value for p_m by substituting $x = x_c$ into Equation 4.3, and replacing σ by p_m, which gives $p_m = 2x_c\rho_1 C_1^2/(\gamma + 1)$. This result follows from the fact that we have identified the highest pressure in the crushing zone with the lowest pressure in the plastic zone. The expression for p_m involves the parameter γ. From experimental Hugoniot data, γ may be evaluated using Equations 4.2 and 4.3. It is found that γ is about 2 or 3 in most geologic

materials. These values for γ are accurate in the hydrodynamic range of pressure, $\sigma > p_H$, but approximate in the plastic range, $p_m < \sigma < p_H$.

In the hydrodynamic pressure range, $\sigma > p_H$, γ is very nearly constant. In the plastic range, γ is a slowly varying function of σ, so that in subsequent calculations we shall take it to be constant for all pressures, $\sigma > p_m$, and equal to its value when $\sigma > p_H$.

Pressure Zones Near an Explosion

The schematic diagram of Figure 4.1 illustrates the various pressure regions surrounding an underground explosion. The modulus correction, x, in these same pressure regions is shown as a function of σ in Figure 4.2 for a typical earth material. The information of Figure 4.2 has been converted to a stress-strain diagram in Figure 4.3.

Table 4.1 summarizes the modulus corrections and the stress-strain relations for the various pressure ranges.

The only certain information we have about the properties of solid media is their elastic constants and their Hugoniot, illustrated in Figure 4.2 by the two regions of the curve where the slope is unity. Between these extreme limits of pressure our knowledge of medium properties is imprecise, if not negligible. The two straight-line portions of the curve in the acoustic and fluid pressure ranges must be connected in some fashion. We have made this connection by assumption, using the relations listed in Table 4.1.
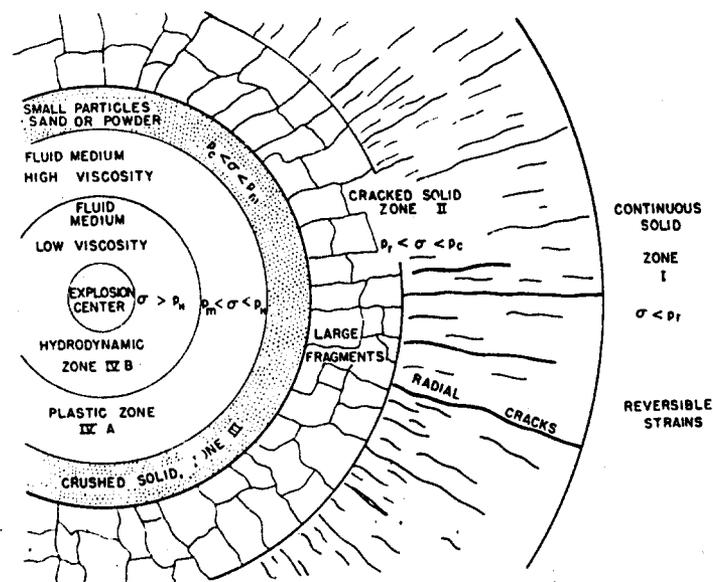
Figure 4.1 Pressure Zones Near an Underground Explosion

KNOWN FROM EXPERIMENT

UNCERTAIN, INSUFFICIENT DATA

ASSUMED IN CALCULATIONS

CONSTANT γ STRAIGHT LINE

(p_2, x_2)

(p_r, x_c) (p_c, x_c) (p_H, x_H)

MODULUS CORRECTION LOG x

CONTINUOUS SOLID

REVERSIBLE STRAINS

ZONE I

(p_m, x_c)

LARGE FRAGMENTS OR RADIAL CRACKS	SMALL PARTICLES	FLUID, HIGH VISCOSITY	FLUID, LOW VISCOSITY
CRACKED SOLID	CRUSHED SOLID	PLASTIC	HYDRODYNAMIC
ZONE II	ZONE III	ZONE IV A	ZONE IV B

STRESS LOG σ

Figure 4.2 Variation of Modulus Correction x With Shock Front Overpressure σ

NOTE: SPACES OCCUPIED BY VARIOUS ZONES ARE NOT TO SCALE

$\epsilon = \dfrac{2}{\gamma+1}$

MAXIMUM STRAIN FOR ANY HUGONIOT COMPRESSION

KNOWN FROM EXPERIMENT

UNCERTAIN, INSUFFICIENT DATA

ASSUMED IN CALCULATIONS

CONSTANT γ CURVE

CONTINUOUS SOLID ZONE I

CRACKED OR CRUSHED SOLID ZONES II AND III

RADIAL CRACKS OR SEPARATE FRAGMENTS

REVERSIBLE STRAINS

MINIMUM STRESS FOR PLASTIC FLOW

p_m

STRESS σ

MAXIMUM REVERSIBLE STRESS

p_r

$\sigma = 2k\epsilon$ $(p_r < \sigma < p_m)$

FLUID MEDIUM HYDRODYNAMIC OR PLASTIC ZONE IV

$\sigma = (k + 4\mu/3)\epsilon$

FOR INFINITESIMAL STRAINS

STRAIN ϵ

Figure 4.3 Variation of Stress σ With Strain ϵ at a Shock Front

TABLE 4.1

Modulus Correction and Stress-Strain Relation in Various Pressure Ranges

Zone	Condition of medium and range of pressure	Modulus correction x	Stress-strain relation, σ versus ϵ
I	Continuous solid, reversible strains, $\sigma < p_r$	$x = \dfrac{\sigma}{2\,p_1}$	$1/\epsilon = \rho_1 C_1^2 \left(\dfrac{1}{\sigma} + \dfrac{1}{2\,p_1}\right)$
II	Cracked solid, large fragments or radial cracks, $p_r < \sigma < p_c$	$x_c' = f_c\left[1 - \left(\dfrac{4}{3}\right)\left(\dfrac{C_2}{C_1}\right)^2\right] - 1$ $f_c \geq 2$	$1/\epsilon = \dfrac{\rho_1 C_1^2 \left(1 + x_c'\right)}{\sigma}$
III	Crushed solid, small particles, $p_c < \sigma < p_m$	$x_c = f\left[1 - \left(\dfrac{4}{3}\right)\left(\dfrac{C_2}{C_1}\right)^2\right] - 1$ $f = 2$	$1/\epsilon = \dfrac{\rho_1 C_1^2 \left(1 + x_c\right)}{\sigma}$ $= \rho_1 U_c^2/\sigma$
IV	Fluid, hydrodynamic or plastic, $\sigma > p_m$	$x = \dfrac{(\gamma + 1)\sigma}{2\rho_1 C_1^2}$	$1/\epsilon = \left(\dfrac{1}{2}\right)(\gamma + 1) + \rho_1 C_1^2/\sigma$

Shell Thickness and Wave Energy

Let us take the shock-wave energy, W_s, as twice the kinetic energy in a spherical volume of radius R, the distance from explosion center to shock front. Near the front, the kinetic energy per unit mass is known to be practically equal to the internal energy per unit mass, provided the front pressure is large compared to ambient. Thus

$$W_s = 4\pi \int_0^R \rho_r u_r^2 r^2 dr \quad,$$

in which ρ_r is density and u_r is particle velocity at radial distance r from the center of explosion. We now __define__ the effective shell volume, V_s, to be equal to $W_s / \left(\rho_s u_s^2\right)$, in which ρ_s is density and u_s is particle velocity at the wave front. Then

$$V_s = 4\pi \int_0^R (\rho_r/\rho_s)(u_r/u_s)^2 r^2 dr \quad.$$

The shell volume, V_s, can be expressed in terms of its thickness, y, and outer radius R, so that $V_s = 4\pi R^2 yF$, in which

$$F = 1 - (y/R) + (1/3)(y/R)^2 \quad . \tag{4.10}$$

Now, letting $n = r/R$, the shell-thickness ratio y/R is found from

$$y/R = (1/F)\int_0^1 (\rho_r/\rho_s)(u_r/u_s)^2 n^2 \, dn \quad . \tag{4.11}$$

Equation 4.11 applies generally to any spherical shock wave, provided the front pressure is large compared to the ambient pressure, p_1.

It follows from replacement of γp_1 by S_1 in Equation 4.1 that ρ_1/ρ_s approaches $(\gamma - 1)/(\gamma + 1)$ when σ is large compared to s_1. From Equation 4.3, this same condition results in a large value of x, regardless of whether a gas or a solid is being considered. Taylor (1950)[22] in his analysis assumes the asymptotic front condition $\rho_1/\rho_s = (\gamma - 1)/(\gamma + 1)$; accordingly, Taylor's analysis can be applied to a solid medium when x is large compared to 1 and the shock wave is strong.

Taylor's theory provides radial profiles for inclusion in Equation 4.11. In terms of Taylor's variables, $\phi(n, \gamma)$ and $\psi(n, \gamma)$, the result is

$$(y/R)_o = \left(\frac{\gamma^2 - 1}{4F}\right)\int_0^1 \psi\phi^2 n^2 \, dn \quad , \tag{4.12}$$

in which the subscript, o, designates a strong shock wave. The values of $(y/R)_o$ calculated from Equations 4.10 and 4.12 and Taylor's formulas for ϕ and ψ appear in Figure 4.4. This shows that the hydrodynamic shell-thickness ratio $(y/R)_o$ is a function only of the medium parameter, γ, and does not depend on R.
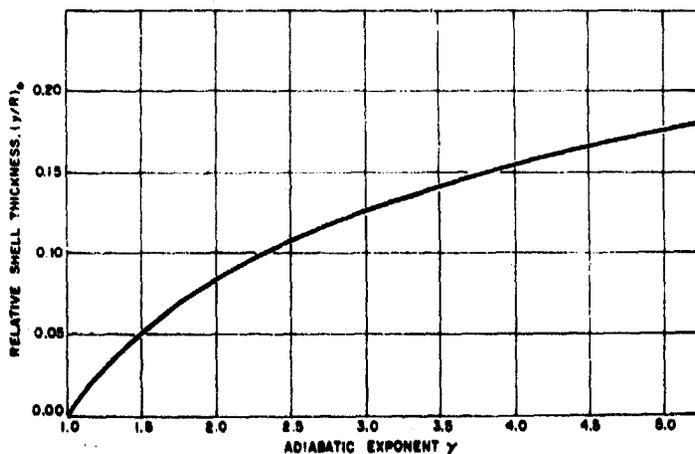
Figure 4.4 Relative Shell Thickness Versus Adiabatic Exponent for Hydrodynamic Shock Waves

Strong Shock Energy and Pressure

It is seen (Figure 4.4) that the shell-thickness ratio $(y/R)_0$ is invariant as R increases, provided γ remains constant and the shock wave remains strong; when x is large compared to 1, a shock is defined to be "strong," regardless of the type of medium. Any spherical blast wave can be described adequately by two parameters, namely, front pressure, σ, and shock energy, W_s. The shock energy can also be expressed in terms of the relative shell thickness, y/R, and the energy density, $\rho_s u_s^2$, at the front. From preceding definitions, $W_s = 4\pi R^3 \rho_s u_s^2 Fy/R$. Energy density, $\rho_s u_s^2$, is related to front pressure, σ, since the change of kinetic energy is $(1/2)u_s^2 = (1/2)\sigma(v_1 - v_s) = (\epsilon/2)(\sigma/\rho_1)$.

Taylor (1950)[22] has shown that there is a simple relation between the front pressure, σ, and the total blast energy, W_t. This quantity is defined as the total kinetic and internal energy associated with all the material inside the entire sphere of radius R. It is sometimes convenient to separate the total blast energy, W_t, into two parts. The shock-wave energy, W_s, has already been described. It is associated with the spherical shell whose outer radius is R and whose inner radius is $R - y$. We now define the "core" energy, W_c, to be equal to $W_t - W_s$. The core energy, W_c, is associated with the spherical volume whose radius is $R - y$.

Taylor (1950)[22] defines a dimensionless pressure, $f(n, \gamma)$, analogous to the relative density, ψ, and relative particle velocity, ϕ, which we have already used in Equation 4.12. From Taylor's result in our notations, the front pressure, σ, is given by

$$\sigma = B(\gamma)W_t R^{-3} \tag{4.13}$$

where

$$B(\gamma) = \left\{ \pi(\gamma + 1)\left[I_1 + (2/\gamma)(\gamma - 1)^{-1} I_2 \right] \right\}^{-1}$$

and $x \gg 1$. It is calculated from two definite integrals through the use of Taylor's formulas for ϕ, ψ, and f.

$$I_1(\gamma) = \int_0^1 \psi \phi^2 n^2 dn ,$$

$$I_2(\gamma) = \int_0^1 f(n, \gamma)n^2 dn .$$

The function $B(\gamma)$ is plotted in Figure 4.5
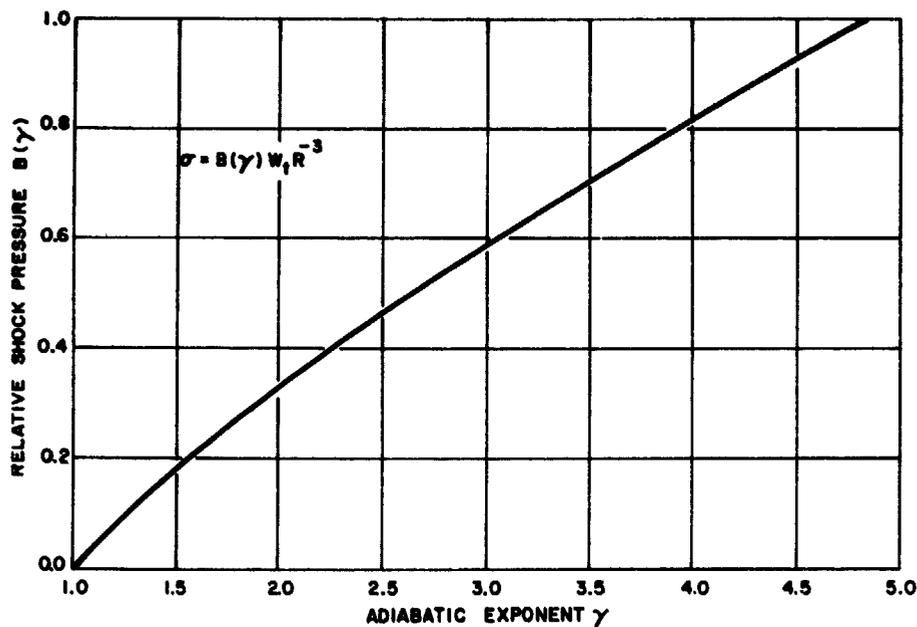
Figure 4.5 Relative Pressure Versus Adiabatic Exponent for Strong Shock Waves

From the strong-shock energy relations, $W_s = 4\pi R^3 \rho_s u_s^2 F(y/R)_o$, $u_s^2 = \epsilon\sigma/\rho_1$, $\epsilon = 2/(\gamma + 1)$, and Equations 4.12 and 4.13, we find that $W_s = 2\pi(\gamma + 1)R^3 I_1(\gamma)\sigma$, $W_s/W_t = 2\pi(\gamma + 1)I_1(\gamma)B(\gamma)$, and also that $W_c/W_t = 1 - W_s/W_t$. The ratio W_s/W_t designates the fraction of the total energy which is partitioned to shock propagation (i.e., in the shell), and the remainder is retained by the core. These fractions depend on the medium; for strong shocks ($x >> 1$) they are functions of γ only. It is also evident that for strong shocks the fraction of energy partitioned to shock propagation is independent of the front radius, R, provided γ is constant. For example, when $\gamma = 3$, $W_s/W_t = 0.8$. Thus, only 20 percent of the total energy is retained by the core in this case; whereas, when $\gamma = 1.4$, $W_s/W_t = 0.42$ and nearly 60 percent of the energy is retained by the core.

Heat Energy Loss From Shell

As shown in the last section, there is no significant loss of energy from a strong spherical shock-wave shell, since γ is nearly constant. As the spherical front radius, R, increases, however, the shock necessarily becomes less strong, and eventually there is an appreciable net loss of energy from the shell. Then W_s becomes a variable, depending on the shock front radius R at any given instant. Since the adiabatic expansion curve of a medium lies above the Hugoniot curve (Figure 4.6), the net loss, Q_s (per unit mass), is always less than the heat, Q, which corresponds to a Hugoniot expansion curve, in

which the final specific volume is the same as the initial specific volume. Let us define

$$Q_s = G_m G_x Q ,$$ (4.14)

where

Q_s = heat which is ultimately lost from the shell and retained by the core;

Q = heat associated with the Hugoniot expansion curve of Figure 4.6;

G_x = factor which depends on shock strength; and

G_m = factor which depends on type of medium.

As we have seen for strong shock waves, the shell energy, W_s, remains constant as the front moves along. Therefore, for strong shocks, Q_s must be zero, although Q is never zero. For shocks which are not strong, neither Q_s or Q is zero.

Figure 4.6 Shock Energy Relations: Pressure Versus Volume

The heat Q is the approximate energy deposited in a solid medium if $\sigma < p_H$, since the final specific volume v_1' is nearly equal to the initial specific volume. It is to account for these observations that it is convenient to introduce the two parameters G_m and G_x. Also, by the introduction of parameters G_m and G_x explicit consideration of adiabats, which are completely unknown for geologic media, is avoided. The shock strength parameter G_x must go to zero as the shock becomes strong in order to account for Taylor's result that the shell energy, W_s, remains constant. The factor G_m is a medium parameter which can be evaluated approximately from an experimental determination of the Hugoniot in the plastic zone. Explicit forms for G_m and G_x will be presented in the following sections.

Referring now to Figure 4.6, the heat energy Q per unit mass is illustrated graphically on a pressure-volume diagram as the area between the Rayleigh line, AC, and the Hugoniot curve. The area enclosed represents the approximate net heat energy, Q, deposited in a unit mass of condensed material. Using the analytic Hugoniot curve described by Equations 4.2 and 4.3, the heat _fraction_ is given by

$$h = Q/u_s^2 = 1/2 - (1/x)\left[(1 + 1/x) \ln(1 + x) - 1\right] \quad , \tag{4.15}$$

in which $u_s^2 = \sigma(v_1 - v_s) = \sigma\epsilon/\rho_1$ represents twice the kinetic energy at the shock front, and is shown in Figure 4.6 as the rectangle ABCD.

When x is small compared to 1, Equation 4.15 reduces approximately to $h = x/6$; and h approaches $1/2$ when x is large compared to 1.

Energy Propagation

From the definition of the effective shell volume V_s, $W_s = \rho_s u_s^2 V_s$. Differentiating this with respect to the front radius R,

$$dW_s/dR = \rho_s\left[V_s\left(du_s^2/dR\right) + u_s^2(dV_s/dR)\right] \quad .$$

in which we neglect the change in front density ρ_s compared to changes in u_s^2 and V_s. Consider the energy loss dW_s from the shell which results when a shock front advances from radius R to radius $R + dR$. Then $dW_s/dR = -4\pi R^2 \rho_1 Q_s$, in which ρ_1 is the ambient density of the medium. Eliminating dW_s/dR from the last two equations provides a differential equation describing variation of shock energy, u_s^2, with distance, R. Using Equation 4.14 and introducing $z = R/y$ we obtain

$$-\left(\frac{d \log u_s^2}{d \log R}\right) = 3 + q - (1/F)\left(\frac{d \log z}{d \log R}\right) \quad . \tag{4.16}$$

$$q = (1/F)zhG_m G_x(\rho_1/\rho_s) \quad , \tag{4.17}$$

in which q is a parameter which denotes the heat energy loss from the shock-wave shell. The variable z represents the ratio of the front radius R to the effective shell thickness y.

Shell Thickness in Hydrodynamic Zone

In order to integrate Equation 4.16 in the hydrodynamic zone where γ is nearly constant, we use the Hugoniot Equations 4.2 and 4.3 and eliminate ϵ through the energy relation $u_s^2 = \sigma\epsilon/\rho_1$. This gives $u_s^2 = \alpha^{-1}\sigma\rho_1^{-1}(1 + 1/x)^{-1}$ in which $\alpha = (1/2)(\gamma + 1)$ and $x = \alpha\sigma/S_1$. From these results, $u_s^2 = \alpha^{-2}\rho_1^{-1}S_1 x^2(1 + x)^{-1}$, and $d \log u_s^2/d \log x = (2 + x)(1 + x)^{-1}$, when γ is constant. Now we can obtain a differential equation from Equation 4.16 which relates the variation of x with R to the variation of z with R in the hydrodynamic zone,

$$-\left(\frac{d \log x}{d \log R}\right) = \left(\frac{1 + x}{2 + x}\right)\left[3 + q - (1/F)\left(\frac{d \log z}{d \log F}\right)\right] \quad .$$

It is evident that this equation cannot be integrated until z is expressed in terms of x and R. Let us assume that

$$d \log z/d \log R = 1/(1 + x) \quad , \tag{4.18}$$

and also that this relationship is valid over all ranges of pressure. It is apparent that Equation 4.18 applies to strong shock waves, where x is large compared to 1, since we have already seen (Figure 4.4) that Taylor's theory requires z to be constant if γ is constant; and so for very strong shock waves, $d \log z/d \log R = 0$. Very weak shock waves, or acoustic waves, correspond to values of x which are very small compared to 1. These also are described by Equation 4.18, since z = R/y and y remains constant, independent of R so that $d \log z/d \log R = 1$. Each "infinitesimal" Fourier component of a very weak disturbance travels at the same "acoustic" velocity, C_1, as is evident from Equation 4.4, since x approaches zero for acoustic waves. Therefore, an acoustic wave pulse does not disperse; it maintains a constant radial extension whose scale is measured by the effective shell thickness, y .

Using Equation 4.18, we obtain a differential equation which describes the variation of x with R in the hydrodynamic zone,

$$-\left(\frac{d \log x}{d \log R}\right) = \frac{2 + 3x + q(1 + x)}{2 + x} \quad , \tag{4.19}$$

where q is defined by Equation 4.17, and F has been set equal to 1. Referring to Equation 4.10 and Figure 4.4, we see that y/R is relatively small for strong shock waves, and F is nearly equal to 1 .

The ratio y/R will become even smaller for weak shock waves, because y tends to remain constant when R increases, as already pointed out. Therefore, we can assume F = 1 for any shock wave, with adequate accuracy.

By eliminating R, a differential equation for z is obtained from Equations 4.18 and 4.19, which is valid in the hydrodynamic pressure range (γ = constant),

$$- \frac{d \log z}{d \log x} = \frac{2 + x}{(1 + x)[2 + 3x + q(1 + x)]} \quad . \tag{4.20}$$

Now we refer to the definition of q in Equation 4.17, and set F = 1. Each remaining factor in Equation 4.17 must be evaluated in order to integrate Equation 4.20. First of all, it is evident that q is directly proportional to z, and the differential Equation 4.20 is consequently nonlinear in the dependent variable z. Moreover, it will become apparent that the remaining factors defining q in Equation 4.17 are complicated functions of the independent variable x. An approximate analytic method is desired in order to avoid numerical integration of Equation 4.20. Fortunately, one can derive an analytical approximation which is sufficiently accurate for most practical purposes.

Loss Factor, q, in Hydrodynamic Zone

It can be shown from Equation 4.20 that z is a slowly varying function of x when x is greater than about 5, regardless of the variation of q with x. This corresponds generally to the hydrodynamic pressure range described in Section 2. Consider now each of the remaining factors in Equation 4.17 which determine the shell energy loss parameter q. In Equation 4.17, F = 1 and h is a function only of x given by Equation 4.15. From Equation 4.15 it is seen that h is a slowly varying function of x when x is greater than 5. From Equations 4.2 and 4.3

$$\rho_1 / \rho_s = 1 - 2(1 + \gamma)^{-1}(1 + 1/x)^{-1} \quad , \tag{4.21}$$

showing that (ρ_1 / ρ_s) is also a slowly varying function of x when x is greater than 5, and when γ is between 2 and 3, values typical of hydrodynamic pressures in solids.

In Equation 4.17 and Equation 4.14, G_x is a shell energy-loss factor which depends on shock strength, and G_m depends on the type of medium. We have seen that G_x approaches zero as x becomes large. By analogy with Equation 4.18, let us assume that $G_x = 1/(1 + x)$, so that Equation 4.14 becomes

$$G_m = (1 + x)(Q_s / Q) \quad , \tag{4.22}$$

and Equation 4.17 becomes

$$(1 + x)q = G_m zh(\rho_1/\rho_s) = q_2 \quad . \tag{4.23}$$

From Equation 4.22 we see that G_m is a slowly varying function of x in the hydrodynamic zone. Note that G_m cannot become large as rapidly as x, because Q_s/Q must approach zero as x increases. This observation indicates that q_2 in Equation 4.23 is a slowly varying function of x, since each of the other factors has already been shown to be a slowly varying function of x. As a result, we assume that some constant average value $\left(q_2\right)_{av} = q_a$ can be used in evaluating Equation 4.20,

$$-\left(\frac{d \log z}{d \log x}\right) = \frac{2 + x}{(1 + x)(2 + q_a + 3x)} \quad ,$$

which can be integrated to give

$$z/z_i = \left(\frac{1 + 1/x}{1 + 1/x_i}\right)^{\frac{1}{3(b - 1)}} \left(\frac{1 + b/x}{1 + b/x_i}\right)^{\frac{b - 2}{3b(b - 1)}} \quad , \tag{4.24}$$

in which

$$b = (1/3)(2 + q_a) \quad . \tag{4.25}$$

In Equation 4.24, $z = z_i$ when $x = x_i$, and in Equation 4.25,

$$q_a = \left(G_m\right)_a z_a h_a \left(\rho_1/\rho_s\right)_a \quad . \tag{4.26}$$

In Equation 4.26, we first examine the variation with respect to x of each of the factors over the hydrodynamic range of pressures.

In order to determine z_a in Equation 4.26, let us find an average value for z over the hydrodynamic range of x. To do this, it is sufficient to examine Equation 4.24 for all values of x in the hydrodynamic range which are smaller than $x = 100$. It is unnecessary to consider Equation 4.24 for larger values of x since z remains practically the same as the strong shock limit, $(y/R)_o = 1/z_o$, given in Figure 4.4. This conclusion also follows necessarily from Taylor's theory, because the actual density ratio ρ_1/ρ_s given by Equation 4.21 differs from Taylor's limit $(\gamma - 1)/(\gamma + 1)$ by less than 1 percent when x is greater than 100.

From Figure 4.2 we find that x_c is the lowest values of x in the plastic zone, and from Table 4.1 it is seen that the same stress-strain relation is used in both the plastic zone and the hydrodynamic zone. In Figure 4.2, the transition between hydrodynamic and plastic pressures occurs where $x = x_H$.

Below this point γ is not constant, and the hydrodynamic equations in which a constant value of γ is not assumed are not strictly valid. If γ is taken to be constant, as a simplifying assumption in the plastic range, $(x_c < x < x_H)$, we can make an additional simplifying assumption in order to avoid calculating a separate lower limit x_c for the hydrodynamic-plastic range in each medium. We shall assume $x_2 = 1/2$ for the "effective-average" lower limit of this range in each medium, and the corresponding pressure will be called the "hydrodynamic termination pressure," p_2 (see Figure 4.2). As determined from Equation 4.3, we obtain $p_2 = S_1/(\gamma + 1)$. This may not be the "best" choice that can be made. Ideally, one should perform a separate analysis of the (curved) plastic zone and determine the variation of x with σ without restricting it to follow a linear relationship (i.e., constant γ) as we have just done. However, the parameters of an extensive geologic formation are not sufficiently uniform to make such an effort rewarding, and our objective here is to make reasonable and simplifying assumptions so that the problem is tractable in analytic form.

From Equation 4.25, it is evident that b is always greater than 2/3, since q_a is never zero in the hydrodynamic range of pressures. It follows from Equation 4.24 that the greatest possible values of z/z_i occur when b has the smallest possible value, namely $b = 2/3$.

Therefore, evaluating Equation 4.24 between limits $x_i = 100$ and $x_2 = 1/2$, and assuming $b = 2/3$, we obtain the greatest possible value for z_2, namely $z_2 = 1.8z_o$. Here z_2 is the value of z at the hydrodynamic termination pressure, p_2, and $1/z_i = 1/z_o$ is the asymptotic limit $(y/R)_o$, shown in Figure 4.4, at the high-pressure end of the hydrodynamic range, where $x_i = 100$. An average value of z can be taken to be half way between $1.8z_o$ and z_o, so that $z_a = 1.4z_o$. Because of the assumption $b = 2/3$, this particular average is an upper limit for any medium, which is approached only by a nearly loss-free medium such as halite or granite. From experimental data we find that $x_H = 3.5$ and $b = 3.28$ in tuff, which differs considerably from the lower limit, $b = 2/3$. In tuff, it is found that $z_a = 1.16z_o$. For desert alluvium, $b = 12.8$, and z_a is less than $1.16z_o$. It turns out as a result that an average value for z in any rock medium, including alluvium, is given by $z_a = 1.2z_o$ with adequate accuracy. This is the value we shall use in Equation 4.26 for all geologic materials.

Returning again to Equations 4.15 and 4.21, it can be seen that both h and (ρ_1/ρ_s) are quite slowly varying functions of x when x exceeds 10, since γ in a solid medium is generally greater than 2 and less than 3. Referring to Equation 4.24, we see that z changes very slowly when x exceeds 10, for any possible value of b. Therefore, we need only consider how these quantities vary in the range from

$x = x_2 = 1/2$ to $x = 10$. The same is also true of G_m, given by Equation 4.22, as we have already shown that G_m must be a slowly varying function of x when x exceeds 10; then ρ_1/ρ_s approaches $(\gamma - 1)/(\gamma + 1)$, and Taylor's theory becomes applicable, at which point Q_s/Q approaches zero.

Referring now to Equation 4.22, we recall that $x = x_H$ at the upper limit of the plastic zone. It is expected that the heat loss, Q_s, should be approximately equal to Q for any value of x less than x_H in the plastic zone. In the plastic zone where $x_c < x < x_H$, Equation 4.22 is simplified by this assumption, giving $G_m = 1 + x$. As explained previously, the general plan of calculation is to obtain an average for h, (ρ_1/ρ_s), and G_m over the range from $x = 0.5$ to $x = 10$. It is not clear how G_m varies when x exceeds x_H. Possibly a good average for G_m over the stated range is the value corresponding to the point where $x = x_H$. Then an approximate average of G_m to be used in Equation 4.26 is $\left(G_m\right)_a = 1 + x_H$.

In principle, one should now take the average of $h(\rho_1/\rho_s)$ over the entire range of x from 0.5 to 10. However, it was not possible to evaluate G_m for any value of x greater than x_H. For this reason, it is expected that a better average for the triple product $G_m(\rho_1/\rho_s)h$ might result from emphasizing the upper end of the range of x near $x = 10$ when an average for the double product $(\rho_1/\rho_s)h$ is being calculated. Since ρ_1/ρ_s is a decreasing function of x and h is an increasing function of x, the product varies quite slowly even for values of x less than 10. Therefore, it is sufficient to evaluate $(\rho_1/\rho_s)h$ at $x = 10$ in order to obtain a satisfactory average to be used in Equation 4.26. From Equations 4.15 and 4.21 we find $h_{10} = 0.336$, and $\left(\rho_1/\rho_s\right)_{10} = 1 - (20/11)/(1 + \gamma)$. Using these expressions together with the preceding equations, $\left(G_m\right)_a = 1 + x_H$ and $z_a = 1.2z_0$, we obtain a general expression for the loss term, q_a, in Equations 4.25 and 4.26,

$$q_a = (0.4)z_0 \, (1 + x_H)\left[1 - (20/11)/(\gamma + 1)\right] \quad . \tag{4.27}$$

In Equation 4.27, z_0 is obtained from Figure 4.4 and a known value of γ for the medium. Values of γ and of x_H for the medium are obtained from a plot of x versus σ using experimental Hugoniot data, and from Equation 4.3. As in Figure 4.2, we obtain x_H from the point at which the plot of x versus σ first departs "significantly" from the hydrodynamic straight line where γ is constant. Below this point, the medium is plastic and γ is not constant. The exact location of this departure is more or less arbitrary. As a rough guide, one can assume that the departure is "significant" when the actual value of x differs by about 30 percent from the value of x obtained by extending the hydrodynamic straight line.

Hydrodynamic Pressure Range

In the hydrodynamic pressure range where σ is greater than p_2, the value of x at any distance R is found by integrating Equation 4.19, using also Equations 4.23 and 4.25,

$$R/R_i = (x_i/x)^{1/3} \left(\frac{1 + b/x}{1 + b/x_i}\right)^{\frac{2-b}{3b}} , \qquad (4.28)$$

where $R = R_i$ when $x = x_i$, and from Equation 4.3 we obtain the pressure, $\sigma/\sigma_i = x/x_i$. It should be observed that γ is assumed to be constant.

Crushing Zone

When the wave-front pressure, σ, is less than p_m, we take $x_c = 1 - (8/3)(C_2/C_1)^2$ as shown by Equation 4.9. We see from Figure 4.2 that, in general, the hydrodynamic termination pressure, p_2 is nearly equal to p_m. Thus, a constant value of x determined by x_c from Equation 4.9 can be used without excessive error for any pressure less than p_2 and greater than the crushing strength, p_c. This particular modulus-correction for the crushing zone is merely an estimate, made necessary by lack of experimental data.

Shock-wave propagation in the crushing zone is not described by Equation 4.28 since γ in the crushing zone varies rapidly with pressure σ. In the crushing zone we use Equations 4.16 and 4.18, with $F = 1$.

$$- \left(d \log u_s^2/d \log R\right) = 3 + q - 1/(1+x_c) , \qquad (4.29)$$

in which $q = G_m(\rho_1/\rho_s)zh(1 + x_c)^{-1}$. Here the heat factor, h, is $x_c/6$ from Equation 4.15, using the approximation for small x. The factor G_m is obtained from Equation 4.22, in which we assume that $Q_s/Q = 1.0$ for the crushing zone, so that $G_m = 1 + x_c$. This combines with Equation 4.9 to give

$$G_m = 2 - (8/3)(C_2/C_1)^2 .$$

It is seen from Equations 4.21 and 4.9 that ρ_1/ρ_s is nearly equal to 1 in the crushing zone. Therefore,

$$q \approx \frac{G_m z x_c}{6(1 + x_c)} ,$$

and Equation 4.29 becomes

$$- \left(d \log u_s^2 / d \log R \right) = 3 - (1 - zx_c G_m/6)/(1 + x_c) \quad . \tag{4.30}$$

Since $u_s^2 = \sigma \epsilon/\rho_1$, it follows from Equation 4.2 that $u_s^2 = \sigma^2 / \left[\rho_1 S_1 (1 + x_c) \right]$ and Equation 4.30 becomes

$$-d \log \sigma / d \log R = 3/2 - (1/2)(1 - zx_c G_m/6)/(1 + x_c) \quad . \tag{4.31}$$

Dividing Equation 4.31 by Equation 4.18, with subscript c in crushing zone,

$$-(d \log \sigma / d \log z) = 1 + 3x_c/2 + x_c z G_m/12 \quad , \quad$$

which can be integrated to give

$$\sigma/\sigma_i = (z_i/z)^{-\dfrac{2 + 3x_c}{2}} \exp \left[-(G_m/12)x_c(z - z_i) \right] \quad . \tag{4.32}$$

In Equation 4.32, $z = z_i$ when $\sigma = \sigma_i$. The ratio z/z_i is obtained by integrating Equation 4.18,

$$z/z_i = (R/R_i)^{\dfrac{1}{1 + x_c}} \quad , \tag{4.33}$$

in which $\sigma = \sigma_i$ and $z = z_i$ when $R = R_i$.

Cracking Zone and Reversible Zone

When the wave-front overpressure, σ, is less than the crushing strength, p_c, and greater than the reversible limit, p_r, the pressure varies inversely as the square of the radial distance, R, as assumed in Section 2 for the cracking zone. Thus,

$$\sigma/\sigma_i = (R_i/R)^2 \quad , \tag{4.34}$$

in which $\sigma = \sigma_i$ when $R = R_i$.

When σ is less than p_r, the strains are reversible and $q_a = 0$. Thus, $b = 2/3$ according to Equation 4.25, and x in the reversible zone is given by Equation 4.5. The curve of σ versus R is found from Equation 4.28 with $b = 2/3$, $x = \sigma/2p_1$, so that

$$R/R_i = (\sigma_i/\sigma)^{1/3} \left(\frac{1 + 4p_1/3\sigma}{1 + 4p_1/3\sigma_i} \right)^{2/3} \quad , \tag{4.35}$$

when σ is less than p_r. In Equation 4.35, p_1 designates the ambient pressure. When $\sigma = p_s - p_1$ is much smaller than p_1, Equation 4.35 approaches $R = \text{constant}/\sigma$, and the pressure, σ, falls off inversely as the first power of the radius, R. This range corresponds to acoustic overpressures, for which x in Equation 4.5 is very small compared to 1.

Table 4.2 lists the stress-decay formulae associated with the various conditions of the medium, and the corresponding ranges of pressure.

TABLE 4.2

Stress Decay Laws in a Solid Medium

Zone	Condition of medium and range of stress	Stress-decay law
I	Continuous solid, reversible strains, $\sigma < p_r$	$\sigma/\sigma_i = (R_i/R)^3 \left(\dfrac{1 + 4p_1/3\sigma}{1 + 4p_1/3\sigma_i}\right)^2$
II	Cracked, large fragments or radial cracks, $p_r < \sigma < p_c$	$\sigma/\sigma_i = (R_i/R)^2$
III	Crushed, small particles, $p_c < \sigma < p_2$	$\sigma/\sigma_i = \dfrac{(R_i/R)^{\frac{2 + 3x_c}{2(1 + x_c)}}}{\exp\left\{\left(\dfrac{G_m x_c z_i}{12}\right)\left[(R/R_i)^{\frac{1}{1 + x_c}} - 1\right]\right\}}$
IV	Fluid, hydrodynamic or plastic, $\sigma > p_2$, $p_2 \cong p_m$	$\sigma/\sigma_i = (R_i/R)^3 \left[\dfrac{1 + 2\rho_1 C_1^2 (b/\sigma)/(\gamma + 1)}{1 + 2\rho_1 C_1^2 (b/\sigma_i)/(\gamma + 1)}\right]^{\frac{2 - b}{b}}$

Initial Conditions

In order to use Equation 4.28 to calculate the relation between σ and R in the hydrodynamic zone, one must first obtain the "initial value," x_i, at some given radius, R_i. Since $x_i = (1/2)(\gamma + 1)\sigma_i/\rho_1 C_1^2$ from Equation 4.3, it is evidently necessary to calculate the pressure, σ_i, at some given initial radius, R_i. This pressure can be calculated for a strong shock wave ($x \gg 1$) in a solid, using Taylor's formulae given above. Strong shock wave, $x \gg 1$, are always produced by buried nuclear explosions.

137

An underground chemical explosion does not produce a strong shock wave, and, accordingly, only a fraction of the incident energy of a detonation wave is transmitted past the boundary of the surrounding medium. The remaining energy is reflected back into the detonation products. In order to calculate the transmitted energy, one must first obtain the energy and pressure of the incident detonation shock wave.

For chemical explosions, the front pressure, p_{sD}, of a detonation shock wave is obtained from the Rankine-Hugoniot mass and momentum conservation relations,

$$u_{sD} = AD \quad , \tag{4.36}$$

$$P_{sD} = \rho_a D u_{sD} = A\rho_a D^2 \quad , \tag{4.37}$$

in which $A = \left(1 - \rho_a/\rho_s\right)_D$ and u_{sD} is particle velocity behind the detonation front. The ambient density of the undetonated explosive is designated as ρ_a and the detonation front velocity is D. Parameter A is the relative fractional volume change from the ambient specific volume, ρ_a^{-1}, to the shock front specific volume, ρ_s^{-1}. The factor A is nearly equal to 0.25 for several types of explosives (Cook, Keyes, and Ursenbach, 1961, Lutzky, 1960).[5,10]

In order to find the pressure, p_t, of the shock wave transmitted into the surrounding medium, one must first obtain the reflection pressure as a function of the reflection particle velocity in the explosive detonation products. When the reflection pressure, p, is greater than the incident detonation front pressure, p_{sD}, the reflection particle velocity, u, is less than the particle velocity, u_{sD}, of the incident detonation wave, and the curve (p, u) is described as a "reflection Hugoniot." When the reflection pressure, p, is less than p_{sD}, the reflection particle velocity, u, is greater than u_{sD}, and the curve (p, u) is termed a "reflection isentrope."

These reflection curves are not generally known from direct measurements, but formulae for calculating an explosive reflection Hugoniot or isentrope have been given by W. E. Deal (1958).[6] Deal's results can be expressed as follows in our notation. When the reflection pressure, p, is greater than the incident front pressure, p_{sD}, the reflection Hugoniot is

$$p/p_{sD} = A_2 + \left(A_2^2 - A_3\right)^{1/2} \quad , \tag{4.38}$$

$$A_2 = 1 + (1/4)(1 - A)^{-1}(1 - u/u_{sD})^2 \quad ,$$

$$A_3 = 1 - (1/2 - A)(1 - A)^{-1}(1 - u/u_{sD})^2 \quad .$$

When the reflection pressure, p, is less than p_{sD}, the reflection isentrope is

$$u/u_{sD} = 1 + \beta^{-1}\left[1 - (p/p_{sD})^{\beta}\right] ,$$

(4.39)

$$\beta = (1/2 - A)(1 - A)^{-1} .$$

The transmitted pressure, p_t, and the transmitted particle velocity, u_t, correspond to the point of intersection (p_t, u_t) of the reflection curve (p, u) with the Hugoniot curve (σ, u_s) of the surrounding medium. The Hugoniot curve (σ, u_s) of the surrounding medium is generally obtained from laboratory experiments. If direct measurements are not available for the medium in question, one can use a theoretical Hugoniot, derived from Equations 2.2 and 2.3 in Section 2, and the kinetic energy relation at the front, $(\epsilon/2)(\sigma/\sigma_1) = (1/2)u_s^2$, which is independent of the shock strength. It is found that

$$u_s^2 = \frac{2\sigma}{\rho_1(\gamma + 1)(1 + 1/x)} ,$$

(4.40)

$$x = \frac{(\gamma + 1)\sigma}{2\rho_1 C_1^2} .$$

(4.41)

Here C_1 is the longitudinal wave propagation velocity for infinitesimal strains in the medium. As already mentioned in Section 2, the adiabatic exponent γ in the hydrodynamic pressure range is about 2 for hard rock, and about 3 for porous wet rock and porous soils. When x is small compared to 1, Equations 4.40 and 4.41 reduce to the correct relation, $\sigma = \rho_1 C_1 u_s$, for small acoustic overpressures (compared to the modulus $\rho_1 C_1^2$), regardless of the particular value assumed for γ in the hydrodynamic pressure range. Therefore, we can use the same constant value of γ in Equations 4.40 and 4.41 over any intermediate pressure range with reasonable accuracy. For very strong shocks, x is large compared to 1, and Equation 4.40 reduces to the simple relation, $\sigma = (1/2)(\gamma + 1)\rho_1 u_s^2$.

Shell Thickness Ratio

In order to calculate the shell thickness of the spherical shock wave transmitted into the surrounding medium from an incident explosive detonation wave, it is first necessary to find the shell thickness, y_e, of the explosive detonation wave, using Equation 4.11. This gives the (constant) shell thickness ratio, $z_e^{-1} = y_e/R_e$, at any spherical detonation front radius, R_e, in the explosive, using known relations between (ρ_r/ρ_s), (u_r/u_s), and $n = r/R_e$ for an explosive which has a given undetonated density, ρ_e. These relations are termed "radial profiles." Such profiles have been calculated by Lutzky (1960)[10]

for several explosives, including TNT at a density $\rho_e = 1.58 \text{ gm/cm}^3$. Radial profiles for pentolite, RDX, tetryl, and RDX/TNT have also been calculated.

It is sometimes necessary to obtain the shell thickness ratio, $z_a^{-1} = y_a/R_a$, for an explosive whose ambient undetonated density, ρ_a, is not the same as the particular density, ρ_e, for which radial profiles have been calculated. An approximate method for finding z_a (at density ρ_a) from a known value, z_e, calculated at density ρ_e, is given by Bishop (1962a).[2]

$$z_a/z_e = (D_a/D_e)^2 \quad . \tag{4.42}$$

Here D_a represents the detonation front velocity which corresponds to an explosive density, ρ_a, and D_e is the velocity which corresponds to a density, ρ_e.

In order to determine the shell thickness ratio, $z_t^{-1} = y_t/R_t$, of the shock wave transmitted into the surrounding medium, compared to the shell thickness ratio, $z_a^{-1} = y_a/R_a$, of the incident detonation wave at the medium boundary, we observe that, in a time y_a/D_a, during which the detonation front moves a distance y_a, the wave front in the medium moves a distance y_t, in a time y_t/U_t, where U_t is the initial shock front propagation velocity in the medium near the boundary. Since the detonation shock wave can supply energy "effectively" only during the time y_a/D_a, the effective shell thickness, y_t, of the shock wave in the medium near the boundary is the same as the distance that its front moves in the same time. Thus, $y_a/D_a = y_t/U_t$, or $y_t/y_a = U_t/D_a$. In terms of the shell thickness ratio z, this relation is equivalent to $z_t = (D_a/U_t)(z_a)(R_t/R_a)$. Since R_t is essentially equal to R_a near the explosive-medium boundary, we have, finally,

$$z_t/z_a = D_a/U_t \quad . \tag{4.43}$$

The shock front propagation velocity, U_t, in the medium can be found from

$$U_t = p_t(\rho_1 u_t)^{-1} \quad , \tag{4.44}$$

since ρ_t and u_t have already been determined.

It is sometimes necessary to adjust the transmitted pressure, p_t, and the transmitted shell thickness ratio, z_t. If p_t is equal to or greater than the plastic flow upper limit, p_H, for the medium, the pressure is said to be "hydrodynamic" (refer to Figure 4.2). In the hydrodynamic pressure range, the hydrodynamically stable shell thickness ratio, $z_o^{-1} = y_o/R_o$, is given by the graph in Figure 4.4 as a function of the adiabatic exponent, γ. If p_t is greater than p_H and z_t is greater than z_o, there

is an unstable balance between the pressure, p_t, and the shell thickness ratio, z_t. The shell thickness ratio must rapidly shift to the stable value, z_o, and the front pressure, p_t, simultaneously shifts to a corresponding stable value, p_o. The shift is completed at a minimum stable radius, R_o, given (Bishop, 1962a)[2] in terms of the initial radius, R_t, at the explosive-medium boundary,

$$R_o/R_t = (1 - 2/z_o)^{-1} \quad .$$ (4.45)

The stable pressure, p_o, is found in terms of the transmitted pressure, p_t, the transmitted modulus correction, x_t, and the stable modulus correction, x_o,

$$p_o = p_t(x_o/x_t) \quad .$$ (4.46)

In Equation 4.46, the stable modulus correction, x_o, is obtained by solving the following quadratic equation, (Bishop, 1962a)[2]:

$$x_o/x_t = (z_o/z_t)(R_t/R_o)^3 \left[\frac{\alpha(1 + 1/x_o) - 1}{\alpha(1 + 1/x_t) - 1}\right] \quad ,$$ (4.47)

in which $\alpha = (1/2)(\gamma + 1)$ and $x_t = (U_t/C_1)^2 - 1$.

Comparison of Calculations With Experiments

Numerous measurements have been made of particle velocities resulting from explosions in various geologic media. Also, from new developments in instrumentation, a considerable number of direct measurements of pressure have recently been obtained, principally in the hydrodynamic zone. Peak particle velocity data may be converted to peak wave front pressures by the momentum relation, $\sigma = \rho_1 U u_s$, if the density, ρ_1, and wave front velocity, U, are known.

The numerous data which have been obtained over the past few years have largely defied accurate theoretical description. Only within the last two years has significant progress been made in attempts to calculate peak wave pressure as a function of distance from explosions in geologic media. Needless to say, very little progress has been made in calculating the particle velocity waveforms which are observed. The foremost difficulty in the theoretical calculation has been and continues to be our great lack of knowledge about the properties of these media, without which meaningful and accurate calculations cannot be performed.

Extensive data have been obtained from both chemical and nuclear explosions buried in four media: granite, halite, volcanic tuff, and desert alluvium. These data have been plotted in Figures 4.7 to 4.11, together with curves calculated from equations derived in the preceding sections. Figure 4.12 compares pressure-distance curves resulting from nuclear explosions in various media.

Hugoniot data used in the calculations for the four media are shown in Figures 4.13 through 4.16. In these figures, the modulus correction, x, is obtained by substituting experimental Hugoniot data into Equation 4.4. Other properties of the media required in these calculations are shown in Table 4.3.

Note that in Table 4.3 the infinitesimal dilatational velocities, C_1, are obtained from the measured wave velocities, U, using $C_1 = U/(1 + x_c)^{1/2}$, from Equation 4.4. As may be observed from the data of Figures 4.7 through 4.11, very few, if any, measurements were made in the acoustic regions around the explosions. In an acoustic region, pressure or peak particle velocity varies inversely as the distance from the explosion, and the acoustic wave front propagates with the velocity, C_1. Since almost all of the measurements of wave arrival were made in the crush-crack zone where peak particle velocities decrease with distance according to a negative power greater than 1, we interpret the measured velocities as being those of finite amplitude waves, and determine C_1 from them by the above formula.

TABLE 4.3

Medium Properties

Medium type	Explosion series or event	Average density ρ_1 (gm/cm^3)	Measured wave velocity U (km/sec)	Infinitesimal wave velocity C_1 (km/sec)	x_c	γ	x_H	Minimum hydro-dynamic pressure p_H (kilobars)
Granite	Hardhat	2.67	5.5[1]	5.2	0.111	2.18	0.72	530
Halite	Cowboy	2.15	4.4[2]	4.2	0.094	2.16	0.23	90
Halite	Gnome	2.15	4.8[3]	4.6	0.094	2.16	0.23	108
Tuff	Hobo	1.85	2.44[4]	2.07	0.385	3.0	3.5	125
Tuff	Rainier	1.85	2.44[5]	2.07	0.385	3.0	3.5	125
Alluvium	Scooter	1.6	1.20[6]	1.04	0.333	3.0	14	135
Alluvium	Teapot Ess	1.6	1.07[7]	0.92	0.333	3.0	20	135

1. Perret, 1963a; Chabai and Bass, 1963
2. Murphey, 1960, Nicholls, Hooker, and Duvall, 1960
3. Weart, 1960
4. Young, 1961
5. Perret, 1961
6. Perret, 1963b
7. Sachs and Swift, 1955

Figure 4.8 Pressure Versus Distance for a Nuclear Explosion in Tuff

Figure 4.7 Pressure Versus Distance for Pelletol Explosions in Tuff

143

Figure 4.10 Pressure Versus Distance for a Nuclear Explosion in Granite

Figure 4.9 Pressure Versus Distance for Explosions in Halite

144
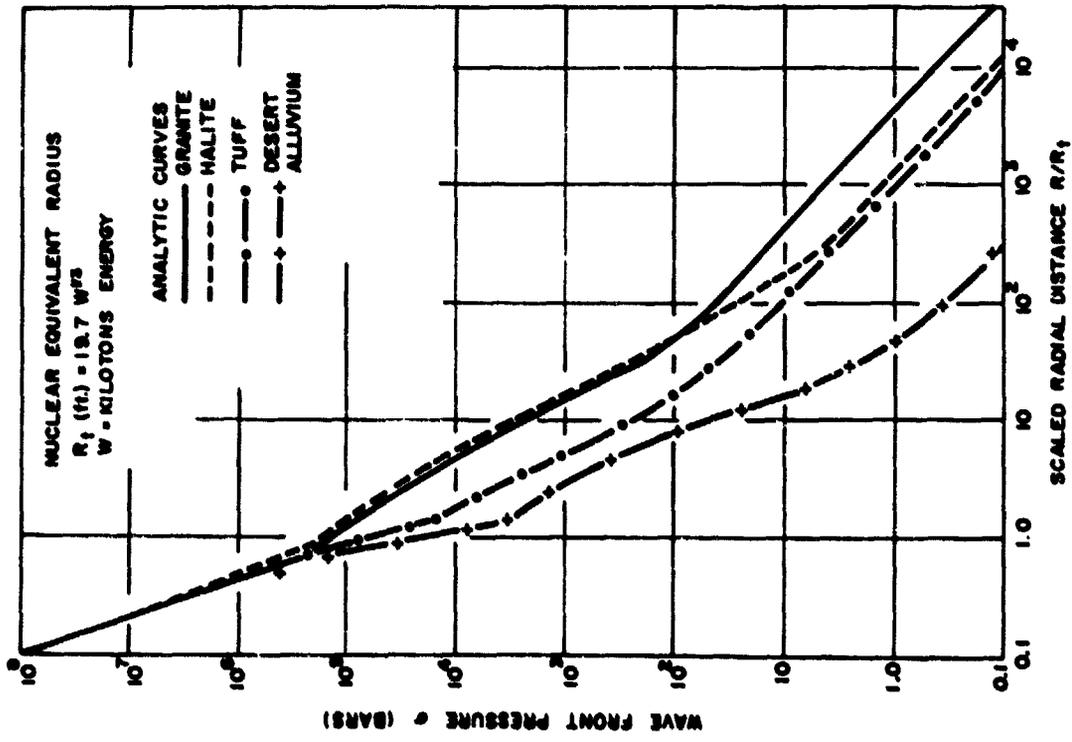
Figure 4.12 Pressure versus Distance for Nuclear Explosions in Various Media
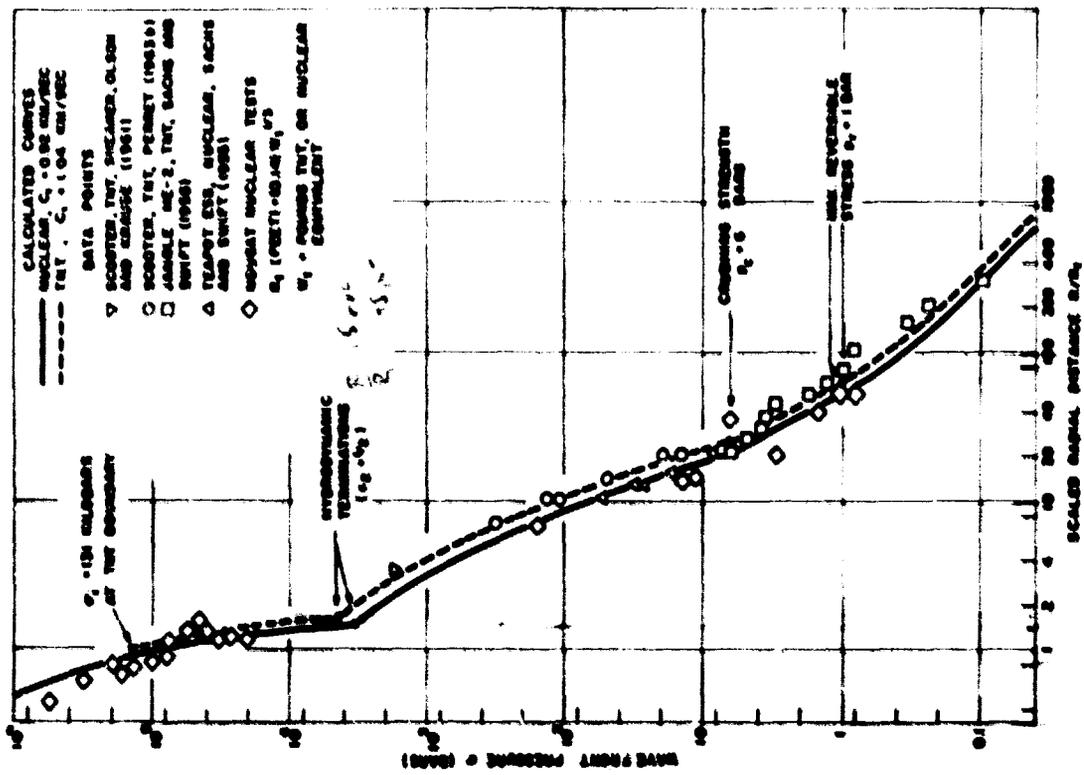
Figure 4.11 Pressure Versus Distance for Explosions in Desert Alluvium

Figure 4.14 Pressure Versus Modulus Correction for Halite

Figure 4.13 Pressure Versus Modulus Correction for Tuff

Figure 4.16 Pressure Versus Modulus Correction for Desert
Alluvium ($C_1 = 1.04$ km/sec)

Figure 4.15 Pressure Versus Modulus Correction for
Granite

To illustrate the method of application of the formulas summarized in Table 4.2, we describe briefly the procedure followed for obtaining the calculated curves of Figures 4.7 to 4.11. For chemical explosions, values of the transmitted quantities p_t, u_t, and U_t in the medium at the explosive boundary, $R = R_t$, are determined by the point of intersection of the medium Hugoniot (σ, u_s) with the reflection curve (p, u) of the explosive, as described under "Initial Conditions" and shown in Figure 4.17 for desert alluvium. The
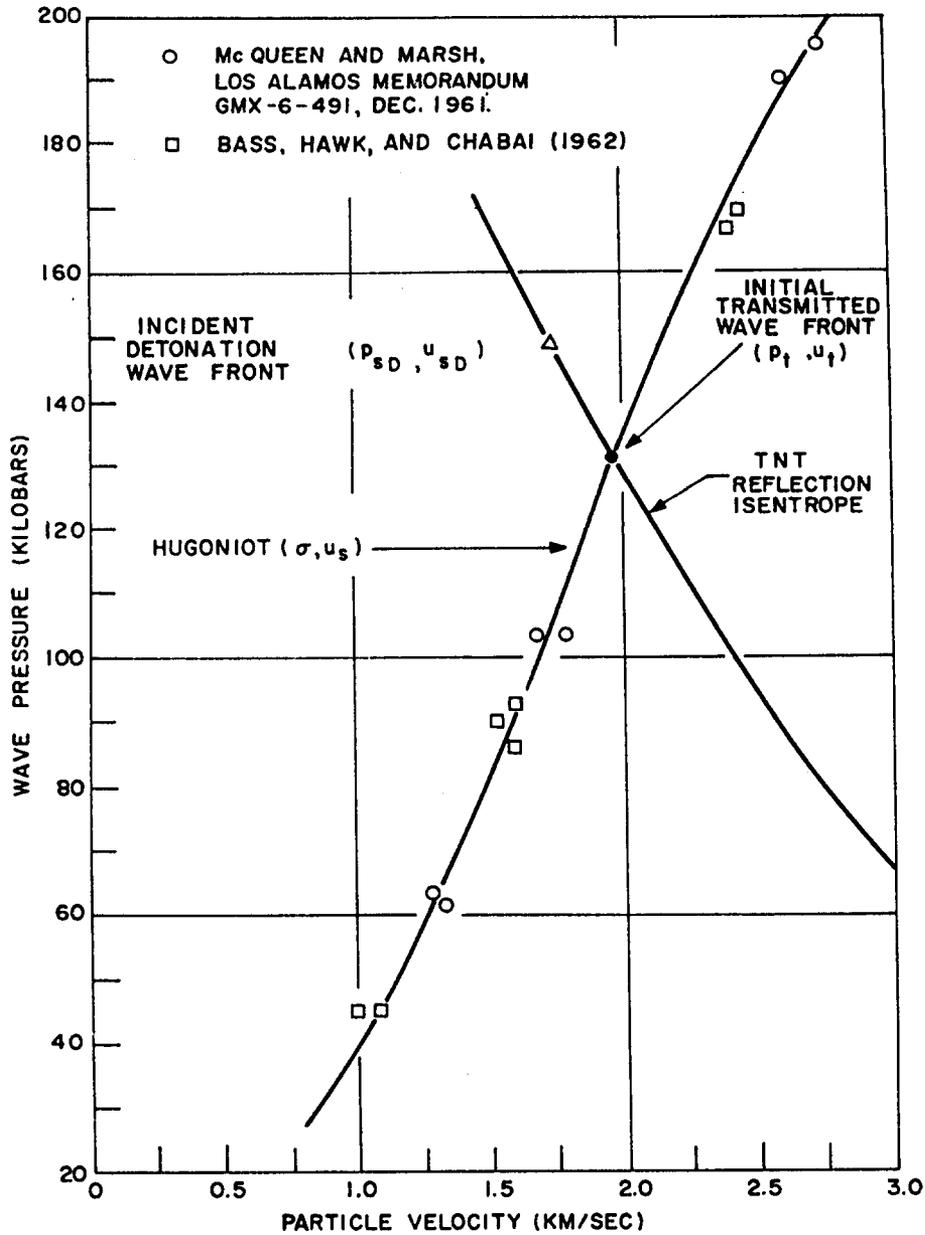
Figure 4.17   Desert Alluvium Hugoniot and TNT Reflection Isentrope
$(\rho_a = 1.375 \text{ gm/cm}^3)$

shell thickness ratio, z_t, of the transmitted wave at the boundary is determined by Equations 4.43, 4.42, and 4.11, in conjunction with the radial velocity and density profiles of the explosive, as explained under "Initial Conditions." The initial value of the pressure, σ_i, in Equation 4.28 is p_t; similarly, we have $x_i = x_t$, and the initial radius R_i is R_t. If $p_H > p_t > p_2$, σ is calculated as a function of R by Equation 4.28, as indicated in Table 4.2, to the distance R_2 at which $\sigma = p_2$ and $x = x_2 = 1/2$. The value of p_2 is obtained directly from $p_2 = p_t(x_2/x_t)$, where $x_t = (U_t/C_1)^2 - 1$.

The value of b must also be computed for use in Equation 4.28. By Equations 4.25 and 4.27, b is readily evaluated in terms of the medium constants γ and x_H, since the shell thickness ratio, $1/z_o$, equal to $(y/R)_o$, is given as a function of γ in Figure 4.4.

The initial value of the shell thickness ratio, z_i, in Equation 4.24, is equal to the transmitted shell thickness ratio, z_t, at the boundary. Since $x_i = x_t$, and $x_2 = 1/2$, we can evaluate the shell thickness ratio, z_2, from Equation 4.24, at the hydrodynamic termination point where the pressure, σ, is equal to p_2. In the range from $\sigma = p_2$ to $\sigma = p_c$, the pressure as a function of distance is determined by Equations 4.32 and 4.33, in which the initial pressure, p_i, is equal to p_2, and the parameter z_i is equal to z_2. In the crack zone, $p_c > \sigma > p_r$, pressure decays inversely as the square of distance (Equation 4.34), and in the reversible zone, $\sigma < p_r$, the pressure falloff is by Equation 4.35.

Since there are no data available regarding the values of p_r for geologic materials, we must estimate p_r from wave pressure and particle velocity data of explosion experiments. In Figures 4.7 to 4.11, we note the minimum pressure level at which σ varies inversely with the square of R; for pressures smaller than this value (which we take to be p_r), the falloff rapidly approaches an inverse R dependence. Values of p_r estimated in this manner are listed in Table 4.4 .

From explosion experiments we can also obtain a value for the dynamic compressive strength, p_c, of an earth material by observing the maximum pressure at which σ varies inversely as the square of R. Fortunately, laboratory determinations of the static value of p_c provide a helpful guide (Duvall and Atchison, 1957; Warner and Violet, 1959).[7, 23] As has been mentioned, laboratory tests reveal that the dynamic strength, p_c, is about twice the static value for several materials (Wuerker, 1959; Watstein, 1953).[26, 24] Whether or not these results from tests on laboratory samples can be applied to gross regions of material in situ is unknown. Nevertheless, such determinations of even static compressive strengths give valuable information for order of magnitude comparison.

TABLE 4.4

Summary of Explosions and Corresponding Numerical Quantities Used in Calculations

Medium and type of explosion	TNT radius R_t (feet)	Energy release W_t	Ambient pressure $p_1 = \rho g h_s$ (bars)	Calculated initial values				Hydrodynamic termination values ($x_2 = 1/2$)			Deduced medium constants	
				σ_i (kilobars)	R_i (feet)	z_i	x_i	p_2 (kilobars)	$\dfrac{R_2}{R_t}$	z_2	p_c	p_r
											(bars)	
Granite, nuclear, Hardhat	33.7	5 kt	80	45,400	4.0	10.5	100	227	0.75	15.6	4000	250
Halite, TNT (pelletol), Cowboy	$0.156 W_t^{1/3}$	Various, 20 lb to 1000 lb	60	87	TNT radius R_t	10.4	0.18	Nonhydrodynamic initial pressure			2500	10
Halite, nuclear, Gnome	28.4	3 kt	76	28,900	3.88	10.5	100	144.5	0.97	16.3	2500	10
Tuff, 240 ft., TNT (pelletol), Hobo	1.54	968 lb	11.4	76	1.54	12.1	2.57	14.8	1.47	14.5	1400	5
Tuff, 1000 ft., TNT (pelletol), Hobo	$0.156 W_t^{1/3}$	103, 516, and 973 lb	64	76	TNT radius R_t	12.1	2.57	14.8	1.47	14.5	1400	80 to 200
Tuff, nuclear, Rainier	23.5	1.7 kt	25 to 60	3,960	7.18	8.0	100	14.8	1.38	10.5	650	–
Desert Alluvium, TNT, Scooter	14	10^6 lb	7.4	(131) 29	(14.0) 18.7	(22) 8.0	(15) 3.4	4.3	1.61	8.7	6	1
Desert alluvium, nuclear, Teapot ESS	18.75	1.2 kt	4.4	680	11.5	8.0	100	3.42	1.46	8.9	–	–

It should be noted that quantities p_c and p_r listed in Table 4.4 for desert alluvium are estimated from the Jangle HE-2 data points plotted in Figure 4.11. The _dynamic_ compressive strength of halite has been measured directly by Nicholls, Hooker, and Duvall (1960).[12]

With regard to the determination of z_i in Equation 4.24, this is generally equal to z_t (Equation 4.43) for most chemical underground explosions, but it is possible for z_t to exceed z_o with certain combinations

of explosives and media. Here, $1/z_o$ is the hydrodynamically stable shell thickness ratio $(y/R)_o$ obtained from Figure 4.4. If, moreover, the initially transmitted pressure, p_t, exceeds the hydrodynamic limit, p_H, as noted under "Initial Conditions," z_t is then an unstable shell thickness ratio and rapidly shifts to the stable value, z_o. Simultaneously, the pressure, p_t, shifts to the stable value p_o determined from Equations 4.45, 4.46, and 4.47. In Table 4.4 the initially transmitted values in parentheses for the Scooter explosion represent unstable quantities in desert alluvium.

For nuclear explosions where the starting pressures are extremely high and the initial disturbance is fully hydrodynamic $(\sigma >> p_H)$, we take any value for x_i which is greater than 10, for example, $x_i = 100$. Then σ_i is given by $\sigma_i = 2\rho_1 C_1^2 x_i/(\gamma + 1)$, from Equation 4.3. Using known values of σ_i, W_t, and γ, the corresponding initial radius, R_i, is obtained from $R_i = \left[B(\gamma)W_t/\sigma_i\right]^{1/3}$, Equation 4.13. Now in the hydrodynamic range, $\sigma_i > \sigma > p_2$, the pressure, σ, varies with distance, R, according to Equation 4.28, and the subsequent calculational procedure is exactly as described above for chemical explosions. Note that in the present context, $z_i = z_o$, and z_o^{-1} is given in Figure 4.4. For complete details of each of the explosion experiments listed in Table 4.4, reference may be made to two research reports by the author (Bishop, 1962a, 1962b).[2]

The energy release, W_t, of the Hardhat nuclear explosion in granite is listed as 5 kt in Table 4.4. It should be pointed out that there is an uncertainty in this value (obtained from radiochemistry) of about 30 percent. The error associated with the 3 kt value for Gnome is in excess of 30 percent, but the errors for the remaining nuclear explosions in Table 4.4 are believed to be less than 20 percent.

Also in Table 4.4, it is to be noted that the initially transmitted pressures $(p_t = p_i)$ from the pelletol (TNT, $\rho_a = 1$) chemical explosions in halite are less than 100 kilobars, and consequently are definitely not hydrodynamic (see Figures 4.9 and 4.14).

The initial shell thickness ratios $(y_i/R_i = 1/z_i)$ in Table 4.4 are of the order of 0.1 for all the explosions listed, indicating that the effective length, y_i, of the wave transmitted into each medium is of the order of magnitude of 10 percent of the starting radius, R_i.

Values of p_1, listed in Table 4.4, refer to the lithostatic pressure at the depth of the associated instrumentation from which data were obtained. For the Rainier explosion, p_1 varies from 25 to 60 bars, corresponding to the depths of the various velocity gages used in that experiment (Perret, 1961).[14] As a result, one might expect the values of p_c and p_r deduced from Rainier to differ somewhat from those for the Hobo explosions, since these quantities may depend upon depth.

Note that, for a nuclear explosion, the parameter R_t in Table 4.4 refers to the radius of an "equivalent" sphere of TNT that would release the same total energy, W_t. The density, ρ_a, of the equivalent TNT sphere is assumed to be 1.0 gm/cm^3 for Gnome, Hardhat, and Rainier, which are compared to TNT (pelletol) explosions in corresponding media. Therefore,

$$R_t(\text{feet}) = (19.7)(\text{kilotons})^{1/3} \quad .$$

The density, ρ_a, is taken as 1.375 gm/cm^3 for the Teapot Ess and Nougat nuclear explosions in alluvium, since these are compared with the Scooter explosion (Figures 4.11, 4.17), for which $R_t = 14$ feet.

There is always a hydrodynamic zone surrounding any tamped nuclear explosion that releases more energy per unit volume than TNT. It was shown from Taylor's strong-shock theory (Equation 4.13) that initially $R_i = \left[B(\gamma)W_t/\sigma_i\right]^{1/3}$ with good accuracy, provided x_i is greater than 10. Therefore, the particular distance, R_i, at which any high pressure, σ_i, occurs ($x_i > 10$) will be proportional to the cube root of the energy, W_t. It is then evident that the radial distance, R, will be proportional to $W_t^{1/3}$ at any given pressure, σ, in the crushing zone, the crack zone, or the reversible zone. Cube-root scaling in each low-pressure zone results from the fact that the termination radius, R_2, at the beginning of the crushing zone is proportional to $W_t^{1/3}$. This last proportionality arises from the fact that σ is a function only of (R/R_i) in the hydrodynamic zone of a given medium (see Table 4.2), and R_i, in turn, is proportional to $W_t^{1/3}$.

In Figure 4.7 are shown data obtained from experiments with pelletol (TNT) explosions in volcanic tuff (Hobo). One series of experiments was conducted at 240-foot depth and another at 1000-foot depth. Scatter in the data is very great. The source of scatter is unknown; it may be due to uncertainties in the values of W_t, gross medium inhomogeneities, large experimental errors, or a combination of these. In order to give an idea of the effect of an inhomogeneity, a curve has been drawn in Figure 4.7 representing calculated pressures in a homogeneous medium with acoustic velocity $C_1 = 2.8$ km/sec and density $\rho_1 = 2.2$ gm/cm^3. Although such a hypothetical medium does not represent actual tuff characteristics, it is interesting to observe that only a slight change in the sonic velocity, C_1, results in a considerable change in the transmitted pressures.

Data from the nuclear explosion in tuff (Rainier) are seen in Figure 4.8 together with the calculated pressure-distance curve. Also shown is a curve for Rainier calculated by Nuckolls (1959),[13] and data of Figure 4.7 from the Hobo experiments at 240 feet.

Figure 4.9 illustrates data from various explosions in salt media (halite). The data are very good, and are well described by the calculated curves within the limits of experimental error. The dotted curve

is from a computer calculation by Seidl (Letter from Lawrence Radiation Laboratory to Sandia Corporation, Albuquerque, New Mexico, October 10, 1961) for a nuclear explosion in halite.

Data from the 5 kt nuclear explosion in granite (Hardhat) are plotted in Figure 4.10. Except for the two valuable and independent measurements of shock pressure near 500 kilobars, the remaining data are all at pressures less than 4 kilobars. It is seen that not enough measurements were made in the elastic region; consequently, it is difficult to estimate the reversible limit stress, p_r, from the pressure data of this figure. The computer curves calculated by Seidl (Lawrence Radiation Laboratory Memorandum, Livermore, California, UOPKA 62-6, January 19, 1962) agree nicely with the two data points near 500 kilobars, but below 10 kilobars Seidl's curves lie definitely above the experimental data points.

Numerous data from explosions in desert alluvium (Figure 4.11) cover almost completely the range of pressures from 500 kilobars to 0.1 bar. Most of the data are results of velocity measurements. In the alluvium hydrodynamic region, shock pressures were measured directly in the Nougat series of nuclear explosions using a new "impedance-mismatch" gage described in Section 1 of this report. Since several of the yields, W_t, of the Nougat explosions are classified, only the scaled distances (R/R_t) can be presented with the measured pressures. Considering the probability that the desert alluvium medium was not identical for all the explosions of this series, it is believed that agreement between calculations and experimental data is excellent.

The theoretical curve for the Teapot Ess alluvium (C_1 = 0.92 km/sec) has been plotted in Figure 4.11 as a solid line. It is seen that the Teapot Ess experimental points agree quite well with this curve. The same is generally true of the Nougat experimental points, but the scatter is much greater than that of the Teapot Ess points.

It is evident that all but one of the Nougat points, as well as all of the Teapot Ess points, are below the corresponding points of the Scooter explosion (TNT). This is probably due to the exceptionally high value of the Scooter alluvium dilatational velocity (C_1 = 1.04 km/sec) rather than to any great difference between nuclear and chemical explosions in the same type of alluvium.

It must be emphasized that the discontinuity in the slope of each calculated curve (Figure 4.12) at the hydrodynamic termination pressure, p_2, is not realistic, but is a consequence of the assumption that γ remains constant throughout the hydrodynamic and plastic zones down to the termination pressure, p_2, as shown by the dashed 45-degree straight line in Figure 4.2. Experimental Hugoniot data (Figures 4.13 to 4.16) reveal that γ is not strictly constant except for a range of pressure ($\sigma > p_H$) which is much greater

than p_2. In the region of pressure near p_2, γ has an average value which differs from that of the higher pressure region which was used in the calculations. The effect of including a variable γ in the calculations would be to remove the discontinuity and to produce a smooth pressure-distance curve which would lie above each one shown in Figures 4.7 to 4.11, in the vicinity of the pressure p_2. The difference in pressures would be comparable to that between the experimental Hugoniot curve (Figures 4.13 to 4.16) and the projection of the 45-degree straight line from the hydrodynamic zone.

Discussion and Conclusions

Review of Assumptions

Calculations have been made, using a constant parameter γ in the plastic zone, where the relation between $\log \sigma$ and $\log x$ is actually a curve. Let us examine the resulting error in halite. Referring to Figure 4.14, we obtain the "constant γ" termination pressure, p_2, from the intersection of the $x = 1/2$ line with the 45-degree hydrodynamic straight line, which gives 132 kilobars. The "exact" value of p_2 is obtained from the curved graph at $x = 1/2$, which gives 139 kilobars.

Another assumption of consequence is the use of $f = 2$ in Equation 4.8. The modulus ratio, $f = S_s/S_1$, is defined in terms of the "rapid-strain" shock modulus, S_s, and the "slow-strain" acoustic modulus, S_1. The modulus ratio, f, is a useful parameter only in the crush-crack zones, where it is nearly constant. In the reversible zone, $f = 1 + x$, which is not constant; nevertheless, it is possible to estimate the upper limit of f for wave front pressures near the reversible limit, where $\sigma = p_r$. Since $p_r < \sigma < p_c$ in the crack zone (Figure 4.2), the upper limit of f in the reversible zone should provide an estimate for the nearly constant value of f in the crack zone (and also in the crush zone). As shown following Equation 4.5, x may have any value less than or equal to $1 + T/p_1$ in the reversible zone. Here, p_1 is the ambient pressure, and T is the dynamic tensile strength. Therefore, f may have a maximum value of $2 + T/p_1$ in the reversible zone. The value of f in the crack zone is probably comparable to 2, since the term T/p_1 does not apply to the crack zone. The constant value $f = 2$ is consistent with experimental data for several types of solid media (Wuerker, 1959; Watstein, 1953).[26, 24]

We have also used the constant value $G_m = 2$ in the crushing zone ($p_c < \sigma < p_2$) when making calculations. As shown in the derivation of Equation 4.30, the relation $G_m = 1 + x_c$ leads to $G_m = 2 - (8/3)(C_2/C_1)^2$ in the crushing zone. It has been found that $G_m = 2$ gives a better fit to the experimental pressure distance points (Figures 4.7 to 4.11). In the derivation of Equation 4.30, it should be noted that the heat loss expression $h = Q/u_s^2 = x_c/6$, is only approximate. It is well known that

the energy, Q, is not the exact heat loss because the Hugoniot expansion curve (Figure 4.6) only approximates the true adiabat curve. Therefore, the better numerical value of 2 for G_m may be interpreted as an empirical factor which adjusts the product hG_m in Equation 4.17 so that it has a more correct average value over the entire range of pressures in the crushing zone.

In the hydrodynamic and plastic zones, we have used the relation $\left(G_m\right)_a = 1 + x_H$ in order to evaluate Equation 4.26. Since the exact value of Q_s/Q in Equation 4.22 is unknown when x is greater than x_H, we have used the equality $Q_s = Q$ only when x is less than x_H.

The parameter x_H is evaluated from the curve of x versus σ (Figures 4.13 to 4.16). It is taken as the point where x on the curved graph is about 30 percent different from the corresponding intercept (σ = constant) on the projected hydrodynamic 45-degree straight line. This point is defined physically in terms of the minimum hydrodynamic pressure, p_H,

$$x_H = (1/2)(\gamma + 1)p_H/(\rho_1 C_1^2) \quad .$$

The medium is said to be plastic at lower pressures where $p_2 < \sigma < p_H$. If an experimental Hugoniot curve is not available, one can determine x_H from the above expression if the minimum hydrodynamic pressure, p_H, can be estimated -- for example, by interpolation from Table 4.3. It is also necessary to have a numerical value for the acoustic dilatational velocity, C_1. It is evident from Table 4.3 that γ is about 3 for porous rock, and about 2 for nonporous rock. The acoustic dilatational velocity, C_1, also determines the "termination-pressure" p_2, defined by the condition $x_2 = 1/2$, so that $p_2 = \rho_1 C_1^2/(\gamma + 1)$.

It must be noted that the dilatational acoustic velocity, C_1, is not generally identical to the measured wave front velocity, U, but is calculated from the equation $C_1 = U(1 + x)^{-1/2}$. The modulus correction, x, is equal to $x_c = 1 - (8/3)(C_2/C_1)^2$ in the crush-crack zones, and $x = \sigma/2p_1$ in the reversible zone. Thus, x is not usually negligible compared to 1, and the wave front velocity, U, corresponds to that of a finite-amplitude disturbance.

Conclusions

The properties of a solid medium which determine the manner of spherical wave propagation from buried explosions have been described by means of a correction factor applied to the known elastic modulus, $\rho_1 C_1^2$, of the medium. Presumably, elastic properties are well known. Also, information is available (Hugoniot data) concerning the hydrodynamic behavior of solid media. However, at the intermediate stress levels where finite amplitude stress waves produce such effects as plastic flow, crushing, and cracking, no experimental information is available for geologic materials. Modulus corrections are

consequently estimated over the range of stress levels where these nonlinear phenomena occur. From these modulus corrections, stress-strain relations are obtained for geologic media over the range of stresses from acoustic to hydrodynamic.

By introducing the concept of wave front shell thickness and by considering the energy associated with an explosive wave disturbance, simple ordinary differential equations are derived whose solutions give analytic expressions for peak stress as a function of distance from explosions. The shell thickness of a spherical wave front represents the distance behind the front which contains essentially all the energy carried along by the wave. Explicit consideration of the time dependence of the wave disturbance is avoided by use of the shell thickness concept, and, because of this, calculations are greatly simplified and result in analytic solutions.

Results of this phenomenological description provide estimates of peak stress at all distances from buried explosions; these estimates, when compared with experimental data, are as accurate as those of the more sophisticated calculations obtained from electronic computers.

The shortcomings of the description are evident and have been emphasized. At the expense of mathematical rigor and detailed description, simplifying assumptions are introduced in order that an analytic solution may be obtained. Nevertheless, despite the approximate nature of the equations, values of stress versus distance may be computed for buried explosions which agree with measurements to better than an order of magnitude over the complete range of stresses from hydrodynamic to acoustic.

LIST OF REFERENCES

1.   Bass, R. C., Hawk, H. L., and Chabai, A. J., Shock Hugoniots of Porous Earth Materials, paper delivered to 32nd International Meeting of The Society of Exploration Geophysicists, Calgary, Alberta, Canada, September 20, 1962.

2.   Bishop, R. H., "Theory of Wave Propagation from Spherical Explosions," Section IV of Close-In Phenomena of Buried Explosions, Sandia Corporation, Albuquerque, N. M., SC-4711(RR), May 1962a; SC-4746(RR), November 1962b.

3.   Chabai, A. J., Synthesis of Shock Hugoniots for Rock Materials, Proceedings of Fifth Symposium on Rock Mechanics, School of Mines and Metallurgy, Institute of Technology, University of Minnesota, Minneapolis, Pergamon Press Ltd. Oxford, England, 1962.

4.   Chabai, A. J., and Bass, R. C., Measurements on a Spherical Shock Wave in a Granite Medium, Sandia Corporation, Albuquerque, New Mexico, SC-4741(RR), 1963.

5.   Cook, M. A., Keyes, R. L., and Ursenbach, W. O., Measurement of Shock and Detonation Pressures, University of Utah, Salt Lake City, Dept. of Metals and Explosives Research, Contract NOw 61-0411-d, ASTIA document AD-258-201, April 1961.

6.   Deal, W. E., Measurement of the Reflected Shock Hugoniot and Isentrope for Explosive Reaction Products, Physics of Fluids, 1, 523-527, 1958.

7.   Duvall, W. L, and Atchison, T. C., Rock Breakage by Explosives, Bureau of Mines Report of Investigations 5356, U. S. Dept. of the Interior, September 1957.

8.   Lamb, G. L., Jr., Some Seismic Effects of Underground Explosions in Cavities, Los Alamos Scientific Laboratory, New Mexico, LA-2405, November 1960.

9.   Lombard, D. B., The Hugoniot Equation of State of Rocks, Lawrence Radiation Laboratory, Livermore, California, UCRL-6311, February 1961.

10.   Lutzky, M., The Spherical Taylor Wave for the Gaseous Products of Solid Explosives, U. S. Naval Ordnance Laboratory, White Oak, Maryland, Navweps Report 6848, May 1960.

11.   Murphey, B. F., Particle Motions Near Explosions in Halite, Sandia Corporation, Albuquerque, New Mexico, SC-4440(RR), June 1960.

12.   Nicholls, H. R., Hooker, V., and Duvall, W. L., Dynamic Rock Mechanics Investigations, Project Cowboy, U. S. Bureau of Mines, College Park, Maryland, Report APRL 38-3.2, September 1960.

13.   Nuckolls, J. H., A Computer Calculation of Rainier, Paper No. C-2 presented at the Second Plowshare Symposium, Lawrence Radiation Laboratory, Livermore, California, UCRL-5675, May 15, 1959.

14.   Perret, W. R., Subsurface Motion From a Confined Underground Detonation, Sandia Corporation, Albuquerque, New Mexico, WT-1529, May 1961.

15.   Perret, W. R., Free Field Ground Motion Studies in Granite, Sandia Corporation, Albuquerque, New Mexico, POR-1803, to be published, 1963a.

16.   Perret, W. R., Mechanisms of Crater Formation (Project Scooter), Sandia Corporation, Albuquerque, New Mexico, SC-4602(RR), to be published, 1963b.

17.   Sachs, D. C., and Swift, L. M., Small Explosion Tests, Stanford Research Institute, Menlo Park, California, Project Mole Final Report, AFSWP-291, December 1955.

18.   Shearer, J. M., Olson, R. G., and Krause, O. H., Close-In Pressure and Shock Arrival Time Measurements, Lawrence Radiation Laboratory, Livermore, California, Final Report, Project Scooter, UCRL-6605, September 1961.

19.   Swift, L. M., Intermediate Range Earth Motion Measurements (Project Gnome), Stanford Research Institute, Menlo Park, California, PNE-111P, February 1962a.

20.   Swift, L. M., Measurement of Close-In Earth Motion, Hardhat Event, Nougat Series, Stanford Research Institute, Menlo Park, California, VUP-2101, March 1962b.

21. Swift, L. M., and Wells, W. M., *Close-In Earth Motions*, Project Hobo, Lawrence Radiation Laboratory, Livermore, California, UCRL-6397, March 1961.

22. Taylor, G. I., *The Formation of a Blast Wave by a Very Intense Explosion*, Proc. Roy. Soc. London A, 201, 159-174, 1950.

23. Warner, S. E., and Violet, C. E., *Properties of the Environment of Underground Nuclear Detonations at the Nevada Test Site*, Contract No. W-7405-eng-48, Lawrence Radiation Laboratory, Livermore, California, UCRL-5542, Rev., April 1959.

24. Watstein, D., *Effect of Straining Rate on the Compressive Strength and Elastic Properties of Concrete*, Proceedings of the American Concrete Institute, 49, 729, 1953.

25. Weart, W. D., *Particle Motion Near a Nuclear Detonation in Halite*, Sandia Corporation, Albuquerque, New Mexico, Project Gnome, PNE-108P, February 1962.

26. Wuerker, R. G. *Influence of Stress Rate and Other Factors on Strength and Elastic Properties of Rocks*, paper delivered at Third Symposium on Rock Mechanics, Colorado School of Mines, April 20-22, 1959.

27. Young, D. D., Jr., *In Situ Measurements of Elastic Properties*, Lawrence Radiation Laboratory, Livermore, California, UCRL-6477, May 1961.

DISTRIBUTION:

Defense Documentation Center (DDC), Cameron Station, Alexandria, Virginia, (20)
Attn: TISIA-21, 22314
Chief of Research and Development, D/A, Washington, D. C. 20310, Attn: Atomic Division (1)
Chief of Engineers, D/A, Washington, D. C. 20310 Attn: ENGCW-NE (1)
ENGTE-E (1)
ENGMC-E (1)
Commanding General, U. S. Army Materiel Command, Washington, D. C. 20310, Attn: AMCRD-DE-N (2)
Commanding General, Aberdeen Proving Ground, Aberdeen, Maryland 21005, Attn: Director BRL (4)
Director, U. S. Army Research and Development Laboratory, Ft. Belvoir, Virginia 22060
    Attn: Chief, Tech. Support Branch (1)
Commanding Officer, Picatinny Arsenal, Dover, New Jersey 07801, Attn: ORDBB-TK (1)
Commanding General, U. S. A. Electronic R&D Lab., Ft. Monmouth, New Jersey 07703,
    Attn: Technical Documents Center, Evans Area (1)
Commanding General, USA Missile Command, Huntsville, Alabama (1)
Commanding General, USA Munitions Command, Dover, New Jersey (1)
Commanding Officer, U. S. Army Corps of Engineers, Beach Erosion Board, Washington, D. C. 20315 (1)
Commanding Officer, U. S. Army Nuclear Defense Laboratory, Edgewood Arsenal,
    Edgewood, Maryland 21040, Attn: Tech. Library (1)
Director, Waterways Experiment Station, U. S. Army Corps of Engineers,
    Vicksburg, Mississippi, Attn: Library (1)
Director, U. S. Army Corps of Engineers, Nuclear Cratering Group, Livermore, California (3)
Chief of Naval Operations, Navy Department, Washington, D. C. 20350, Attn: OP-03EG (1)
Chief, Bureau of Naval Weapons, Navy Department, Washington, D. C. 20360 (2)
Chief, Bureau of Ships, Navy Department, Washington, D. C. 20360, Attn: Code 372 (1)
Code 423 (1)
Chief, Bureau of Yards and Docks, Navy Department, Washington, D. C. 20370, Attn: Code D-400 (1)
Code D-440 (1)
Chief of Naval Research, Navy Department, Washington, D. C. 20390, Attn: Code 811 (1)
Commanding Officer, U. S. Naval Schools Command, U. S. Naval Station,
    Treasure Island, San Francisco, California (1)
Superintendent, U. S. Naval Postgraduate School, Monterey, California (1)
Commander, U. S. Naval Ordnance Laboratory, Silver Spring 19, Maryland, Attn: EA (1)
EU (1)
E (1)

Commanding Officer & Director, U. S. Naval Civil Engineering Laboratory,
    Port Hueneme, California, Attn: Code L31 (1)
Director, U. S. Naval Research Laboratory, Washington, D. C. 20390 (1)
Commanding Officer & Director, Naval Electronics Laboratory, San Diego 52, California (1)
Commanding Officer, U.S. Naval Radiological Defense Laboratory,
    San Francisco, California 94129, Attn: Tech. Info. Division (1)
Commanding Officer & Director, David W. Taylor Model Basin,
    Washington, D. C. 20007, Attn: Library (1)
Underwater Explosions Research Division, DTMB, Norfolk Naval Shipyard, Portsmouth, Virginia (1)
Hq. USAF, Washington, D. C. 20330, Attn: AFRNE (1)
Director of Research and Development, DCS/D, Hq. USAF, Washington, D. C. 20330,
    Attn: Guidance & Weapons Division (1)
ASD, Wright-Patterson AFB, Ohio 45433 (1)
Commander, Air Force Logistics Command, Wright-Patterson AFB, Ohio 45433 (2)
AFSC, Andrews Air Force Base, Washington, D. C. 20331, Attn: RDRWA (1)
AFCRL, L. G. Hanscom Field, Bedford, Massachusetts 01731, Attn: CRQST-2 (1)
AFWL, Kirtland AFB, New Mexico 87117 (4)
Commandant, Institute of Technology, Wright-Patterson AFB, Ohio 45433, Attn: MCLI-ITRIDL (1)
BSD, Norton AFB, California 92409 (1)
Director, USAF Project RAND, Via: U. S. Air Force Liaison Office, The Rand Corporation, (2)
    1700 Main Street, Santa Monica, California, For: Dr. H. L. Brode and Dr. R. Latter
Director of Civil Engineering, Hq, USAF, Washington, D. C. 20330, Attn: AFOCE (1)
Director of Defense Research & Engineering, Washington, D. C. 20330, Attn: Tech. Library (1)
Assistant to the Secretary of Defense (Atomic Energy) Washington, D. C. 20330 (1)
U. S. Documents Officer, Officer of the United States National Military Representative-SHAPE,
    APO-55, New York, New York (1)
Director, Weapons Systems Evaluation Group, OSD, Room 1E880, The Pentagon,
    Washington, D. C. 20301 (1)
Commander, Field Command, DASA, Sandia Base, Albuquerque, New Mexico, 87115 (3)

DISTRIBUTION: (Continued)

Commander, Field Command, DASA, Sandia Base, Albuquerque, New Mexico, 87115, Attn: FCWT   (1)
                                                                                   FCTG   (1)
Chief, Defense Atomic Support Agency, Washington, D. C. 20301, Attn: Major Bruce M. Carswell   (5)
Lawrence Radiation Laboratory, Box 808, Livermore, Calif., Attn: Technical Information Division   (2)
    For: Dr. Lombard and Dr. Holzer
Los Alamos Scientific Laboratory, P. O. Box 1663, Los Alamos, New Mexico,
    Attn: Report Librarian   (2)
Administrator, National Aeronautics & Space Administration, 1512 H Street, N. W.,
    Washington, D. C. 20546   (1)
Langley Research Center, NASA, Langley Field, Hampton, Virginia 23365,
    Attn: Mr. Philip Donely   (1)
Chief, Classified Technical Library, Technical Information Service,
    U. S. Atomic Energy Commission, Washington, D. C. 20545   (1)
Superintendent, Eastern Experiment Station, U. S. Bureau of Mines, College Park, Maryland   (1)
    Attn: Dr. Leonard Obert
Mr. Kenneth Kaplan, United Research Services, 1811 Trousdale, Burlingame, California   (1)
Department of Physics, Stanford Research Institute, Menlo Park, California   (1)
Poulter Laboratory, Stanford Research Institute, Menlo Park, California   (4)
Dr. Neidhardt, General American Transportation Corporation, 7501 N. Natchez Avenue,
    Niles, Illinois   (1)
Dr. T. H. Schiffman, Illinois Institute of Technology Research Institute,
    10 West 35th Street, Chicago 16, Illinois   (1)
Mr. Marc Peter, United Aircraft Corporate Systems Center, Santa Barbara, California   (1)
Roland F. Beers, Inc., 2520 Oakville, Alexandria, Virginia   (5)
Space Technology Laboratories, Inc., One Space Park, Redondo Beach, California   (1)
    Attn: Document Librarian
Dr. Frank Shelton, Kaman Nuclear, Colorado Springs, Colorado   (1)
Paul Weidlinger, Consulting Engineer, 770 Lexington Avenue, New York 21, New York   (1)
    Attn: Dr. M. Baron
Mr. A. Weiderman, Illinois Institute of Technology Research Institute, 10 West 35th Street,
    Chicago 16, Illinois   (1)
Dr. Vincent J. Cushing, Engineering Physics Company, 5515 Randolph Road, Rockville, Maryland   (1)
Forestal Research Center Library, Aeronautical Sciences Bldg., Princeton University
    Princeton, N. J., Attn: Library (For: Dr. Walter Bleakney)   (1)
Department of Interior, U. S. Geological Survey, Denver Federal Center, Denver 25, Colorado   (1)
    Attn: Dr. Carl Roach
Department of the Interior, U. S. Geological Survey, 345 Middlefield Road,
    Menlo Park, California, For: Astrogeology Branch   (1)
Shell Development Company, P. O. Box 481, Houston 1, Texas 77001, Attn: Dr. Sydney Kaufman   (1)
Robert G. Cheshier, Branch Librarian, Boeing Aircraft, P. O. Box 3707, Seattle 24, Washington   (1)
Professor Samuel Katz, Rensselaer Polytechnic Institute, Troy, New York   (1)
Physics International Co., 2229 4th Street, Berkeley 10, Calif., Attn: Dr. W. Birnbaum   (1)
Director, Advanced Research Project Agency (ARPA), Washington 25, D. C.   (6)
VELA Seismic Information Analysis Center, The University of Michigan, P. O. Box 618,
    Ann Arbor, Michigan   (3)
California Institute of Technology, Pasadena, California, Attn: Dr. Press and Dr. Benioff   (2)
VELA UNIFORM, Data Analysis and Technique Development Center, c/o Code TD-1A, AFTAC,
    Headquarters, U. S. Air Force, The Pentagon, Washington 25, D. C.   (2)
Director, Military Application, U. S. Atomic Energy Commission, Washington 25, D. C.   (2)
Continental Oil Company, P. O. Drawer 1267, Ponca City, Oklahoma, Attn: Dr. John Crawford   (1)
Lamont Geophysical Observatory, Palisades, N. Y., Attn: Dr. Jack Oliver   (1)
U. S. Coast and Geodetic Survey, Department of Commerce, Seismology Branch,
    Washington 25, D. C., Attn: Leonard Murphy   (1)
U. S. Coast and Geodetic Survey, Sandia Base, Albuquerque, New Mexico   (1)
National Science Foundation, 1951 Constitution Avenue, N. W., Washington 25, D. C.
    Attn: Earth Sciences Division   (1)
U. S. Geological Survey, Department of the Interior, Washington 25, D. C., Attn: Studies, Crustal   (1)
Crustal Studies Branch, U. S. Geological Survey, 7580 West 16th Avenue, Lakewood 15, Colorado   (1)
United Electro Dynamics Corp., United Earth Sciences Division, Alexandria, Va.   (1)

DISTRIBUTION: (Continued)
Bell Telephone Laboratories, Murray Hill, N. J., Attn: Dr. John Tukey (1)
Atomic Coordinating Office, British Defense Research Staff, British Embassy,
   3100 Massachusetts Avenue, N. W., Washington 8, D. C. (3)
Air Force Office of Scientific Research (SRPG), Tempo Building D, Washington 25, D. C. (1)
Defense Research Board Member Canadian Joint Staff,
   2450 Massachusetts Avenue, N. W., Washington 8, D. C. (1)
U. S. Arms Control and Disarmament Agency, Reference Research Service,
   State Department, Washington 25, D. C. (1)
R. S. Claassen, 5100
F. W. Neilson, 5130
J. W. Easley, 5300
T. B. Cook, 5400
B. F. Murphey, 5410
C. R. Mehl, 5411
R. H. Bishop, 5411 (3)
M. L. Merritt, 5412
A. J. Chabai, 5412 (12)
R. C. Bass, 5412 (10)
J. C. Eckhart, 7250
B. C. Benjamin, 7251
J. W. Wistor, 7251-3 (5)
B. R. Allen, 3421-1
M. G. Randle, 3421-3, Bldg. 880
M. G. Randle, 3421-3, Attn: Mrs. E. Baca, Bldg. 836
W. F. Carstens, 3423
L. D. Patterson, 3423-5 (4)
W. A. Jamieson, 8233
R. C. Smelich, 3427-3 (15)